Spring 1-1-2015

Enhancement of Heat Transfer in Pool and Spray Boiling with Microporous Coatings

Suraj Joottu Thiagarajan
University of Colorado at Boulder, suraj.jt@gmail.com

ENHANCEMENT OF HEAT TRANSFER IN POOL AND SPRAY BOILING WITH MICROPOROUS COATINGS

by

SURAJ JOOTTU THIAGARAJAN

B.E., Anna University, 2005

M.S., The Ohio State University, 2007

A thesis submitted to the

Faculty of the Graduate School of the

University of Colorado in partial fulfillment

of the requirement for the degree of

Doctor of Philosophy

Department of Mechanical Engineering

2015

This thesis entitled:

Enhancement of Heat Transfer in Pool and Spray Boiling with Microporous Coatings
written by Suraj Joottu Thiagarajan
has been approved for the Department of Mechanical Engineering

_____
Prof. Ronggui Yang

_____
Dr. Sreekant Narumanchi

Date _____

The final copy of this thesis has been examined by the signatories, and we find that both the content and the form meet acceptable presentation standards of scholarly work in the above mentioned discipline.

Abstract

Thiagarajan, Suraj Joottu (Ph.D., Mechanical Engineering)

Enhancement of Heat Transfer in Pool and Spray Boiling with Microporous Coatings

Thesis directed by Associate Professor Ronggui Yang and Dr. Sreekant Narumanchi

The relentless increase in the heat flux dissipation levels in electronic devices has necessitated development of new thermal management methods that can handle such heat flux levels, while maintaining a low device temperature. Direct cooling of the electronic components using dielectric liquid coolants, along with phase-change heat transfer, has the potential to achieve this. In this work, the enhancement of boiling heat transfer by the use of a thermally conductive copper microporous coating with a dielectric coolant (3M Novec HFE-7100) under two configurations is studied: passive pool boiling, and spray impingement boiling.

Pool boiling experiments were performed on microporous surfaces and plain surfaces. The microporous surfaces, with coating thicknesses in the range 100 to 700 μm, and porosity of ~57%, showed a significantly lower boiling incipience temperature, enhanced the heat transfer coefficient by 50 – 270%, and enhanced the critical heat fluxes (CHF) by 33 – 60%, when compared to the plain surface. At low heat flux levels, the surface with a thicker microporous coating showed better performance than the thinner one. However, the thinner microporous coating resulted in higher CHF than the thicker surface. High-speed visualization was used to measure the nucleation site density, bubble diameter at departure, and bubble departure frequency. Based on a simple heat flux partition model, neglecting the heat transfer effects due to bubble coalescence, the individual modes of heat transfer (evaporative and single-phase) were computed. Reasonably good agreement between the partition model and the experimental data was obtained. On the plain surfaces, the evaporative and single-phase components were

approximately equal, while on the microporous surfaces, the evaporative component was found to be significantly higher.

We also investigated spray boiling heat transfer performance on the microporous copper surface. Heat transfer data was measured using two full-cone spray nozzles spanning a range of volumetric flow rate from 1.1 cm^3/s to 15.8 cm^3/s, and liquid subcooling levels from 30 °C to 0 °C. The microporous surface showed an enhancement of 300% – 600% in the heat transfer coefficient at a given wall superheat compared the plain surface. The CHF also increased by up to 80%. Counterintuitively, we observed that the liquid spray at near-saturated temperature (0 °C subcooling) had higher heat transfer coefficient and CHF than the subcooled spray, on both surfaces. This likely results from the limited residence time of the liquid droplets in contact with the heater surface and the much higher efficiency of phase change heat transfer. The near-saturated spray undergoes phase change much faster than the subcooled liquid, removing heat more efficiently than the subcooled liquid. New correlations are proposed for predicting the CHF of spray impingement boiling on both plain and enhanced surfaces.

Dedicated to my parents

Acknowledgments

I would like to acknowledge Prof. Ronggui Yang, my Ph. D. advisor, for dedicating his time in guiding me through all the years. I am deeply indebted to Dr. Sreekant Narumanchi at the National Renewable Energy Laboratory (NREL) for his constant guidance and encouragement. I would like to thank Charlie King for helping me with his expert knowledge in instrumentation of the experimental setups, and Dr. Gilbert Moreno for the many discussions that we had regarding the conducting and interpreting of the experiments. I am grateful to our group manager at NREL, Dr. Rob Farrington for this support. I thank my dissertation committee members, Dr. Y.C. Lee, Dr. Julie Steinbrenner and Dr. Kurt Maute, in addition to Dr. Sreekant Narumanchi and Dr. Ronggui Yang, for participating in the review process and helping me explore from multiple perspectives.

I thank my fellow labmates and friends in our group for their encouragement and support: Jen-Hau Cheng, Xiaobo Li, Wei Wang, and Qian Li. I would also like to extend my gratitude to my friends Sanjay Mohanty, Aditya Kausik, Omkar Pradhan, Neeti Wagle, Gopi Krishnan and Shriram Santhanagopalan, who turned the otherwise arduous task of doctoral research into an enjoyable experience.

I would not have been in a position to complete this dissertation without the support of my family. My parents have motivated and encouraged me throughout my life, and I continue to be forever grateful. Special thanks to my wife, Nimisha Morkonda. Her patience, love and support have kept me motivated throughout this process. I appreciate the many sacrifices she has made.

This research was performed under a subcontract from NREL to the University of Colorado Boulder. I would like to acknowledge the financial support of Susan Rogers and Steven Boyd, Technology Development Managers of the Electric Drive Technologies Program in the U.S. Department of Energy Vehicle Technologies Office.

Table of Contents

List of Tables

List of Figures

Chapter I Introduction

I.1 Background and Motivation

Modern technology demands increased power and in an ever decreasing package size. As functions are increased and devices shrink, heat density increases. For example, the high heat fluxes created by high performance electronics offer great challenges to thermal management of devices that employ them. Devices and systems such as computer processors, insulated-gate bipolar transistors (IGBTs), concentrated photovoltaics, solid-state lasers, radar and signal processing systems, require implementation of a thermal management system that is capable of removing high heat fluxes in the range of hundreds of W/cm^2, at relatively low surface temperatures [1]. Two-phase systems utilizing boiling or liquid evaporation have the potential to remove large amounts of heat at low temperature difference. The best cooling performance with liquid cooling can be achieved with the direct cooling of electronics chips as it eliminates the thermal interface layers, and allows for the direct contact of the cooling fluid with the surface of the chip. However this limits the choice of working fluid to dielectric coolants. Due to the inferior thermophysical properties of the dielectric coolants, compared to water, the viability of a direct cooling system is highly dependent on the ability to achieve very large convective heat transfer coefficients [2]. This goal can be realized by adopting a highly effective convective cooling configuration, and also by capitalizing on the benefits of phase change. Forced convective cooling in conjunction with phase change heat transfer is one of the most effective means of high heat flux dissipation. The forced convection aspect can be implemented in several methods including flow boiling, jet impingement and spray cooling. The high heat dissipation potential of these types of cooling schemes is to a large extent a result of the high heat transfer

rates associated with phase change heat transfer, in addition to the enhancement due to the convection. Therefore, any attempt to further increase the already high heat dissipation potential of these cooling schemes should also include enhancing the phase change mechanisms. One of the many methods through which phase-change heat transfer can be enhanced is by surface modification. 3M recently developed a microporous coating for boiling enhancement [3], which has been found to enhance the heat transfer in pool boiling with the dielectric coolant such as FC-72 and HFE-7000 [4]. However, the mechanisms responsible for the enhancement are not clear, and heat transfer enhancement with the use of aggressive convection methods like jet and spray impingement with this coating has not been studied. The goal of this research is to address this lacuna by experimentally studying the boiling heat transfer performance on the microporous surface under quiescent pool boiling and spray impingement. The rest of this chapter provides an overview of the literature on the boiling enhancement with the use of various surface modifications explored in the past, followed by the discussion on the microporous coating that is the focus of this study. The experiments and results are discussed in Chapters II and III for pool boiling and spray impingement cooling, respectively. The outcome of the research would be a contribution to the literature with practical applications for the cooling of high-heat-flux devices.

I.2 Nucleate Boiling Heat Transfer Using Enhanced Surfaces

Two-phase (nucleation and evaporation) enhancement has been the topic of many studies and there are many ways to achieve enhancement. One of the most effective means to augment phase change (boiling) heat transfer is through an increase in the number of active nucleation sites on the heated surface. This can be achieved through either surface roughening and/or the creation of artificial micro cavities on the heated surface [5]. In addition to enhancing nucleate

boiling heat transfer, the capillary wicking of some enhanced surfaces have also been found to enhance evaporation [6,7]. Thus, it seems that enhanced/structured surfaces can increase heat transfer by facilitation phase change in both nucleation and evaporation. The following is a summary of some of the research into surface enhancement techniques applied to pool boiling, followed by a discussion on the literature on spray boiling with enhanced surfaces.

I.2.1 Pool Boiling on Enhanced Surfaces

It has long been understood that pressure, subcooling, heater material and thickness, surface modifications can be used to further raise pool boiling critical heat flux (CHF) limit. Berenson [8] extensively investigated the effect of surface finish on nucleate boiling performance, by studying the characteristics of pool boiling from surfaces with a high density of stable, artificially formed nucleation sites. Later, Costello and Frea [9] studied the surface effects with horizontally-oriented stainless steel semi-cylindrical heaters in water. Coating the heaters with calcium carbonate was found to yield nearly 50% higher CHF values than on smooth heaters. They postulated that the increase in CHF for the treated surfaces was a result of increased wettability. Marto and Lepere [10] investigated the heat transfer enhancement of three commercially available surfaces (Union Carbide High Flux, Hitachi Thermoexcel-E, Wieland GEWA-T) on a cylindrical tube immersed in highly wetting liquids, such as saturated FC-72 and R-113. These surface enhancements are shown in Figure I-1. They observed a 60% decrease in nucleate boiling superheats and a negligible increase in CHF. Of the three surfaces tested, only one was found to enhance CHF (with FC-72) and is due to the relatively larger spacing between pores which reduces coalescence of the vapor columns and thus extend CHF. As early as 1974, a surface enhancement method to upgrade the nucleate boiling performance of silicon chips in dielectric liquids was devised by Oktay and Schmeckenbecher [11]. While it was shown possible

to machine the surface of silicon chips to improve their heat transfer performance, such chip modifications were not usually permissible.

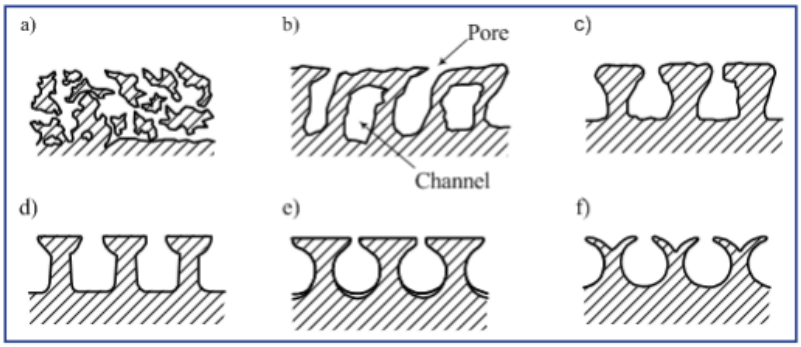

a) Porous layers made of sintered metal particles from 10 to 100 μm in diameter – High Flux (formerly of Union Carbide and now belonging to UOP); **b)** Deformed finned tubes with cut and bent over edges, with pore diameters of approximately 100 μm – Thermoexcel-E (Hitachi); **c)** Knurled and compressed fins – Turbo-B (Wolverine Tube); **d)**, **e)** and **f)** Split and compressed fins: d) Gewa-T; e) Gewa-TX; f) Gewa-TXY (Wieland-Werke)

Figure I-1. Various surface enhancements available in commercial products. Figure from [12].

Mudawar and Anderson [13] found that the surface cavities, approximately 300 μm in diameter, were ineffective in lowering incipience superheats as well as enhancing CHF in FC-72. In a later publication [14], Mudawar presented an extensive summary of his team's studies on the surface enhancement of boiling, including the improvement associated with creating microstructures on the surface with sandpaper, silica blast surface finish, and microfin attachments. All of the surface attachments/treatments yielded some improvements in the FC-72 CHF values.

In recent years great success in pool boiling enhancement has been achieved through the use of thin surface coatings [15]. It is generally believed that such enhancement results from a substantial increase in the nucleation site density and its uniformity across the heated surface. Alternatively, porous and microporous coatings can facilitate two-phase flow and boiling within the surface layer and produce substantial CHF augmentation. Webb [16,17] found that the

primary variables in microporous surface enhancement of pool boiling CHF were particle shape, coating thickness, and porosity and that particle size played a secondary role. Bergles and Chyu [18] observed an improvement in the boiling heat transfer with the use of commercial porous surfaces. Afgan et al. [19] studied the boiling characteristics from 30–75% porosity layers of sintered metal particles, using water, ethanol and R-113. They observed a qualitative change in the boiling mechanism at high heat fluxes and ascribed it to the presence of the sintered spherical particles. From these and related studies, it may be argued that much of this enhancement in CHF can be explained by the ability of the porous coating to smooth the transition from pool boiling to film boiling, facilitating the continuation of pool boiling on the outer surfaces of the porous layers, while vapor slugs – which may partially blanket the heated surface – form inside the coating.

Thome [20] reviewed a large number of data sets for pool boiling on porous coatings and found that, while these surfaces performed better than plain surfaces, there was little correlations between the optimum coating geometries in one study to those found in others. The performance benefit of the coatings is thought to be due to the increase in the effective boiling surface area, i.e., the vapor–liquid contact area, within the thick porous layer. Thome [20] also observed that three distinct evaporation mechanisms were present in porous coatings: thin film, capillary, and external evaporation, and that convective heat transfer could also be expected to prevail on the exterior surfaces, due to bubble agitation and vapor/liquid exchange, and inside the structure due to laminar flow through the pores, possibly with strong entrance effects. In a later study, Chang and You [21] suggested that a lower porosity might lead to lower internal vaporization rates (thin film and capillary vaporization) due to reduced flow within the structure. While many of the enhanced surfaces tested have demonstrated the ability to reduce wall superheat and increase

CHF, their feature sizes are apparently too large to effectively trap a large number of embryonic bubbles when immersed in dielectric liquids.

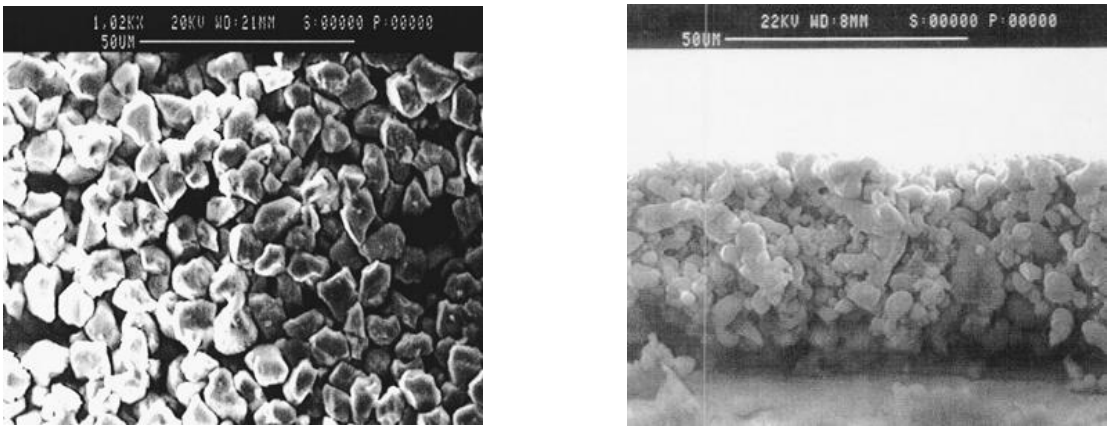

(a) (b)

Figure I-2. (a) DOM microporous coating (Kim et al. [22]); (b) ABM microporous coating (Rainey et al. [23])

You et al. [24] studied the enhancement potential of "particle layering," achieved by spraying particles on a flat surface and showed that a treated surface, immersed in saturated FC-72, could provide a 109% increase in CHF over the plain surface. O'Connor and You [25] reported a 224% larger CHF value when boiling with 45 °C subcooling relative to the un-treated surface at saturated conditions in FC-72. The effect of low thermal conductivity microporous surfaces (Figure I-2(a)) on nucleate boiling heat transfer in saturated FC-72 was studied by Kim et al. [22], using high-speed photography to study bubble size, bubble frequency, and vapor film characteristics on plain and coated thin wire heaters. Their tests revealed enhancement in both the heat transfer coefficients and CHF. The increase in heat transfer coefficient was attributed to the higher number of active nucleation sites of the coating. Additionally, measurements of the bubble departure diameters and frequencies of both coated and non-coated surfaces revealed that the porous coated surfaces produce smaller bubble departure diameters and higher bubble departure frequencies as compared to the non-coated heaters. Therefore, concluding that at

higher heat fluxes, the porous coated surfaces enhance micro-convection and reduce vapor generation which results in higher CHF. Rainey et al. [23,26] studied CHF enhancement on flat copper heaters coated with microporous structures and immersed in FC-72, achieving a maximum CHF value of nearly 80 W/cm^2 and offering an empirical correlation based on their results and others from the literature (Figure I-2(b)). When tested in pool boiling, these microporous coatings have demonstrated significant enhancement to the heat transfer coefficients, critical heat flux (CHF) and boiling incipience. When applied to flow boiling, the low thermal conductivity of the microporous layer, led to degraded heat transfer performance at higher velocities [27]. The heat transfer degradation observed is due to the low-thermally conductive nature of bonding epoxies used in these microporous coatings. Later, combined results for enhanced microporous and pin finned structures on the heaters subjected to a range of pressures (between 30 and 150 kPa), subcoolings (as high as 50 °C), and dissolved gas concentrations in FC-72 were presented [23], resulting in a maximum CHF value of 61.4 W/cm^2. The relative enhancement of CHF on finned surfaces, from increased subcooling, was greater for microporous surfaces than for the plain finned surface, but it was found to fall below the values achieved with microporous coated heaters. In an extended review of microporous surface coating enhancement of pool and flow boiling [28], You et al. reported a decrease in the boiling incipience superheat along with an increase in CHF, and revealed that applied microporous coatings have been proven to survive up to 10 years of continuous service. They ascribed the CHF increase to higher bubble departure frequencies along with smaller bubble departure diameters, leading to a larger microconvection contribution and higher heat fluxes at a given wall superheat.

El-Genk and Parker [29] investigated the effects of subcooling on pool boiling of HFE-7100 from 3 mm thick porous graphite surfaces. Along with nucleate boiling heat fluxes more than five times higher and surface superheats significantly lower than those for a bare copper surface in the same experimental apparatus, CHF of the porous graphite surface was found to equal 31.8 W/cm^2 and 66.4 W/cm^2 for 0 and 30 °C subcooled boiling, as opposed to CHF values for the smooth copper of 21.5 W/cm^2 and 37.3 W/cm^2, respectively, reflecting a greater enhancement for subcooled pool boiling than under saturated conditions.

Pool boiling on thin and uniform porous coatings was also examined experimentally by Hwang and Kaviany [30] for various copper particle diameters (40-200μm) and fabrications with n-pentane. The coating thicknesses were 3-5 times the mean particle diameter with a constant porosity of 0.4. The results show that the CHF is about 1.8 times higher for all the coatings, with the largest enhancement obtained with the 200 μm particles. It was suggested that the presence of the thin, uniform porous coating influences the hydrodynamic instabilities responsible for CHF by statistically reducing the critical Rayleigh–Taylor wavelength and/or increasing the vapor area fraction. It was postulated that for a 2-fold increase in CHF, the unstable wavelength in the classical Kutateladze–Zuber CHF model would need to fall to nearly one-quarter of that for a plain surface.

Li and Peterson [31,32] conducted a parametric study with thermally conductive coatings created by sintering layers of copper wire screens to produce porous coatings with various thicknesses, porosities and pore sizes. They report that there is a distinct difference in performance between thin and thick coatings with thin coatings resulting in higher heat transfer coefficients while thick coatings produce higher CHF.

I.2.2 Spray Boiling on Enhanced Surfaces

The use of enhanced surfaces on spray cooling has received much less attention as compared to their application to pool boiling. Pais et al. [33] studied the effect of surface roughness on spray cooling. They reported heat flux as high as 1200 W/cm^2 at low wall superheats using water on roughened surfaces. The proposed that surfaces with higher roughness create larger liquid films whereas surfaces with lower roughness would result in thinner liquid films. This in turn results in evaporation being the dominant heat transfer mode for the lesser roughened surfaces and it is these surfaces which outperform the more roughened surfaces. Kim et al. [6] investigated spray cooling on porous coatings. Experiments were conducted using air atomized water sprays at relatively low flow rates (less than 3 ml/min) and low-thermally conductive microporous coatings. Their results show enhancement to both heat transfer rates (at higher heat fluxes) and CHF for the coated surface as compared to the uncoated one. They associate this enhancement to the liquid wicking effect of the coating. Other investigators have used more highly-structured surfaces, as compared to [6,33] to enhance spray cooling. Silk [34] used various embedded (dimples & porous tunnels) and extended surface (straight, cubic and radial fins) structures with spray cooling using PF-5060. It is reported that of all tested surfaces, the straight fins and porous tunnels provided the highest CHF. Inspired by these results, Silk [35] investigated the effect of the pore size (0.25, 0.5 & 1 mm) on porous tunnel spray cooling performance. Results showed that the largest pore size produced the highest CHF while the smallest pore produced the lowest. The size of the structures tested in both [29, 30] were on the order of a millimeter and therefore most of enhancement from these surfaces is likely due to the fin effect and the areal enhancement. Coursey et al. [36] studied spray cooling on high aspect ratio open microchannels with heights between 0.25 and 5 mm. They observed a 200% enhancement in the heat transfer at

the low temperature single-phase regime, and enhancement up to 180% in the boiling regime. High spray efficiency approaching 100% was observed in the microchannel boiling with the flow rate of the order of 1 $cm^3/cm^2/s$. Recently, Bostanci et al. [37,38] experimented using surfaces with micro-scale indentations and protrusions, macro (mm) scale pyramidal pin fins, and multi-scale structured surfaces, combining macro and micro-scale structures. Spray cooling tests using ammonia as the working fluid, revealed enhancement with these structured surfaces and heat transfer coefficients as high as 47 $W/cm^2/K$. CHF values over 950 W/cm^2 were measured, and it was surmised that the enhancement was due to the better liquid retention and spreading capability of the enhanced surfaces.

I.3 Objectives

Despite much work done in the field of boiling, our understanding of the processes responsible for the enhancement of heat transfer remains incomplete. Moreover, very little work exists in the literature on the mechanisms of boiling heat transfer processes on enhanced surfaces, with the application of spray impingement. The overall objective of this study is to experimentally investigate the fundamental mechanisms of enhancement in boiling heat transfer performance that could be obtained by the use of a thermally conductive microporous copper coating, and the influence of the various parameters on the spray heat transfer process, in view of potential application to cooling of power electronics.

- Investigate pool and spray impingement boiling enhancement using the thermally conductive microporous coating.

- Through the use of high-speed visualization of the boiling process in pool configuration, measure the bubble site density, diameter and frequency of bubble departure on plain and microporous surfaces, and correlate these parameters of bubble dynamics to the total heat transfer. Identify the factors responsible for the enhancement of heat transfer with the microporous surface.
- With spray cooling, determine the effect of nozzle type, flow rate/velocity and subcooling on heat transfer performance (plain and microporous). Quantify enhancement to the heat transfer coefficients and critical heat flux (CHF).

I.4 Thermally Conductive Microporous Copper Coating

The microporous coating that is studied in this work was developed by 3M Company [4]. The procedure for producing the microporous surface is proprietary, and involves use of 5-20 μm copper particles coated with a ~20-nm-thick layer of silver. The 3M product code for the powder is L-20227 [3]. The powder is mixed with Dow Corning 704 Diffusion Pump Fluid to create a screen-printable mixture that is applied to the flat copper substrate. Coated parts are fired in a 0.01-milliTorr vacuum furnace at a maximum temperature of 850 °C for up to 120 minutes to achieve the coating [4]. The coating can be made to any required thickness, and has a porosity of about 57%. As shown in the SEM image of the microporous coating in Figure I-3, the microporous copper layer includes cavities of a variety of sizes, which result in a high nucleation site density. In addition, the layer includes a network of interconnected channels that facilitate liquid replenishment that could potentially delay dry-out on the surface to higher heat flux values as compared to the plain surface.

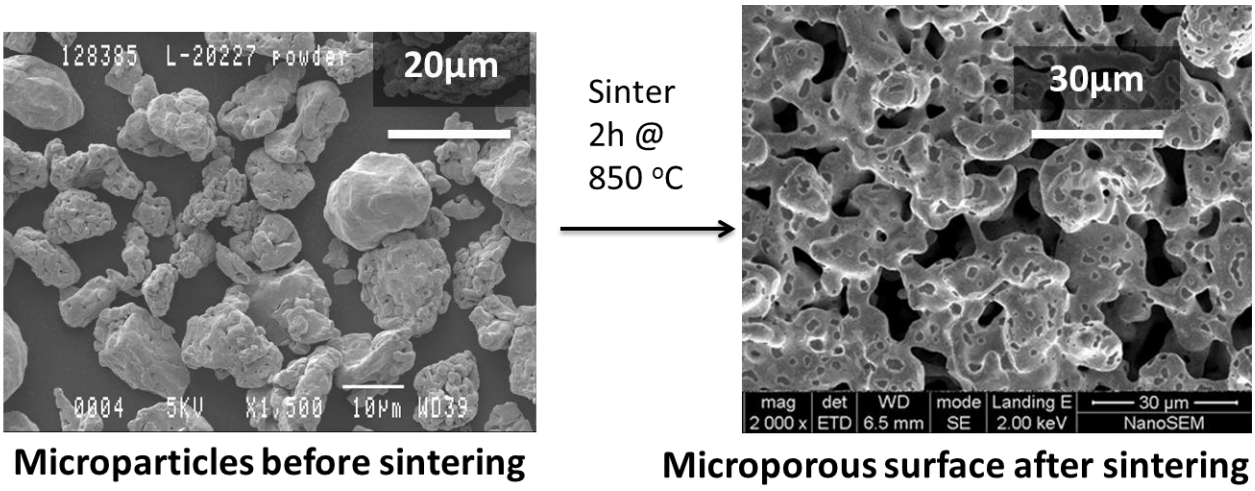

Figure I-3. Silver-coated copper microparticles are sintered together in vacuum to obtain the microporous copper coating that is the focus of this study.

I.5 Heat Transfer Fluid: HFE-7100

3M Novec® HFE-7100 was the working fluid used in this study. The dielectric fluid HFE-7100 has been identified as a potential coolant for cooling power electronics in electric-drive vehicles because of the desirable properties (very low global warming potential, zero ozone depletion potential, nonflammable, and high dielectric strength, in addition to good thermophysical properties) [2], in addition to low saturation temperature, low freezing temperature, and good chemical compatibility with many materials. The relevant thermophysical properties of the fluid at various temperatures of interest in this study are show in Table I-1 [39].

Table I-1. Thermophysical properties of saturated HFE-7100 at various temperatures.

$T_{liq,}$ C	30°	45°	60.4°
Liquid density ρ_l, kg/m^3	1502	1462	1418
Vapor density ρ_v, kg/m^3	3.3	5.43	12.54
Liquid viscosity μ_l, Pa-s	5.3×10^{-4}	4.5×10^{-4}	3.8×10^{-4}
Surface tension σ, N/m	12.8×10^{-3}	11.2×10^{-3}	9.3×10^{-3}
Liquid thermal conductivity k, W/m/K	0.068	0.065	0.062
Liquid specific heat C_P, J/kg/K	1193	1223	1254
Latent heat of vaporization h_{lv}, kJ/kg	122	117.3	112

Chapter II Pool Boiling on Microporous Surfaces

II.1 Introduction

Boiling heat transfer on a surface involves heterogeneous nucleation, growth of vapor bubbles, and the subsequent departure of these bubbles from the heated surface. The large latent heat of vaporization, compared to the specific heat of a liquid, makes boiling a very efficient mode of heat transfer. Pool boiling is the boiling phenomenon that takes place in a quiescent pool of the liquid where the heated target surface is submerged, and the relative motion of the vapor bubble and its surrounding liquid is primarily due to buoyancy. The mechanisms of heat transfer in nucleate boiling has been debated for over half a century due to the complexity of the process and difficulty/impossibility of directly observing the process. The proposed models concerning the role of bubbles in boiling heat transfer process can be broadly classified into two categories [40]:

1. Single phase convection models
2. Combined single phase convection and latent heat transfer models.

The first category of models have attempted to simplify the essence of the boiling heat transfer process to mechanisms normally attributed to steady single phase heat transfer. In these models, the role of phase-change processes is relegated to the role of secondary parameters, which indirectly influence the resulting heat transfer. Models proposed by Jakob and Linke [41], Rohsenow [42], Tien [43], and Zuber [44] are based on the analogy of single phase heat transfer to boiling. In later models, researchers tried to provide a more explicit connection between the transient bubble dynamics and the resulting heat transfer. Along these lines, Forster and Greif [45] postulated that bubbles act as micropumps that transport superheated liquid into the bulk as

they grow and depart from the surface. The total heat transferred through subsequent pumping action was calculated using the volume of the bubble and its frequency. They used the difference between the wall and bulk liquid temperatures to define the energy transported in the pumping action. Mikic and Rohsenow [46] postulated that heat transfer during boiling mainly occurs in a transient conduction heat transfer process. They assumed that a departing bubble pumps away the hot liquid adjacent to the surface from an area twice the bubble diameter. They approximated the transient heat transfer into the near-wall entrained liquid using the transient conduction solution through a semi-infinite body (the liquid), while simultaneously excluding heat transfer from areas outside the bubble influence region. Haider and Webb [47] extended the Mikic and Rohsenow model by including the effect of another mechanism of heat transfer that they called transient convection. This mechanism of heat transfer was suggested to arise as a result of convection in the wake of the departing bubbles. In order to evaluate their model using the existing data on large surfaces, Haider and Webb used an existing model for nucleation site density. Then, they tried to fit their model to experimental data by changing the weight factors considered for each mechanism of heat transfer. Their analysis suggested that transient convection is the dominant heat transfer mode.

The second group of models account for latent heat transfer from the surface along with the single-phase convection. For example, Judd and Hwang [48] and more recently Dhir [49] proposed that by combining the contributions of microlayer evaporation, transient conduction, and natural convection one can determine a more comprehensive boiling heat transfer correlation. Dhir [49] further elaborated that for this correlation to be verified as a predictive tool, one needs to have closure models for several parameters: bubble diameter, bubble departure frequency, diameter of the area influenced by the bubble, the average heat transfer coefficients

for natural convection and microlayer evaporation. Although models exist in the literature for some of these parameters, there is no consensus on how well they function, or even over what general region of parametric space they should be used. Similar to the Judd and Hwang analogy, Benjamin and Balakrishnan [50] assumed that microlayer evaporation, transient conduction, and natural convection heat transfer modes constitute the total surface heat flux. However, they made different assumptions concerning the activation time period and magnitude of these mechanisms.

Moghaddam and Kiger [40,51] studied a single bubble growth and departure from an artificial nucleation cavity with FC-72, and the temporally- and spatially-resolved temperature distribution under the bubble during the entire process. They have considered more than one of the mechanisms discussed above and obtained a good match with particular sets of data included in the validation. As the bubble grew from the cavity, analysis of the temperature histories as measured by each sensor suggested the presence of micro-layer evaporation in correspondence of the triple contact line, moving outward as the contact area expanded. The contact area expansion phase was identified as "micro-layer evaporation region": temporal drops (~ 1 ms) of the temperature for the sensor crossed by the contact line were observed. Successively, as the contact area shrank, similar drops were also noticeable because of the rewetting of the surface: this phase was identified as "transient conduction phase". However, the temperature variations seemed to be limited to a narrow area very similar to the triple contact line area. The heat flux was numerically derived from the temperature variations. Micro-layer evaporation was calculated to contribute only ~22% to the total bubble growth in the considered case. The total heat flux generated in the projected bubble area (i.e. the surface area corresponding to the maximum bubble radius) had a much smaller contribution than the total heat necessary for the bubble growth, showing that the heat contribution from the liquid outside the projected area could be

very significant. Contributions of micro-layer, transient conduction and micro-convection were investigated at different wall temperatures (significantly higher than the saturation temperature of the fluid). Micro-convection, defined as natural convection enhanced by the effect of the bubble growth around the bubble itself, was found to contribute approximately 2.3 times greater than pure natural convection. While microlayer evaporation and transient conduction were not strongly affected by temperature variations, the microconvection contribution significantly increased with increasing temperature.

In summary, it is found that heat transfer occurs through the following modes during saturated nucleate boiling on a plain surface, as illustrated in Figure II-1 (a): evaporation, where vapor is formed by the evaporation of the thin microlayer of liquid under a growing bubble and/or of the superheated liquid on the bubble wall [52,53]; quenching [14, 15], where, after the departure of a bubble, heat transfer to the cooler liquid that rushes in to fill the void occurs by transient conduction; microconvection [42,43,54] where the agitation of the liquid by the bubble motion results in increased heat convection near locations of bubble activity; and natural convection at locations on the target surface far away from the bubble activity. In a relatively simple model, the following bubble nucleation quantities are usually considered in developing theoretical models to analyze heat transfer characteristics: average bubble departure diameter (*D*), average bubble departure frequency (*f*), and average active nucleation site density (*N*). Other researchers have utilized high-speed visualization in order to characterize bubble dynamics on plain surfaces, and determine the contributions of the phase-change and single-phase convective heat ([55–57], for example).

(a)

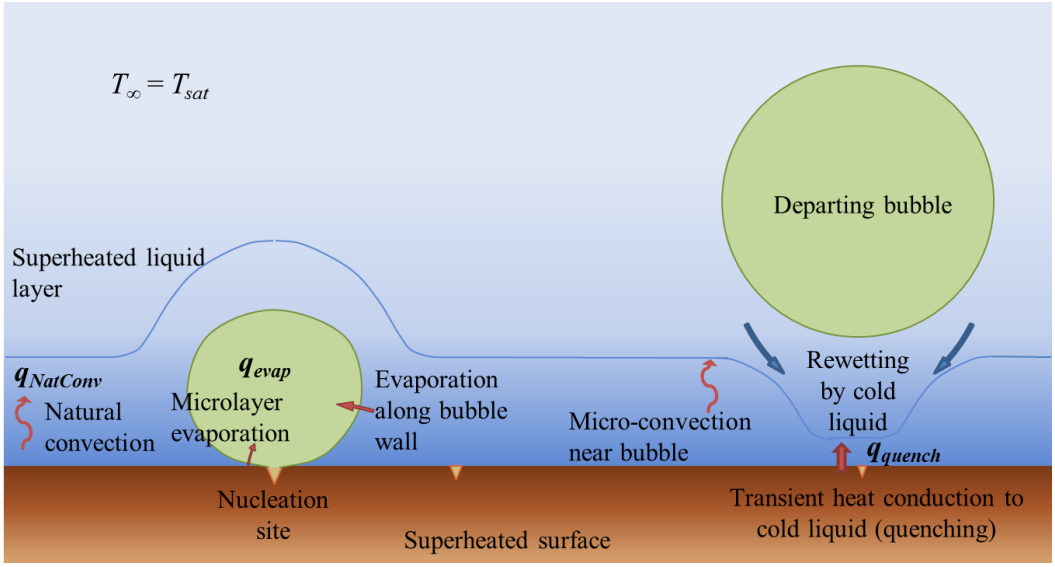

(b)

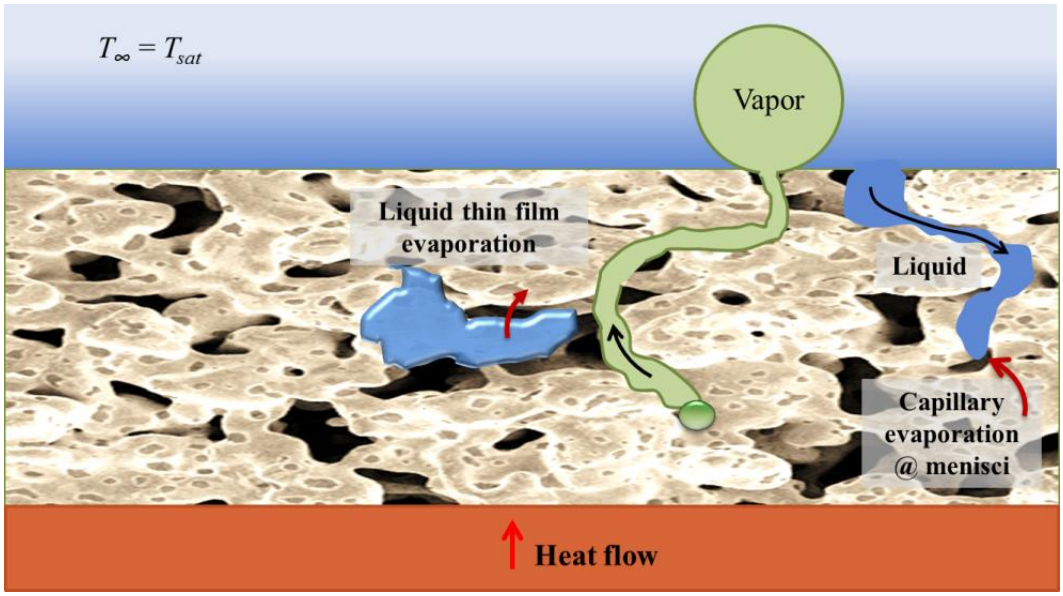

Figure II-1. (a) Schematic diagram showing the different modes of heat and mass transfer on (a) plain surface and (b) inside and outside the microporous surface. In addition to the modes of heat transfer shown in the figure, bubble pumping action results in convective heat transfer inside the microporous layer.

On a surface with a porous coating, heat transfer can be enhanced due to the presence of a few additional modes within the passageways [20], as illustrated in Figure II-1 (b).Vapor is generated by nucleation and bubble growth within the porous layer, evaporation of liquid thin-film on the internal surfaces, and capillary evaporation at the menisci. Single-phase convective heat transfer takes place from the particles to the liquid due to bubble pumping and vapor

motion. Little data exists in the literature that detail the characteristics of bubble dynamics on microporous surfaces, and there appears to be none that relates the bubble characteristics to the heat transfer on a microporous surface except [22].

Assuming condensation of vapor does not occur anywhere from the point of generation of the vapor bubble until its departure from the exterior of the microporous layer, the total heat transfer from the target surface to the fluid by phase-change may be estimated using the rate of vapor departure from the surface. However, the single-phase heat transfer modes within the layer cannot be captured in a visualization study. The objectives of this study are therefore to investigate the saturated pool boiling heat transfer performance and bubble dynamics on the thermally conductive microporous copper coated surface with HFE-7100 and to quantify the contributions to heat transfer through different modes using high-speed visualized bubble dynamics information. In the present study, the average bubble departure diameter (D), the average bubble departure frequency (f), and the average active nucleation site density (N), are calculated from high-speed movies of saturated pool boiling on plain copper surfaces of two different roughness levels and on three microporous copper surfaces at different heat fluxes (in the isolated bubble regime). These parameters are then used to obtain a quantitative measure of the contributions due to various modes of heat transfer on the surfaces using the partition model.

II.2 Experimental Apparatus and Procedure

II.2.1 Pool Boiling Setup

The experimental setup was designed to study pool boiling heat transfer in a horizontal configuration with plain or microporous copper surfaces. Because of the desirable properties of the fluid HFE-7100 (very low global warming potential, zero ozone depletion potential,

nonflammable, and high dielectric strength, in addition to good thermophysical properties), it has been identified as a potential coolant for cooling power electronics in electric-drive vehicles [2].

Figure II-2 shows the schematic diagram and photograph of the setup. The setup primarily consisted of an aluminum chamber to hold the test fluid (liquid-vapor) at saturation conditions, and the heater and temperature sensor assembly which contained the target surface (plain or with microporous coating) to be tested. The aluminum boiling chamber of diameter 12 cm and width of 5 cm had glass windows in the front and the back to allow for the observation of boiling phenomena on the target surface. The chamber was filled with HFE-7100 liquid up to a height of about 6 cm above the target surface. Flexible silicone heaters were attached to the aluminum walls of the chamber to heat the liquid/vapor to maintain the liquid at the saturation temperature. The vapor would rise to the top region of the chamber by buoyancy, go through the reflux condenser located at the top of the chamber, and condense back to liquid pool. The pure liquid-vapor mixture in the chamber was maintained at 54±0.2 °C, which is the saturation temperature corresponding to the atmospheric pressure of HFE-7100 in Golden, Colorado (82 kPa at elevation of 1730 m). Table I-1 gives the thermophysical properties of HFE-7100 at various temperatures [39].

(a)

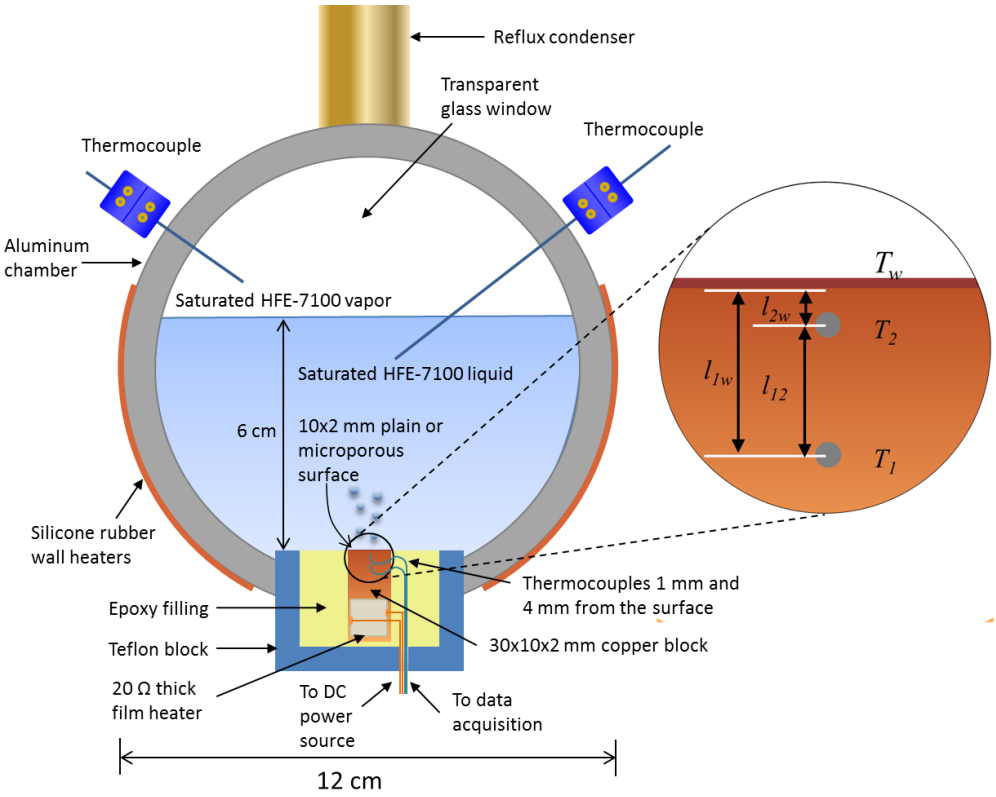

(b)

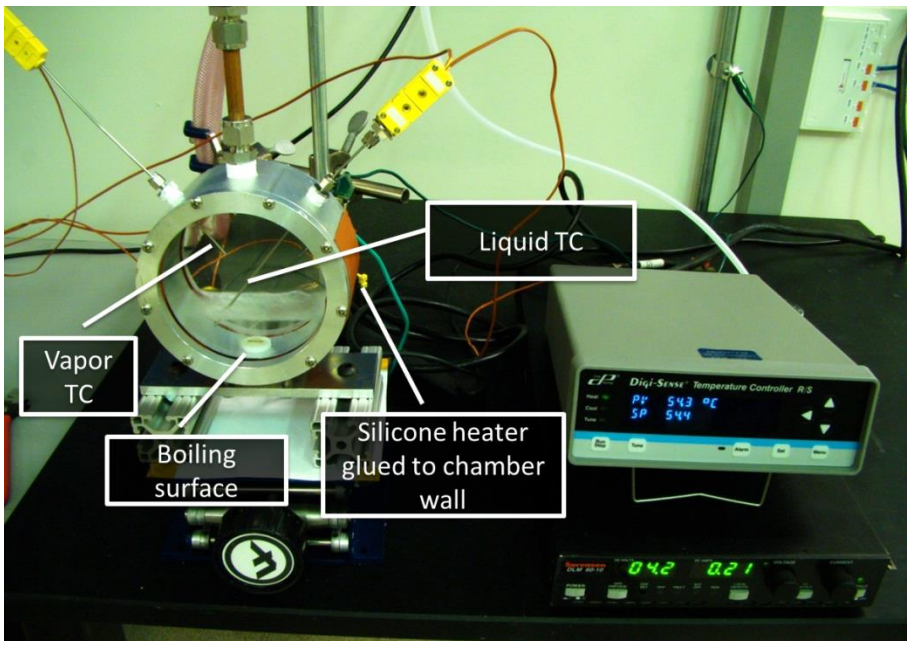

Figure II-2. (a) Schematic diagram and (b) photograph of the pool boiling facility

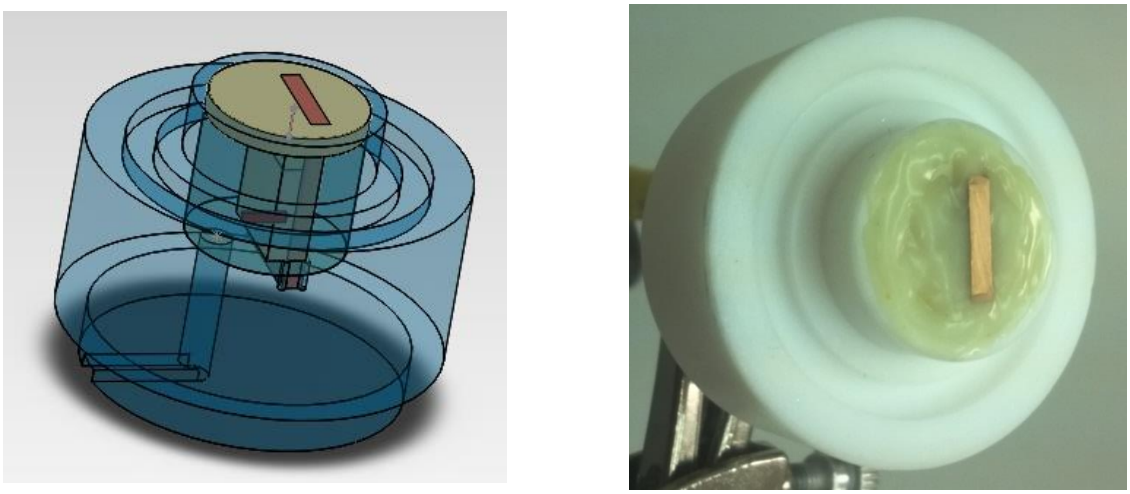

(a) (b)

Figure II-3. (a) Schematic and (b) photograph of the test heater assembly showing the 2 mm x 10 mm copper surface exposed on top.

Figure II-3 shows the schematic diagram and photograph of the heater and temperature sensor assembly. The assembly consisted of a cuboidal oxygen-free copper block (dimensions 2 mm x 10 mm x 30 mm, thermal conductivity k = 393 W/m-K [58]) with a Beryllium oxide ceramic thick film heater of resistance 20 Ω (Components General CCT-375) epoxied to it using a thin layer of a relatively high thermal conductivity (k = 1.6 W/m-K) Epotek®-EE129-4 compound (Epoxy Technology). Two K-type thermocouples with junction diameter 0.25 mm were epoxied to 0.3 mm diameter holes in the copper block, at distance of 1 mm and 4 mm from the target surface using Arctic Silver™ thermal adhesive, such that the thermocouple junctions were located at the center of the copper block at a position 1 mm from the vertical surface. This copper-heater-thermocouple assembly was then placed in the cavity of a custom-fabricated Teflon block (k = 0.2 W/m-K), with 3M Scotch-Weld™ DP-420 epoxy (k = 0.18 W/m-K) filling up the empty volume, so that only the 2 mm x 10 mm target surface of the copper block (along with the surrounding epoxy) was exposed to the boiling chamber when assembled. The perimeter

of the copper surface was covered by the epoxy to prevent boiling at the edges. The heater and temperature sensor assembly was placed under a circular slot in the aluminum chamber, and fastened tightly to the chamber to prevent any liquid leakage.

High speed videos of the boiling dynamics, that is, bubble formation and departure from the target surfaces were obtained using a visualization setup that consisted of a high-speed camera (Photron™ Fastcam SA3 with frame rates of 1500 – 3800 fps) fitted with a long distance microscopic lens (Infinity™ K2/SC with CF-2 objective lens) and a cold (LED) light source (SugarCube™ quad LED). Figure II-4 shows the photograph of the setup during measurement along with the high speed camera. The target copper surface that was exposed to the liquid in the chamber was rectangular with a width of 2 mm and length of 10 mm. The width of the surface was kept small so that the nucleation sites on the entire surface were visible during boiling in order to accurately determine the bubble site density. The inputs from the thermocouples were fed into a data acquisition system and read using LabVIEW, while all the controls were manually operated. To verify that the pool boiling setup we built with high speed visualization on the 2 mm x 10 mm target surfaces could be used to obtain reliable data, a few tests were also conducted using a 10 mm (width) x 10 mm (length) x 2 mm (depth) copper block in a setup similar to that used by El-Genk and Bostanci [59]. As discussed in Section 3.1.1, the pool boiling curves in this study were found to agree well with the results in [59] for the plain surface, thus validating the current setup.

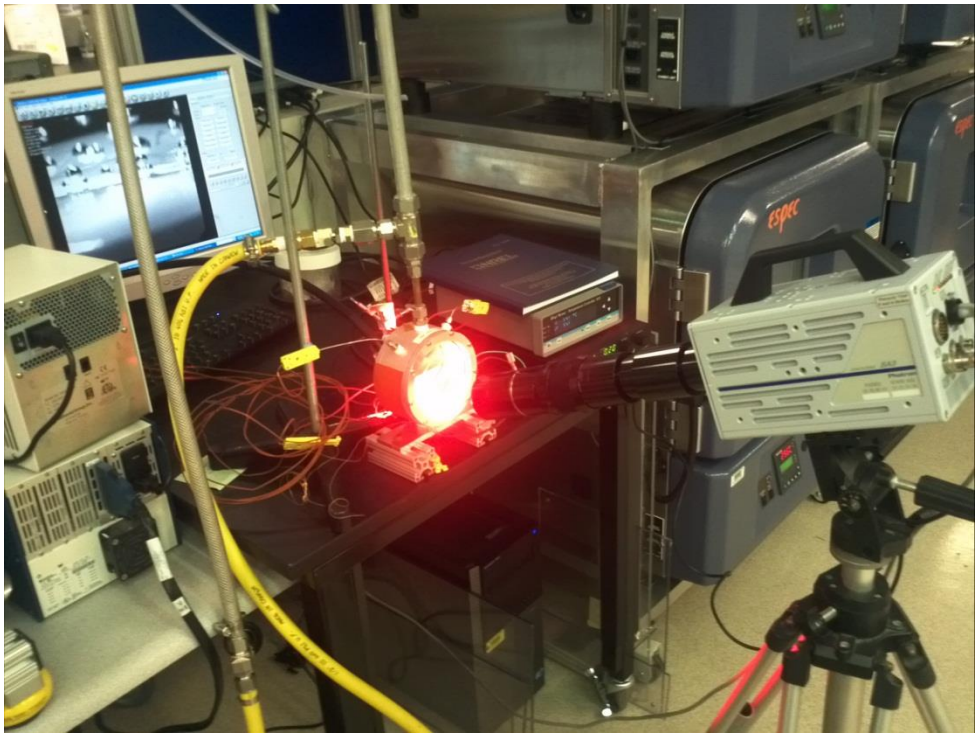

Figure II-4. Photograph of the pool boiling visualization setup during measurement.

II.2.2 Sample Surfaces

Two types of surfaces were studied: the baseline case of plain copper surfaces with no coating, and surfaces with microporous copper coatings. The plain surfaces were prepared by polishing the surfaces with #600 grit paper and then with #2000 or #1500 grit paper, resulting in mean surface roughness, R_a, of 0.33 μm and 0.78 μm, respectively, measured with a Fowler PocketSurf™ roughness profilometer. The surface was deoxidized before testing by wiping with cotton swabs dipped in hydrochloric acid and cleaning with isopropanol. The scanning electron microscope (SEM) images of the plain surfaces are shown in Figure II-5 (a) and (b). The SEM images show that the cavities in the plain surfaces are of dimensions less than 1 μm in diameter, and the surface with R_a = 0.33 μm is much smoother than the one with R_a = 0.78 μm. The surfaces with the microporous copper coating were obtained from 3M Company. The procedure

for fabricating the microporous copper layer on the plain copper surface involved fusing of copper-rich microparticles of diameters between 5 and 20 μm on the copper surface at a temperature of ~850°C [3,4]. Three samples with coating thicknesses of 100 (± 8) μm, 360 (± 30) μm and 700 (± 30) μm were prepared. The porosity of the microporous coating, calculated using weight and volume measurements, is found to be 55% – 60%. SEM images of the microporous coating (Figure II-5 (c) and (d)) show a microstructure with irregular, elongated pore structures, with cavity sizes in the range of 0.5 μm to 5 μm, that could potentially serve as nucleation sites. The presence of the microscale channels also results in a much larger surface area (compared to the nominal external surface area) that is available for thin film evaporation of the liquid, which could potentially augment the heat transfer. Furthermore, the network of interconnected channels that facilitate liquid replenishment could potentially delay dry-out on the surface to higher heat flux values as compared to the plain surface.

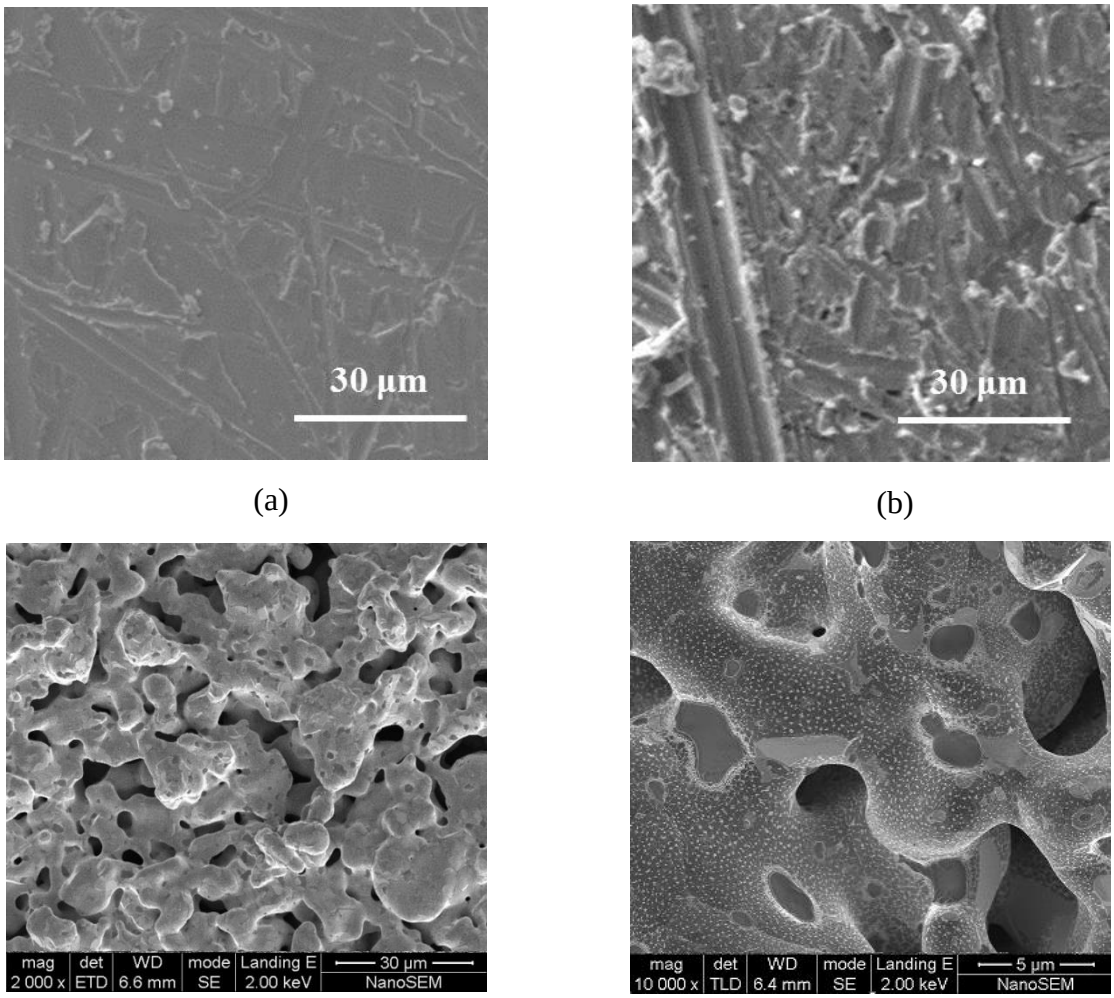

Figure II-5. Scanning electron microscope images of (a) plain surface of R_a = 0.33 µm, (b) plain surface of R_a = 0.78 µm, (c) and (d) microporous surface at two different magnification levels.

II.2.3 Experimental Procedure and Data Reduction

Before each experiment, the HFE-7100 liquid in the pool boiling chamber was degassed for 60 to 80 minutes to expel any dissolved non-condensable gases. This was accomplished by boiling the liquid vigorously at 54 °C using the guarded silicone heaters around the chamber, and allowing the vapor mixed with the non-condensable gases to flow through a condenser located

above the chamber. The portion of the condensed vapor dripped back into the chamber, while the non-condensable gases escaped. After this procedure, the system was allowed to reach a steady state, with no power input to the target copper surface, so that saturation conditions existed within the chamber. Then the power to the target surface was incrementally increased, and measurements were taken after the temperatures reached a steady state (that is, when the temperature variation was < 0.05 °C over a period of 120 seconds). The thermocouple readings were averaged over a period of 30 seconds. Assuming one-dimensional heat conduction in the copper block, the heat flux through the surface (q") was determined by the temperature difference across these two thermocouples using equation (II-1),

$$q" = k\frac{(T_1 - T_2)}{l_{12}}, \qquad \text{(II-1)}$$

where k is the thermal conductivity of oxygen-free copper (k =393 W/m-K [58]), T_1 and T_2 are the temperatures farther away and closer to the target surface respectively, and l_{12} is the distance between the thermocouple locations. The calculated heat flux was then used to determine the wall temperature of the target surface T_w by assuming one-dimensional heat flow using equation (II-2),

$$T_w = T_1 - \frac{l_{1w}q"}{k}, \qquad \text{(II-2)}$$

where l_{1w} is the distance between the thermocouple location and the surface. The heat transfer coefficient, h, was calculated using

$$h = \frac{q"}{(T_w - T_{sat})}. \qquad \text{(II-3)}$$

CHF was defined as the highest heat flux at which stable target surface temperature was maintained, before a sharp increase in temperature occurred (> 10 °C per second) with a slight increase in the power input.

II.2.4 Experimental Uncertainty

The uncertainty of the measured heat flux was mainly from the accuracy of the position and calibration of the thermocouples. A National Institute of Standards and Technology (NIST)-traceable Resistance Temperature Detector (RTD) was used along with a Hart Scientific micro calibration thermal bath Model 7102 to calibrate all the thermocouples in the temperature range from 20°C to 105°C. The uncertainty in the temperature measurement was within ±0.05 °C. Figure II-6 shows the schematic of the positions of the thermocouples that are used to calculate the heat flux and surface temperature in the copper block. The uncertainty in the position of the centers of the thermocouples was estimated to be ±0.05 mm for a 0.25 mm thermocouple bead placed in a 0.30 mm diameter hole. The uncertainties in voltage and current were negligible (< ±0.12% and < ±0.05%, respectively). The uncertainty in the heat flux measurement was estimated using the Kline and McClintock method [60] to be ±10% at heat fluxes below 5 W/cm^2, ±6% at heat fluxes above 8 W/cm^2, and in the intermediate range, between ±6 and 10%. The uncertainty in the measured heat flux over the range 1 W/cm^2 to 30 W/cm^2 is shown in Table II-1 (with 95% confidence limits).

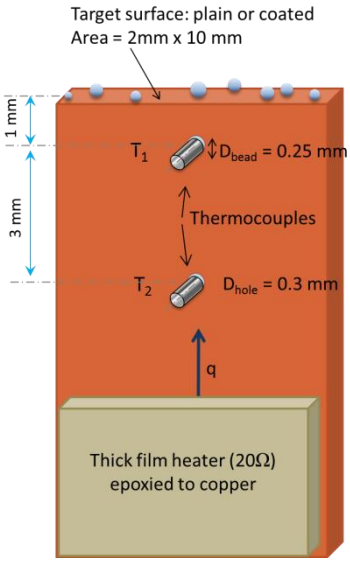

Figure II-6. Schematic view of heater-copper block-thermocouples showing the relative positions (not to scale).

Table II-1. Estimated uncertainty in the heat flux measurement at various input heat flux levels

q'' (nominal) (W/cm^2)	ΔT (°C)	$\pm\delta q''$ (W/cm^2)	% Uncertainty
1	0.076	0.294	29.4
5	0.38	0.515	10.3
8	0.61	0.49	6
10	0.76	0.6	6
30	2.25	1.8	6

Finite element analysis of heat conduction was conducted on the test article to quantify thermal losses, and to ensure that the heat flux could be reliably calculated using the two thermocouples, as shown in Figure II-7. A three-dimensional, computer-aided design model of the test article was created and imported into ANSYS Workbench for a steady-state heat transfer

simulation. The analysis was performed for multiple heat input levels, assuming a uniform heat transfer coefficient on the target surface, and a set of heat transfer coefficients for the different modes of heat loss. The heat loss modes included natural convection to the air surrounding the Teflon block, convective heat transfer to the liquid from the epoxy and Teflon surrounding heated copper block.

Figure II-7 shows the results of the simulation for two cases of input heat of 1.74 W and 5.83 W, with experimentally calculated pool boiling heat transfer coefficients (equation (II-3)) of 4200 W/m^2-K and 13200 W/m^2-K respectively. The boundary conditions are show in Figure II-7 (a). In the model, the input values were the power input ($q_{in} = V \cdot I$, where V is the voltage and I is the current through the cartridge heaters), the pool boiling heat transfer coefficient and the loss heat transfer coefficients. The set of coefficients for heat loss was obtained by iteratively trying different values until the temperatures obtained in the ANSYS model (and heat flux from the surface) matched the corresponding experimental values. The heat transfer through the different surfaces (including the copper target surface) and the temperatures at all points were the outputs. Figure II-7 (b) shows the temperature of the copper block along the direction of heat flow. Figure II-7 (c) and (d) show the temperature contours in the planes where the thermocouples are placed in the copper block (T_1 and T_2, respectively). In both cases, the temperature in each plane is uniform within 0.05 °C in both planes, and the average calculated temperature is within ±0.05 °C of the measured values. This confirmed that the pool boiling heat flux and surface temperature could be calculated using the temperatures measured by the two thermocouples.

Case 1:

Heat input q_{in} = 1.74 W;

Heat flux on surface q'' = 5.8 W/cm^2

Case 2:

Heat input q_{in} = 5.83 W;

Heat flux on surface q'' = 26 W/cm^2

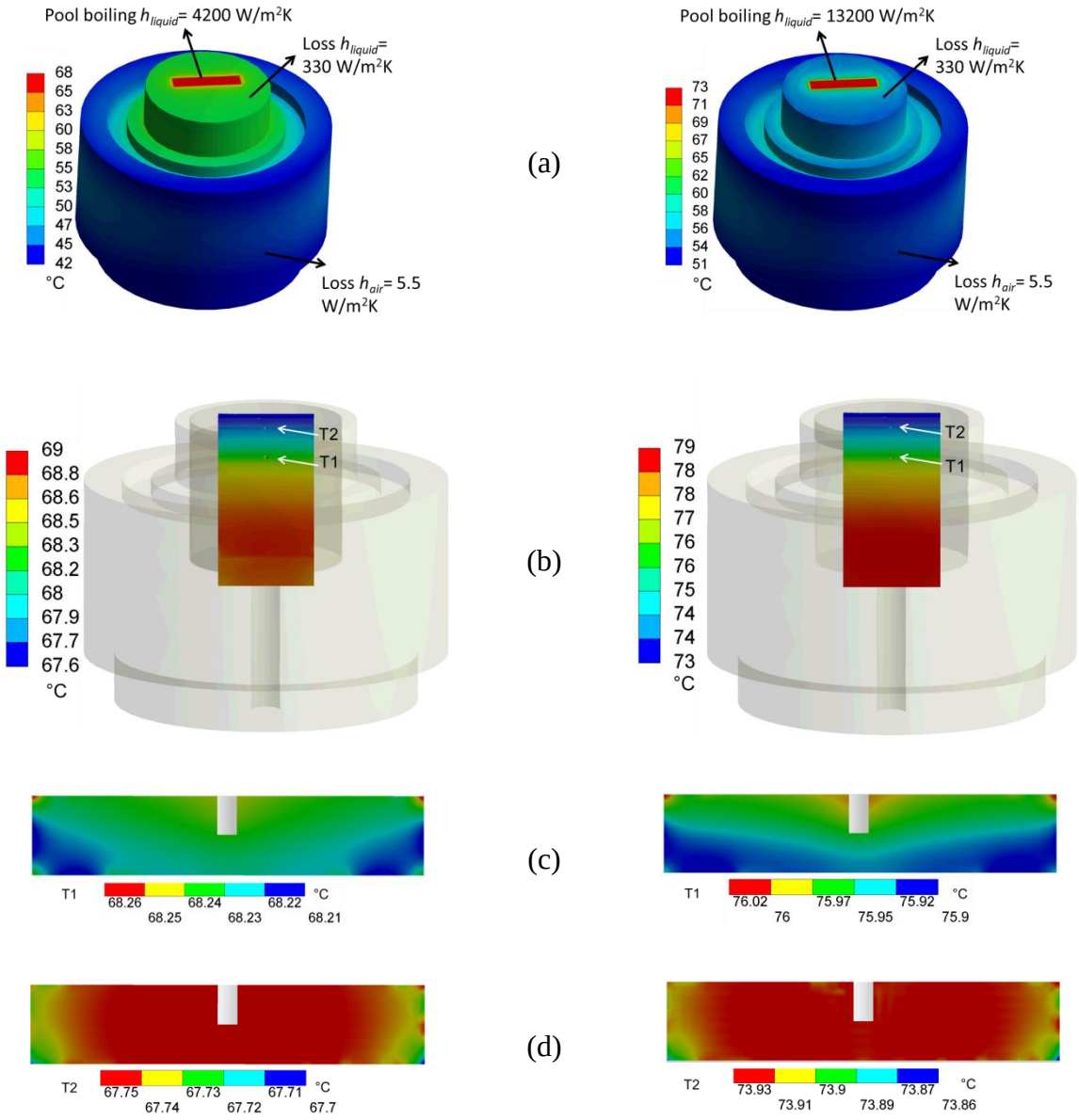

Figure II-7. (a) Results of steady-state thermal simulation: two cases, corresponding to heat input (1) q_{in} = 1.74 W (with h = 4200 W/m^2-K), and (2) q_{in} = 5.83 W (with h = 13200 W/m^2-K) are shown. (a) Boundary conditions applied to the various portions of the heater assembly, (b) Temperature contour in the copper block in the direction of heat transfer, (c) and (d) show the temperature contour plots in the plane perpendicular to the direction of heat conduction at thermocouple location: (T1) 4 mm from the surface, and (T2) 1 mm from the surface, respectively.

II.3 Results and Discussion

II.3.1 Experimental Boiling Curves

II.3.1.1 Measurements on 10 mm x 10 mm surfaces:

To verify that the pool boiling setup with visualization capability designed in this work could be used to obtain reliable data, a few tests were conducted using a 10 mm (width) x 10 mm (length) x 2 mm (depth) copper block in a setup similar to that used by El-Genk and Bostanci [59]. Saturated pool boiling heat transfer data of HFE-7100 by El-Genk and Bostanci [59] on a 10 mm x 10 mm plain copper surface that was sanded with a #1500 grit paper is shown in Figure II-8. In our comparison tests, only one thermocouple was placed at 1 mm below the surface to estimate the surface temperature. The heat flux through the surface was assumed to be equal to the q_{in} (= $V \cdot I$). As the design of this heater assembly is similar to [59] and [61], where simulations showed that the heat loss was below 2%, the losses in the current work are also assumed to be small, and therefore neglected.

The surface was polished using #1500 and #2000 grit paper resulting in roughness of 0.78 μm and 0.33 μm, respectively. As expected, Figure II-8 shows that the onset of nucleation (ONB) occurs at a higher superheat on the smoother sample (R_a = 0.33 μm) than that on the rougher sample (R_a = 0.78 μm). A lower heat transfer coefficient is observed on the smoother surface, as evidenced from the higher surface superheat temperature at the same heat flux. The variation of the critical heat flux due to the level of surface roughness was found to be within experimental uncertainties [62]. A repeated measurement on the 0.78 μm surface after a period of 44 hours of idle waiting (with the surface in contact with the liquid maintained at 20 °C after one cycle of measurement), showed that the ONB increased to 17 °C as compared to 11 °C in the measurement on the fresh surface. This indicates that the highly-wetting nature of HFE-7100

results in flooding and deactivation, of larger cavities, and thus the size of the nucleating vapor embryo changes over time despite the cavities' geometry remaining intact [62]. However, the changes in the heat transfer coefficient and the critical heat flux are found to be negligible.

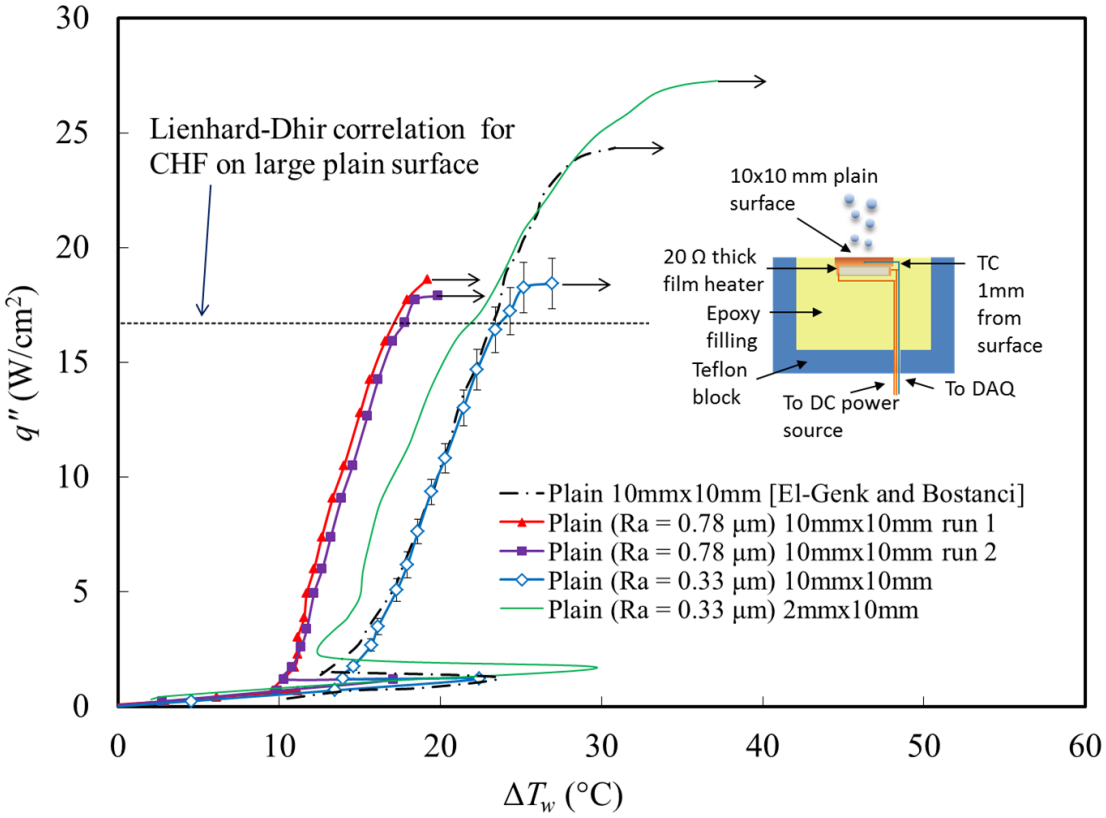

Figure II-8. Pool boiling curves on plain surface with target surface dimension 10 mm x 10 mm. A comparison is made with data from [59]. Inset shows the schematic of the cross-section of the test heater assembly. Data for the smooth plain surface of dimension 2 mm x 10 mm is shown here for comparison. The Lienhard-Dhir [63] correlation for CHF on an infinitely large flat surface gives 16.7 W/cm^2.

Based on hydrodynamic instability model, the critical heat flux on an infinitely large plain surface [63] is computed using the Lienhard-Dhir correlation, which gives a value of 16.7 W/cm^2 for HFE-7100. In our measurements, the 10 mm x 10 mm samples gave a slight higher value of ~ 18.5 ± 1.1 W/cm^2. Interestingly, the pool boiling curve corresponding to the surface polished with #2000 agreed closely with the data corresponding to the surface polished using #1500 in [59]. However, the critical heat flux that we obtained was significantly lower than ~25

W/cm^2 reported in [59]. Overall, we consider our measurement on the 10 mm x 10 mm surface to be in good agreement with literature. In Figure II-8, the pool boiling curve on a 2 mm x 10 mm target surface is also shown, which is also found to be in the same range as the larger surface in the nucleate boiling regime, while the CHF is enhanced as expected for the smaller target surface, consistent with [64].

II.3.1.2 Measurements on 2 mm x 10 mm surfaces:

Visualization of the bubble dynamics on the target surface requires unobstructed view of all the bubble sites to accurately measure the site density, diameter and frequency of departure. With the depth-of-focus of the lens limited to about 2 mm, and because when the width of the target surface was > 3 mm, the density of bubbles departing from the target surface closer to the lens obstructed the view of bubbles farther away, it was determined that the width of the target surface should 2 mm. However, if the target surface size is too small, boiling on the surface may become dominated by the surface tension effects rather than buoyancy, making the data unrepresentative of boiling on larger surfaces. By studying pool boiling data on target surfaces of different sizes under various acceleration-due-to-gravity levels, Raj et al. [65] determined that when the size of the target surface $L_h > 2.1L_c$, where $L_c = \left[\sigma/\left(g(\rho_l - \rho_v)\right)\right]^{1/2}$ is the capillary length, the boiling process is dominated by buoyancy rather than surface tension. At T_{sat} = 54 °C, the capillary length of HFE-7100 is 0.85 mm. The boiling characteristics on the 2 mm x 10 mm target surface is considered to be representative of larger boiling surfaces, since it satisfies the criterion $L_h = 2 \text{ mm} > 2.1L_c$.

(a)

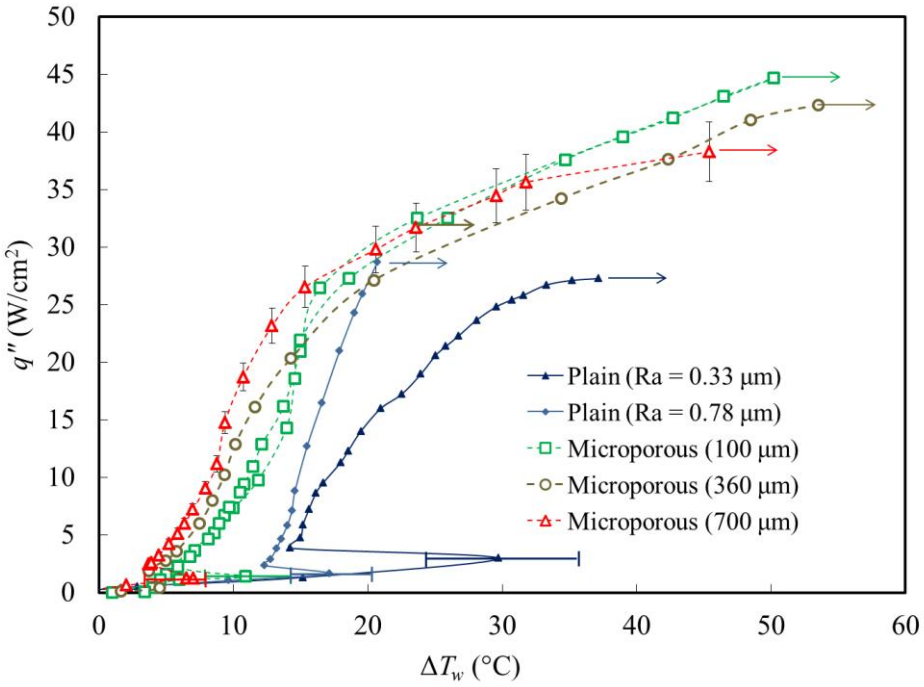

(b)

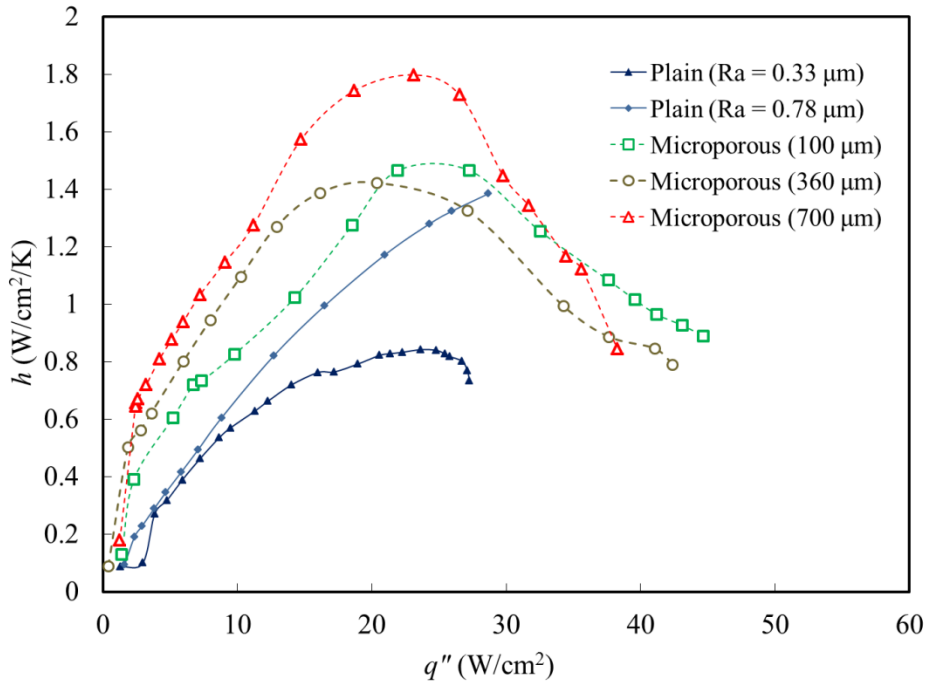

Figure II-9. (a) Pool boiling curves and (b) heat transfer coefficients for the various surfaces. Arrows denote CHF. Horizontal bars indicate the range of the onset of nucleate boiling superheat in different test runs.

Figure II-9 (a) shows the boiling curves obtained for the 5 surfaces with the surface area 2mm x 10 mm exposed to the liquid: two plain surfaces with different roughness (R_a = 0.33 μm and R_a = 0.78 μm) and three microporous copper surfaces with different thickness of coatings (with 100 μm, 360 μm, and 700 μm thick layer). As expected, the ONB, *h*, and CHF all differ with each other depending on the surface condition of these samples. As the heater power level is raised from zero, and the surface temperature is increased from the saturation temperature (corresponding to $\Delta T_w = T_w - T_{sat} = 0$), nucleate boiling on the surface does not start until the "onset" happens. The ONB results in a sudden reduction in the surface temperature, a phenomenon called "incipience temperature drop" which could result in damage to the device due to thermal shock [1]. This is particularly pronounced in highly wetting dielectric fluids such as HFE-7100, as they tend to flood even sub-micron cavities and deactivate them. Also, a large incipience superheat temperature can result in the temperature of the device exceeding the safe operating limit. For these reasons, the incipience overshoot needs to be eliminated or minimized. In the Figure II-9 (a), the ONB for the two plain surfaces is as high as 17 – 38 °C. The difference in the ONB is due to the difference in the surface roughness (see Figure II-5) and the resultant variation of the size of the cavities that allow for initiation of bubble nucleation. In comparison, the ONB superheat on the microporous surfaces occurs at temperatures below 11 °C, which would be much more favorable for use in electronics cooling. Repeated measurements showed that the ONB superheat varies by as much as ±7 °C on the plain surfaces. The variation between the fresh and reworked surface is likely due to the random manner in which cavities of various sizes are activated resulting in nucleation, and/or due to the flooding of some cavities in the reworked surface which results in no embryo for nucleation [66].The ONB superheat is much more repeatable on the microporous surface, with only ±3 °C variation.

The Laplace-Young equation describes the pressure difference across the surface of a vapor bubble $P_v - P_l = 2\sigma/r$, where P_v is the vapor pressure, P_l is the liquid pressure, r is radius of curvature of the bubble and σ is the surface tension. Along with the Clausius-Clapeyron relation, the Laplace-Young equation is used to estimate the critical diameter at bubble nucleation from the ONB [66], resulting in the equation:

$$D_{crit,CC} = \frac{4\sigma T_{sat}}{\rho_v h_{lv} \Delta T_{w,ONB}}, \qquad \text{(II-4)}$$

where σ is the liquid surface tension, T_{sat} is the saturation temperature, ρ_v is the vapor density, h_{lv} is the latent heat of vaporization, $\Delta T_{w\,ONB}$ is the wall superheat at the onset of nucleate boiling. The critical diameter is an estimation of the diameter of the cavity where a vapor nucleus can grow into a bubble without condensing, at a given wall superheat. The prediction given by equation (II-4) is appropriate when the contact angle is large ($\phi \sim 90°$), the incipience superheat is small, and the saturation curve is nearly linear over the range from the saturation temperature of the liquid to the temperature of the superheated vapor within the bubble [67]. However, for a highly wetting liquid, the incipience superheat at ONB can be large, and thus the relation between T_{sat} and P_{sat} would be non-linear, thereby invalidating the use of the Clausius-Clapeyron relation [and hence equation (II-4)]. An equivalent expression that takes into account the non-linearity is given [67] by the following equation:

$$\Delta T_{w,ONB} = T_{w,ONB} - T_{sat}(\text{at } P_l) \cong T_{sat}\left(P_l + \frac{4\sigma\left(\text{at } T_{w,ONB}\right)}{D_{crit}}\right) - T_{sat}(\text{at } P_l). \qquad \text{(II-5)}$$

The relation between T_{sat} and P_{sat} for HFE-7100 [39] is given by:

$$\ln(P[\text{pascal}]) = \frac{-3641.9}{T[\text{kelvin}]} + 22.415. \qquad \text{(II-6)}$$

The critical diameters of the nucleating cavity computed using the minimum and maximum values of $\Delta T_{w\,ONB}$ from equations (II-5) and (II-6) for the various surfaces are shown

in Table 2. The data shows that the microporous surface contains cavities > 1 μm that can get activated at low superheats, resulting in onset of nucleation much before plain surface. Figure II-10 shows the critical diameters for the various surfaces plotted as a function of the surface superheat, overlaid on a plot of the size range of active nucleation sites calculated using Hsu's criterion [68] for a variety of contact angles. The fact that many of the measured data points lie outside the curves corresponding to $\phi \leq 7.5°$ suggests that the relevant contact angle of liquid-vapor interface is higher than the static contact angle (< 1°). Due to the highly wetting nature of the HFE-7100 fluid, the critical cavity diameter may not correspond to the feature dimensions observed under microscope, but indicate the size of largest trapped vapor/gas embryo [69].

Table II-2. The range of superheat temperatures at onset of nucleate boiling on the different surfaces, and the corresponding critical nucleating embryo sizes.

Surface	Range of $\Delta T_{w,ONB}$ (°C)	Range of D_{crit} (μm)
Plain (R_a = 0.33 μm)	24.5 – 36.2	0.17 – 0.35
Plain (R_a = 0.78 μm)	14 – 24.3	0.37 – 0.85
Microporous (100 μm)	9 – 10.9	1.2 – 1.6
Microporous (360 μm)	3.4 – 10.1	1.4 – 7
Microporous (700 μm)	3.2 – 7	2.3 – 7.8

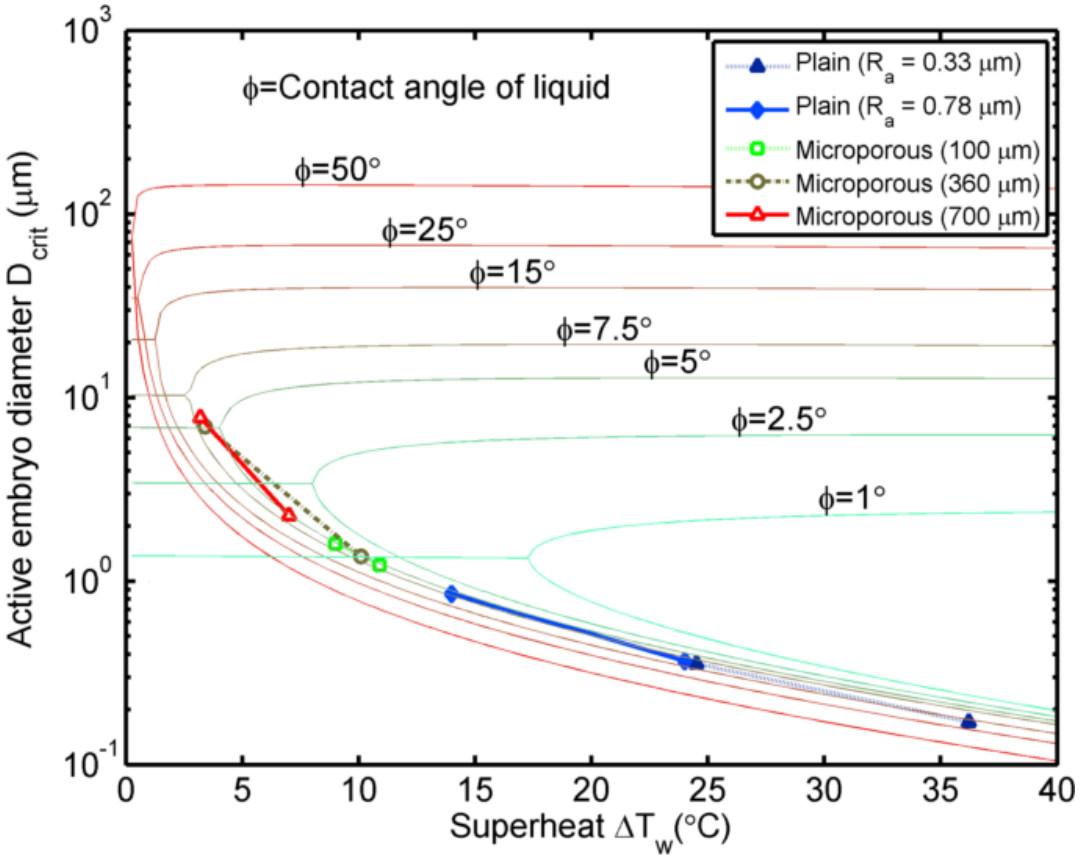

Figure II-10. Predicted size range of active cavity sites as a function of wall superheat based on Hsu's criterion, for the range of contact angle $1° < \phi < 50°$. The active sites are located in the concave portion of each curve. The range of critical diameters of the nucleating embryo calculated using equation (II-5) for each of the different surfaces from the superheat temperature at ONB is also shown.

Figure II-9 (a) also shows that the CHF on the microporous surface is enhanced by about 33 – 60% as compared to that on the plain surfaces. Though the difference is small, the CHF decreases monotonically with increase in the microporous layer thickness. This is likely due to the choking of the liquid pathways occurring at a relatively lower heat flux level in the thicker layer. Figure II-9 (b) shows the heat transfer coefficient as a function for the heat flux. The *h* is enhanced by 50 to 270% on the microporous surfaces over the plain surfaces. The *h* on the 700 μm microporous sample is the highest of all in the isolated-bubbles and fully-developed nucleate boiling regimes. The *h* in this regime increases with the increasing thickness of the layer. This is

probably due to the presence of a larger number of nucleating sites within the thicker layer, resulting in more intensive phase-change heat transfer. At wall superheat > 15°C (corresponding to heat flux > 20 to 25 W/cm^2) the slopes of the boiling curves (Figure II-9 (a)) of the microporous surfaces start to decrease, resulting in the reduction in the *h* after reaching the peak value. At high heat fluxes, the increased rate of vapor generation and motion from within the layer to outside leads to the decrease in the pathways available for liquid reflow which leads to a decrease in the heat transfer coefficient.

Figure II-11 shows the boiling curves (with saturated HFE-7100 at about 1 atm) on different kinds of enhanced surfaces from the literature (Kwark et al. [70], El Genk and Parker [71] and Liu et al. [72]), along with the microporous surfaces in the current study. The plain surface (baseline) boiling curves from each study are also shown. Kwark et al. [70] performed experiments with 1 cm^2 surface made with Al_2O_3 nanocoating. The nanocoated surface was actually seen to result in degraded thermal performance which was attributed to the increasing wetting resulting in lesser nucleation site density. El-Genk and Parker [71] studied pool boiling on 1 cm^2 porous graphite (PG) surface. The PG surface resulted in almost zero onset of boiling overshoot, unlike the plain surface which resulted in ONB at superheat of ~ 40°C. The CHF was enhanced by ~50%. Liu et al. [72] performed pool boiling tests on surface covered with stainless steel meshes of various sizes. The mesh helped the thermal performance at low temperatures, but resulted in degraded performance in the fully developed nucleate boiling regime and the CHF. Visual observations indicated that meshes retarded the removal of the vapor from the surface, resulting in a thick vapor film and thereby reduced heat transfer. In comparison, the microporous surface in the current study is found to reduce the ONB, increase heat transfer in the nucleate boiling regiume, and also enhance the CHF.

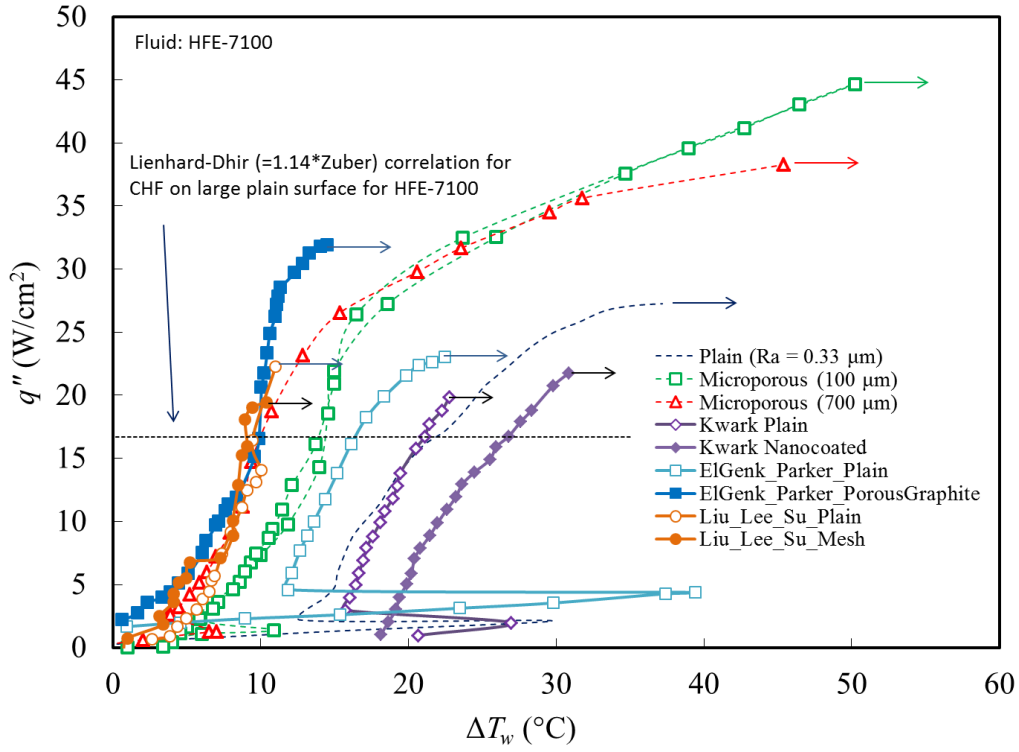

Figure II-11. Boiling curves with HFE-7100 on various enhanced surfaces, and similarly sized plain surfaces (baseline) from the literature, compared to the microporous surface in the current study.

II.3.2 Bubble Dynamics

High-speed visualization offers the possibility of obtaining detailed and temporally resolved information on the dynamics of bubbles growth and departure from the target surface at a high magnification level (25 – 30 x). In the following sections, we will discuss the bubble dynamics on various surfaces as measured using high-speed video. Visualization measurements were used to obtain the bubble characteristics up to a heat flux (and surface superheat) value that allowed for discerning individual bubbles. The crowding of the bubbles on the surface and their coalescence make measurements beyond this heat flux (~ 10 W/cm^2) difficult and not reliable. Figure II-12 shows representative images of bubble dynamics on plain and microporous surfaces at various heat flux levels.

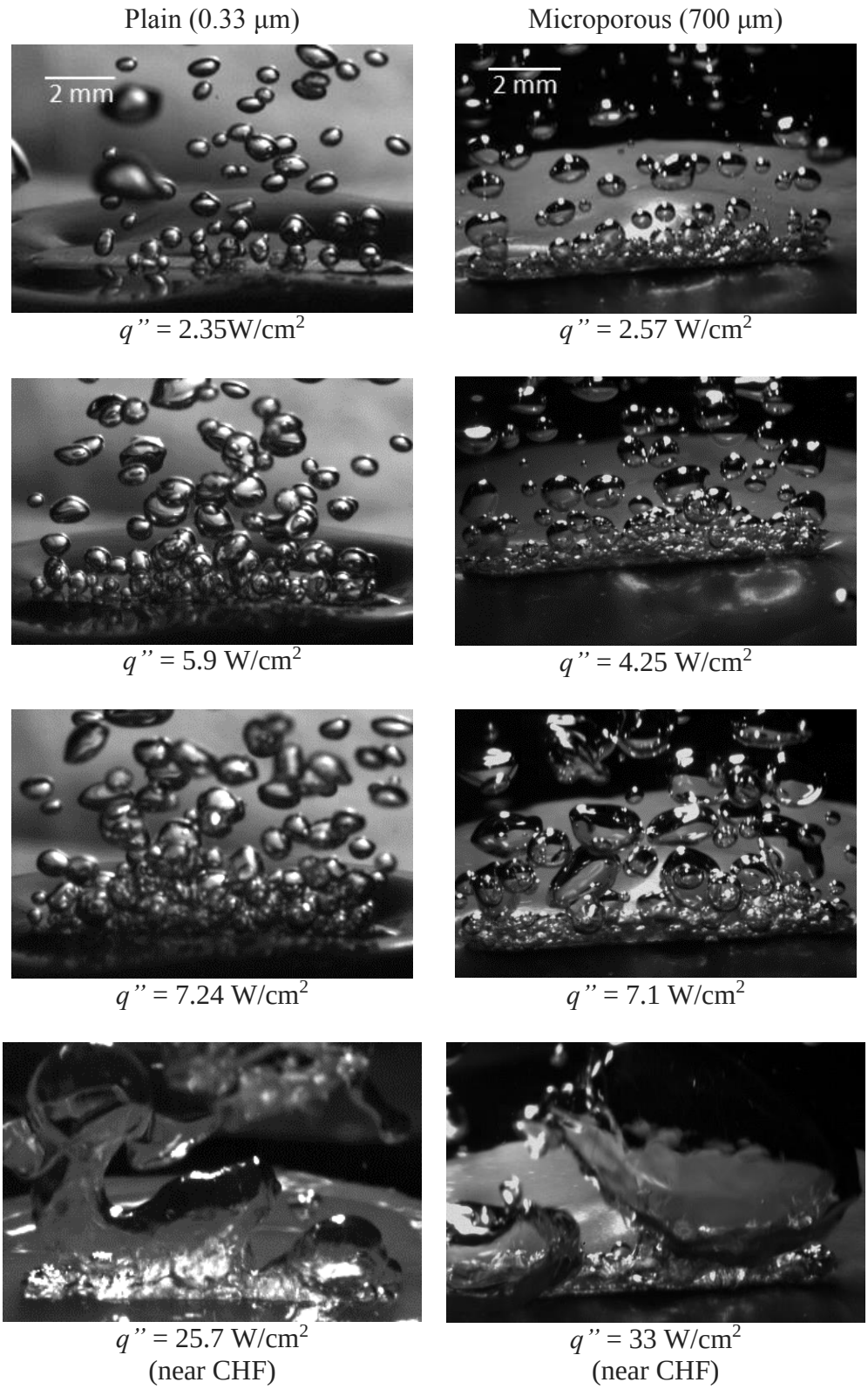

Figure II-12. Images of bubble dynamics on a plain and a microporous surface at various heat flux levels.

II.3.2.1 Bubble site density:

Each video file was analyzed to determine the locations of the active nucleation sites on the test surface. The instantaneous number of active sites captured by a still frame was generally not as high as the total, cumulative number of sites that were active at least once over several departure periods [73]. The cumulative number of sites was determined by counting all the sites that were active over any part of an arbitrarily selected 100 frames that represented several bubble cycles. The area density of active nucleation sites N was then calculated by dividing the counted number of active sites by the area of the surface. The uncertainty in the measurement is estimated to be 10% for low heat fluxes and up to 20% for high heat fluxes where the field of view was frequently obstructed, by repeatedly counting the number of active sites on successive sets of 100 frames each. The number of active sites increased with increasing wall superheat and with increasing surface roughness for the plain surface. Incipience of nucleate boiling on the microporous surface occurred at a much lower temperature; and consequently, the bubble site density in the microporous surface was many times higher than that of the plain surface at any given superheat.

Figure II-13 and Figure II-14 show the nucleation site density as a function of the wall superheat on the plain and microporous surfaces, respectively. Since nucleation in the microporous surface takes place within the layer, the visual image only gives us the number of sites of bubble release from the surface. Hence, site density is referred to as "bubble site density" to be more general. As expected, the plain surface with the higher roughness level produced more bubbles than the smoother plain surface. In regard to the microporous surfaces, the bubble site density was observed to increase strongly with the increasing temperature. However, no clear pattern in terms of the site density versus the layer thickness could be discerned.

The bubble site density on the plain surfaces were compared with models developed by Hibiki-Ishii (H-I) [74], Kocamustafaogullari-Ishii (K-I) [75], and Benjamin-Balakrishnan (B-B) [76] models.

(a)

(b)

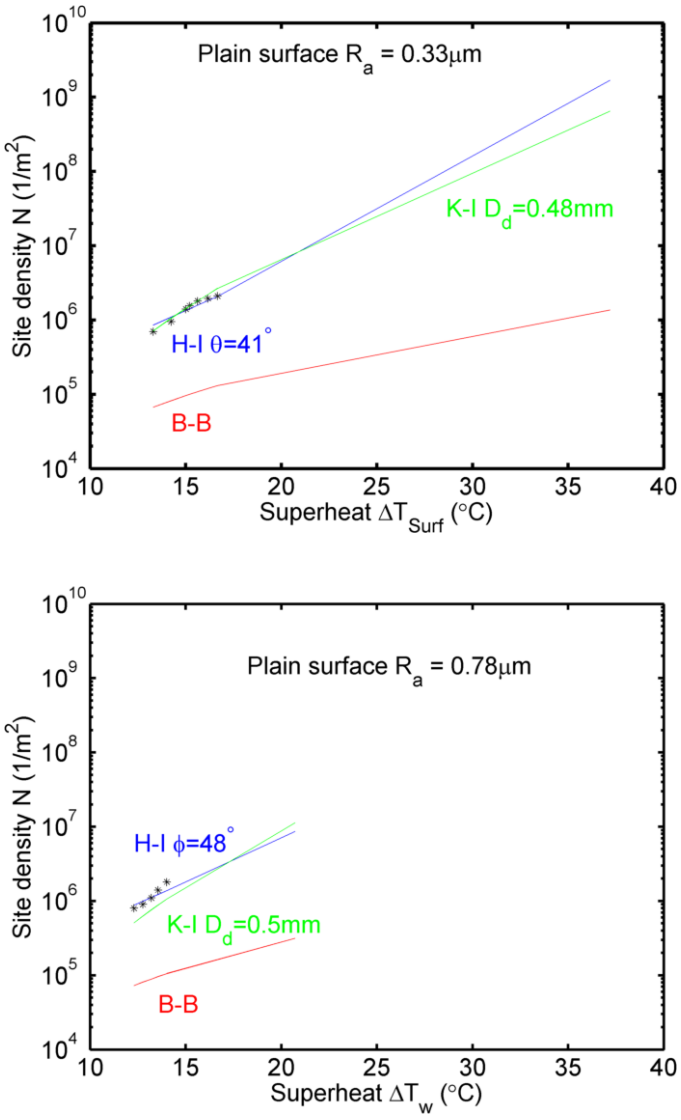

Figure II-13. Experimental measurements of bubble site density compared with correlations for the two plain surfaces of roughness (a) 0.33 μm, and (b) 0.78 μm. The extended range corresponds to the superheat up to the CHF.

The H-I correlation was developed by fitting to a wide array of experimental nucleation site density data for boiling on plain surfaces. They assumed that nucleating cavity number and size distributions would be statistically similar for most boiling systems, accounting for surface

characteristics by including a static contact angle term. However, given the static contact angle of HFE-7100 is < 1°, the predicted values of the site density (N_{HI}) were several orders of magnitude smaller than the experimentally observed values (N).

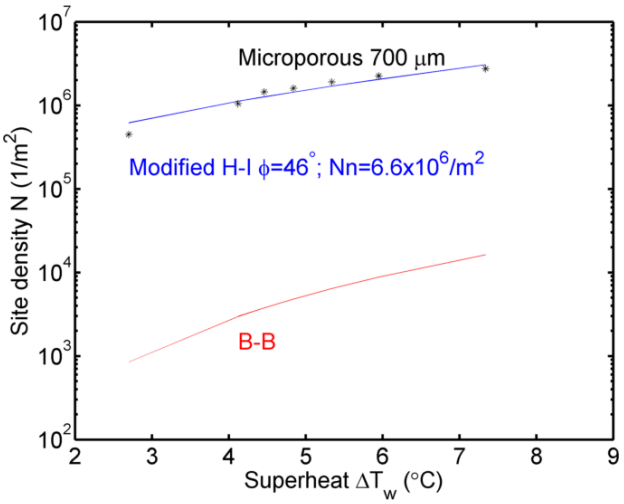

(a)

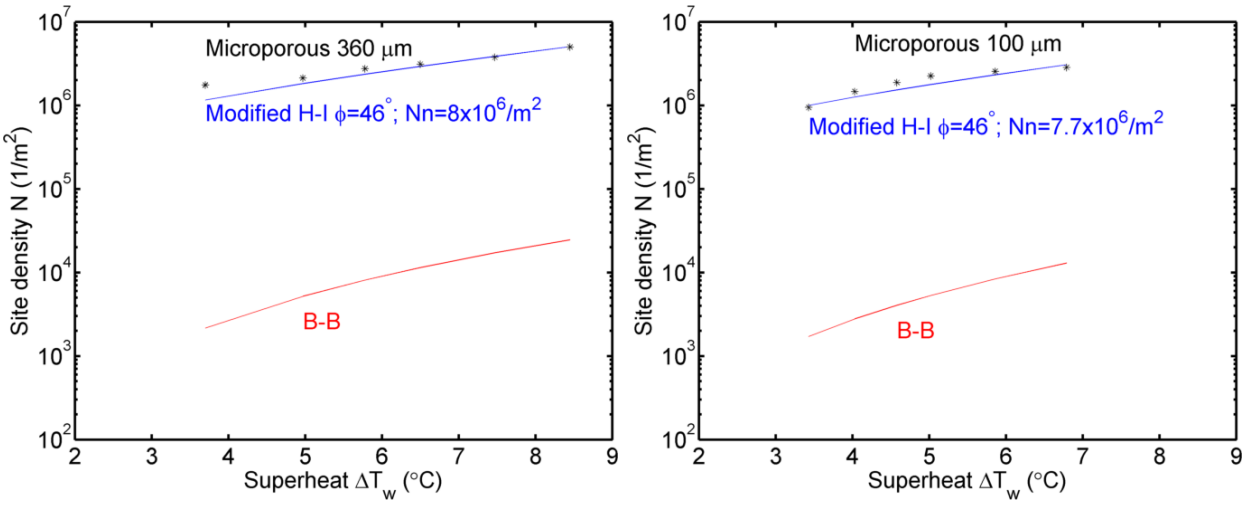

(b) (c)

Figure II-14. Experimental measurements of bubble site density compared with correlations for the microporous surfaces of thickness (a) 700 μm, (b) 360 μm, and (c) 100 μm.

Very good agreement was obtained if ϕ was assumed to be 40 to 50° for the plain surfaces, with only the contact angle being the varying parameter. It is reasonable to assume that

during a nucleate boiling process, the dynamic contact angle (which tends to be much larger than the static contact angle, and dependent on the velocity of the liquid-vapor interface) is the relevant parameter [77], instead of the static contact angle. This is reinforced by the observation that active nucleation cavity sizes lie outside of the size range given by Hsu's criterion with contact angle < 7.5°, as discussed in section II.3.1.2. The H-I correlation is given by the following set of equations:

$$N_{HI} = N_n \left\{1 - \exp\left(-\frac{\phi^2}{8\mu^2}\right)\right\}\left[\exp\left\{f(\rho^+)\frac{\lambda'}{R_c}\right\} - 1\right]$$

$$R_c = \frac{2\sigma\{1 + (\rho_v/\rho_l)\}/P_l}{\exp\{h_{lv}\,(T_w - T_{sat})/(RT_wT_{sat})\} - 1} \qquad \text{(II-7)}$$

$$f(\rho^+) = -0.01064 + 0.48246\rho^+ - 0.22712\rho^{+2} + 0.05468\rho^{+3}$$

$$\rho^+ = \log_{10}\left(\frac{\rho_l - \rho_v}{\rho_v}\right),$$

where $N_n = 4.72 \times 10^5$sites/m^2, μ = 0.722 rad, and λ' = 2.5 x 10^{-6} m. R is the gas constant based on the molecular weight. For HFE-7100, R = 33.24 J/(kg-K).

For the three microporous surfaces, the contact angle is kept constant at ϕ = 46°, and only N_n is varied to obtain good fits to the experimental data. The N_n in the H-I correlation is a coefficient that is related to the average cavity density on (smooth) surfaces. Therefore, it is reasonable to assume that this could be the parameter that varies in the microporous surfaces depending on the thickness.

The K-I model assumes that the nucleation site density and the critical cavity radius can be normalized by the length scale of the bubble departure diameter. Using the departure diameter experimentally obtained (rather than use the Fritz correlation as recommended), reasonably good agreement was obtained for the plain surfaces (Figure II-13), while it severely underpredicted the

N on the microporous surfaces. The B-B model only takes into account the average surface roughness, and also was found to underpredict the observed *N* by over an order of magnitude.

Figure II-15 shows the experimentally measured *N* along with the predictions based on the H-I correlation for all the surfaces. The bubble site density is assumed to increase with the superheat temperature up to a value given by the condition of maximum bubble packing density on the surface. After that superheat value, the bubble site density is assumed to be constant.

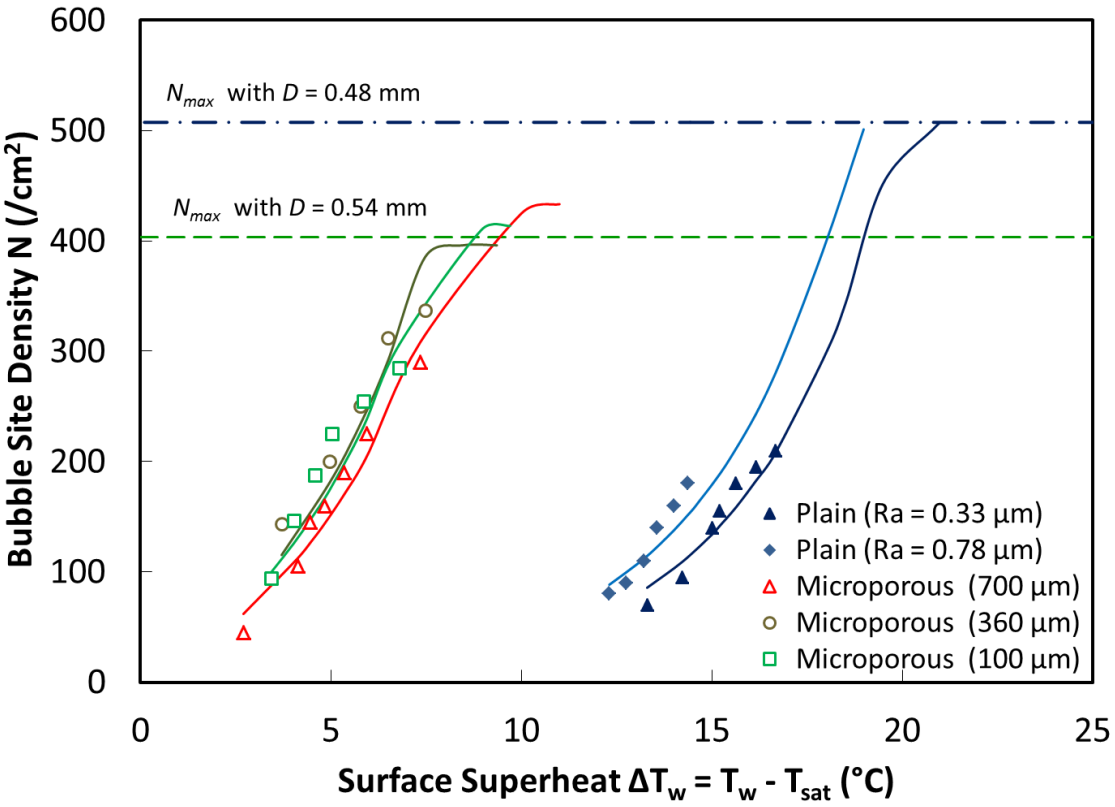

Figure II-15. Bubble site density at departure on the various surfaces as measured using the high-speed video. The symbols are the measurements, and the solid lines are the fits based on Hibiki-Ishii correlation. N_{max} represents the maximum bubble site density when the surface is fully covered by bubbles at the respective departure diameter.

II.3.2.2 Bubble departure diameter:

As a bubble grows in size, buoyancy eventually becomes larger than the force that pins the bubble to the surface. Using the videos, the bubble departure diameter was calculated by

averaging three diameter measurements immediately after the departure over a period of about 1.5 to 3 milliseconds. Based on repeated measurement of the bubbles, it was determined that the diameter measurements obtained from the images have an uncertainty of ±15%. The uncertainty is due to error in locating the bubble edges, the time-dependent non-spherical shape of the bubbles and, the fact that the bubbles emanating from the same site over multiple cycles also differ in size. The departure diameter also varies with the site. In all the experiments, the bubble diameters varied between 0.2 to 0.8 mm, with a majority around 0.45 to 0.6 mm. The average bubble departure diameters for the various surfaces are shown in Figure II-16. The average diameter seems to be only weakly dependent on the superheat temperature on all the surfaces, and decreases slightly with increasing temperature. The average diameter at departure is about 0.5 mm on the plain surfaces. The bubble diameter at departure on the microporous surface is a little higher (~0.55 to 0.6 mm) than on the plain surfaces. This is probably due to the fact that the bubble growth in the case of the microporous surface happens due to vapor generation within the microporous layer, in addition to the growth that takes place due to evaporation after the bubble comes outside of the microporous layer. Since the cavity sizes are larger on the microporous layer relative to the plain surface, the surface tension force that pins the bubble to the surface will also be higher, thereby allowing the bubble to grow larger than that on the plain surface before departure.

Several correlations have been proposed in the literature to predict the bubble departure diameter in pool boiling. The experimentally measured diameter are compared to correlations proposed by Cole [78], Kutateladze and Gogonin [79], Jensen and Memmel [80] and Phan et al. [81] in Figure II-16. Of these, the correlation by Phan et al., shown in equation (II-8), predicted the trend and values of the experimental data most closely (with the contact angle ϕ = 41° to 46°,

same as the value used in the Hibiki-Ishii correlation for nucleate site density). This is an empirical correlation, developed with pool boiling of water on nanocoated surface resulting in the contact angle in the range $20° < \phi < 110°$:

$$D = 0.63 \frac{(2 + 3\cos\phi - \cos^3\phi)}{4} L_c, \qquad \text{(II-8)}$$

where L_c is the capillary length and ϕ is the contact angle. At heat flux levels q'' > 8 to 10 W/cm^2, lateral coalescence (between bubbles adjacent to each other on the surface) and vertical coalescence (between subsequent bubbles at the same site) became significant enough to render the measurement impossible.

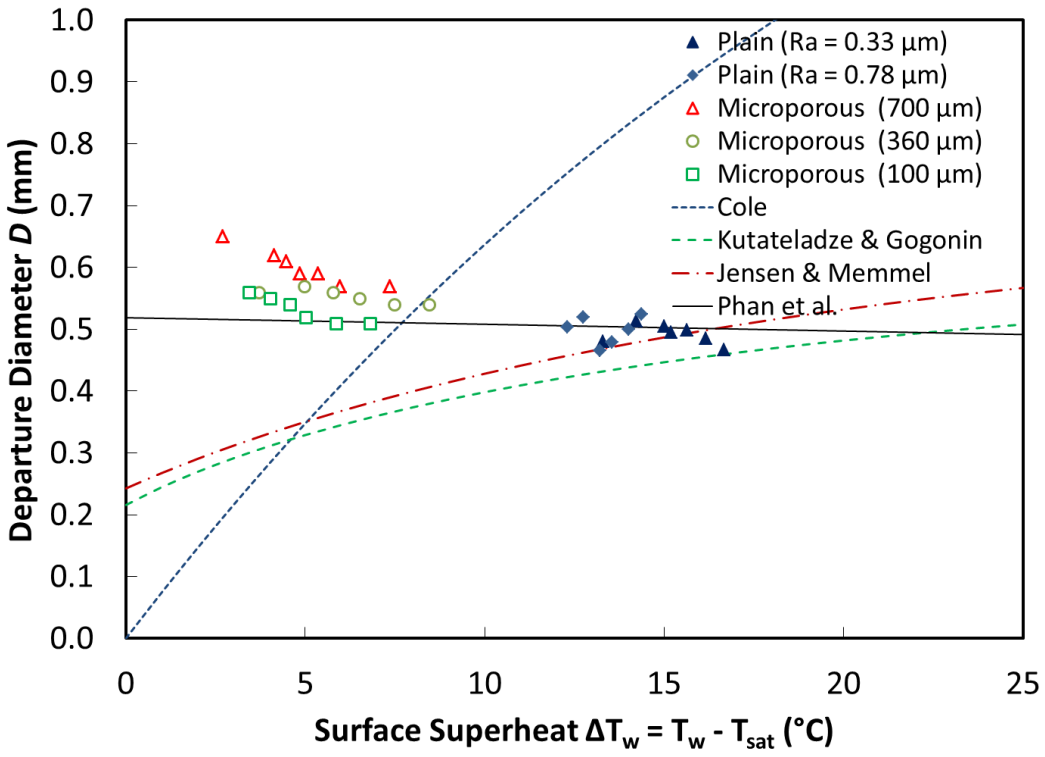

Figure II-16. Average bubble departure diameter for the various surfaces. Predictions based on several different models are also shown. The best agreement was found using the model from Phan et al. [81] with the same contact angle as used for the nucleate site density correlations.

II.3.2.3 Bubble departure frequency:

The number of bubble cycles per unit time at a given cavity location is defined as the bubble departure frequency. In the high-speed video files, bubbles growing at a location, within ~ ±0.2 mm, were all considered to be formed at the same nucleating cavity site. The bubble departure frequency was estimated by observing the number of bubbles that departed from a given nucleation site over a period of time (about 200 frames, corresponding to a time period of about 10 milliseconds). An average of the frequency of departure at a few sites (3 to 5) that are approximately of the same diameter at departure was taken to be the average departure frequency. The uncertainty in departure frequency is estimated to be ± 13%, based on the measurements from several sets of the bubble sites. The average value of the measured bubble departure frequencies are plotted with respect to the surface superheat temperature in Figure II-17, along with linear fits for each surface. On all the surfaces, the bubble departure frequency increases steeply with the superheat temperature. At the heat flux levels > 8 to 10 W/cm^2, increased lateral bubble mergers made frequency measurements meaningless. In a bubble growth cycle, with t_g being the bubble growth period, and t_w the waiting period (between bubble departure and inception of a new bubble) at a given site, the frequency is essentially $f = 1/(t_g + t_w)$. In the experiments, at all heat flux levels, it was found that the bubble cycles were nearly continuous (that is, $t_w \ll t_g$). This is different from the $t_w > t_g$ observed during pool boiling of water [56]. This implies that transient conduction of heat from the surface to the liquid in the waiting period may not be a significant factor in our study, unlike the observation with pool boiling of water in [56], where the transient conduction was found to be the dominant mode of heat transfer. Moghaddam and Kiger also observed in single-bubble pool boiling with FC-72 that the waiting period was often small [51].

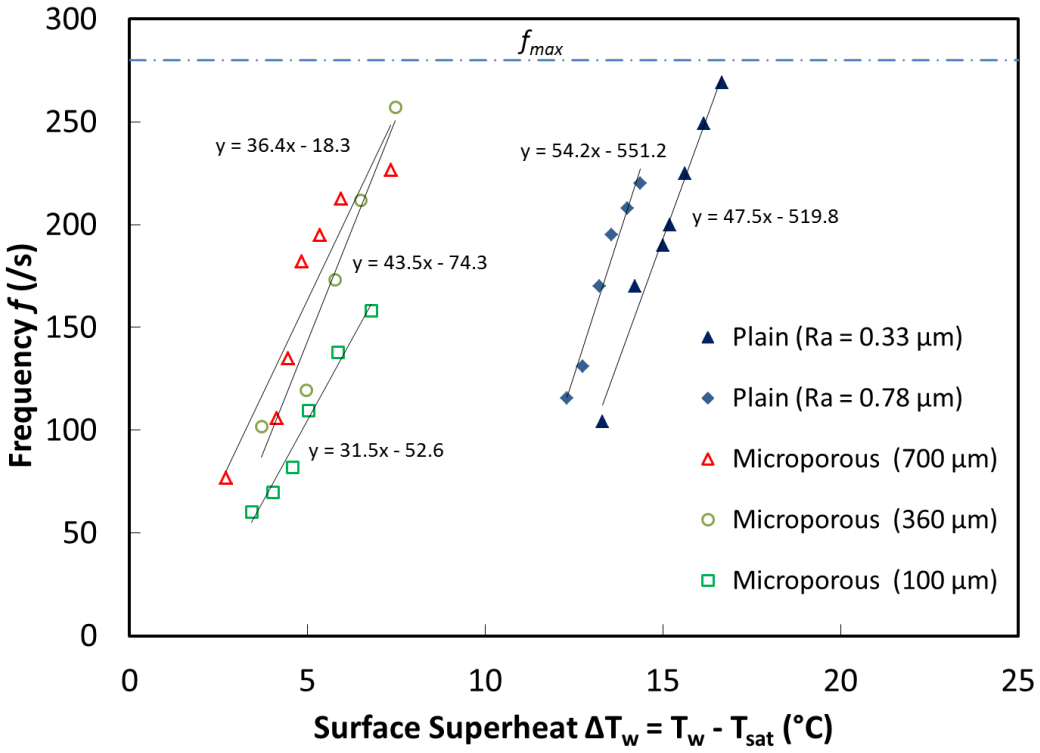

Figure II-17. Average frequency of bubble departure for the various surfaces as a function of the superheat. The solid lines and equations in each case represent linear data fits, with y = f and x = ΔT_w.

For the microporous surface, once again the frequency of bubble departure does not seem to be clearly dependent on the thickness of the layer, though the thickness appears to positively affect the frequency. This again is probably due to the fact that the thicker layer allows higher rate of vapor generation.

Peebles and Garber [82] developed the following correlation for the relation between the frequency and bubble departure diameter, for the case where the bubble waiting time is negligible:

$$Df = 1.18\left(\frac{t_g}{t_g + t_w}\right)\left[\frac{\sigma g(\rho_l - \rho_v)}{{\rho_l}^2}\right]^{0.25}, \qquad \text{(II-9)}$$

where σ is the surface tension of the liquid, g is the acceleration due to gravity, ρ_l is the density of the liquid, and ρ_v is the density of the vapor. Because $t_w \ll t_g$, the term in the parentheses ~ 1. For the plain surface with the D ~ 0.5 mm, this gives f ~ 214/s, which is in the observed frequency range in the present study. However, because the diameter at departure is relatively constant with temperature, this equation implies that the frequency also should be constant, which is contrary to the measured data. The other departure frequency correlations tested [5] also do not seem to be applicable to the pool boiling of HFE-7100, in magnitude and trends [83].

II.3.3 Partition of Heat Flux

The heat flux partition model has been commonly used for mechanistically predicting the nucleate boiling heat transfer. In the model proposed by Bowring [84], the total heat transfer in a boiling process is partitioned into single-phase heat and phase-change heat. The former refers to the amount of heat that is transferred to the cold fluid to raise its temperature above the saturation temperature, and the latter refers to the heat going into changing the phase of the liquid into vapor. The single-phase heat flux can be further subdivided into natural convection at the locations on the target surface that are not nucleating bubbles, and are far enough away to be unaffected by the churning motion of the liquid induced by the bubble motion.

The phase-change heat transfer is calculated from the total volume of vapor generated based on bubbles from all the nucleation sites. The volume of vapor generated is estimated from the vapor bubbles in the liquid just after they leave the surface. Originally developed for flow boiling, it has been applied to pool boiling also. Gerardi et al. [56] applied the partition model to pool boiling of deionized water and nanofluids, and found that partition model was capable of predicting the correct order of magnitude of the heat flux, though the error was typically large.

At the lower heat fluxes in the isolated-bubble regime, the following equations are used to obtain the three heat flux partitions.

1. The phase-change heat flux ($q"_{evap}$) is calculated from the total volume of vapor generated based on bubbles from all the nucleation sites:

$$q"_{evap} = \frac{\pi}{6A}\rho_v h_{lv}(N \cdot D^3 \cdot f). \quad \text{(II-10)}$$

2. The single-phase portion of the heat transferred to the liquid is considered to be due to: (1) natural convective heat transfer, $q_{NatConv}$, at locations undisturbed by the bubble activity, calculated using the McAdams correlation [85]. and due to (2) the "quenching heat flux" which refers to the amount of heat transferred to the cooler fluid that rushes to the surface after a bubble departs, which is the heat that is expended in the formation of a new thermal boundary layer after the departure of the bubble from the previous cycle [86]. The quenching heat flux ($q"_{quench}$) is a transient heat conduction process and is modeled by the heat conducted to a semi-infinite layer of fluid during the waiting time between bubble cycles.

$$q"_{quench} = \frac{2\pi k_l \Delta T_w}{\sqrt{\pi \alpha_l}} N D^2 f \sqrt{t_w}, \quad \text{(II-11)}$$

where k_l is the thermal conductivity of the liquid, α_l is the thermal diffusivity of the liquid, t_w is the waiting time period. From space- and time-resolved studies on pool boiling of a single bubble, Demiray and Kim [87], and Moghaddam and Kiger [40] observed that the transient heat conduction to the liquid happens not only during the "quenching process" during the waiting period, but also throughout the bubble growth and departure duration. Assuming gradual rewetting of the target surface by the liquid front after departure of a bubble, and for the limiting

condition cases with very small waiting time, they [40] derived the following equation for the transient conduction heat flux:

$$q"_{quench} = 2.15 \frac{k_l(0.65\Delta T_w)}{\sqrt{\pi \alpha_l}} \left(N \cdot D^2 \cdot \sqrt{f}\right). \qquad \text{(II-12)}$$

As mentioned previously, from the visualization experiments, we found that the waiting time was much smaller than the bubble growth time. Thus equation (II-12) provides a physical picture that is closer to the observation than the quenching model based on the waiting time, equation (II-11). The total heat flux was then computed as the sum of the three components—phase change heat flux, transient conduction heat flux and natural convection: $q_{total\ proj} = q_{evap} + q_{quench} + q_{NC}$. The site density, departure diameter and frequency measurements made in the isolated-bubbles regime were extrapolated to higher superheat temperatures up to the CHF using the correlations discussed previously. In addition, the site density was assumed to reach a maximum (N_{max}) corresponding to the fully-packed condition, and the frequency at f_{max} = 280/s after which vertical bubble coalescence became large. Bubble interactions and coalescence and their effect on the heat transfer are not accounted for in these models. Using these equations, the heat flux partition for the plain and microporous coated surfaces was obtained.

II.3.3.1 Plain surfaces:

Figure II-18 (a) and (b) show the heat flux partition calculated from the *N*, *D* and *f* on the plain surface (with R_a = 0.33 μm and 0.78 μm, respectively) as a function of the superheat. The solid symbols indicate the partition fluxes calculated using the experimentally obtained bubble parameters. The open symbols denote the partition fluxes calculated using the projected values of *N*, *D* and *f* from the correlations.

(a) Plain smooth (R_a = 0.33 μm)

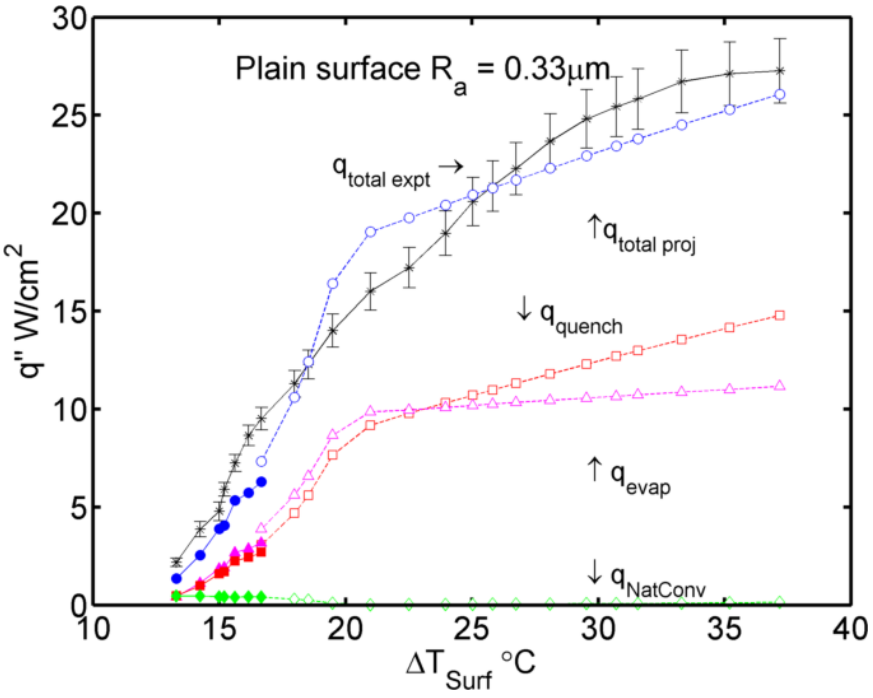

(b) Plain rough (R_a = 0.78 μm)

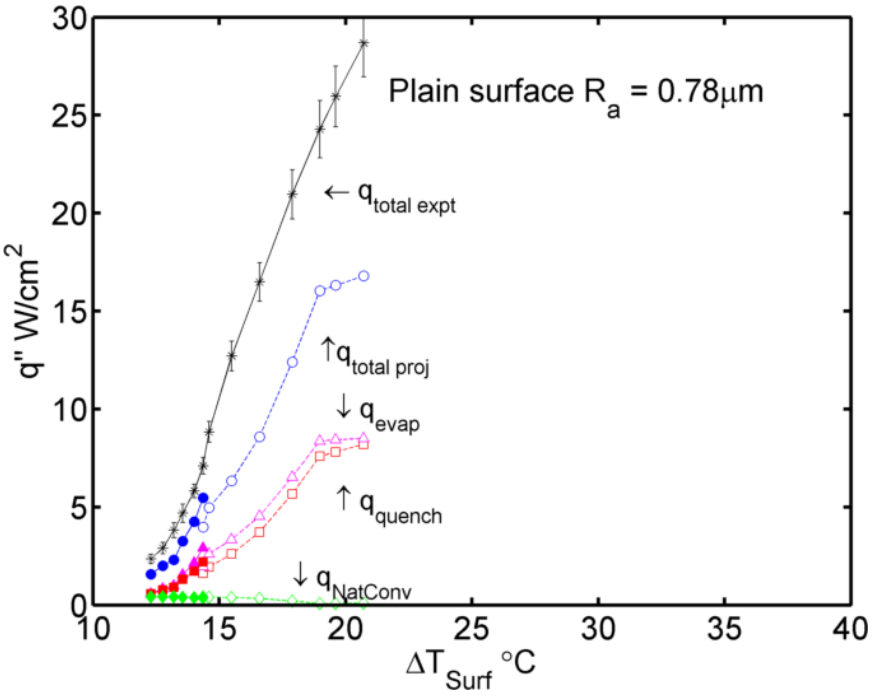

Figure II-18. The partition of heat flux model applied to the plain surfaces: (a) Smooth (R_a = 0.33 μm); (b) Rough (R_a = 0.78 μm). The solid line with * markers is the experimental data. The solid markers denote the data points of *N*, *D* and *f* from experiments, and the open symbols denote the data from extrapolated *N*, *D* and *f*.

Based on the partition model, the proportions of heat that goes into evaporative, quenching and convection modes are plotted in the figures. The natural convection mode contributes little due to the small area of convection and the low natural convection heat transfer coefficient, and it decreases very quickly with increasing superheat. The evaporative and quenching (transient conduction) components contribute most to the total heat flux, and nearly equally (both contributing about 40 to 48% of the total calculated heat flux). In their experiments on pool boiling of water on plain surface, Gerardi et al. [56] observed that the quenching heat transfer was the dominant mode, and evaporative and convective modes were considerably smaller (< 10%). This is probably because HFE-7100 is much more volatile than water, thus evaporates more readily resulting in a higher amount of heat going into the phase-change process.

The total calculated heat flux from the partition model matches much better with the experimental heat flux for the smoother plain surface (Figure II-18 (a)) than the rougher surface (Figure II-18 (b)). This is likely because the bubble site density on the smoother surface is much smaller than on the rougher surface, resulting in much less interference between bubble sites. Thus the partition model, which neglects the heat transfer effects of the interference, is more accurate for the smooth surface. In the higher temperature range with projected values of the bubble site density, the total calculated heat flux falls short of the experimental values significantly. This is because the site density prediction from the H-I correlation for this surface does not grow as quickly with temperature as the experimental data (Figure II-15). The quenching and evaporative components follow a straight line as a function of temperature beyond 21 °C (smoother surface) and 19 °C (rougher surface), corresponding to the range where the site density and frequency are assumed to be constant.

II.3.3.2 Microporous surfaces:

Figure II-19 shows the heat flux partition calculated from the *N*, *D* and *f* on the three microporous surfaces as a function of the superheat. The solid symbols indicate the partition fluxes calculated using the experimentally obtained bubble parameters. The open symbols denote the partition fluxes calculated using the projected values of *N*, *D* and *f* from the correlations.

In the low temperature range with the experimentally obtained values of the bubble parameters, the evaporative component is found to be the largest, followed by the quenching component. The evaporative component contributes (~65 to 73% of total calculated) significantly more than the quenching component (~ 20 to 25%). The natural convection component is close to zero. Compared to the plain surface, the contribution of the evaporative mode is much higher. This is due to the enhanced nucleation on the microporous surface versus the plain surface. In the high temperature range ($q"_{expt} > 25$ W/cm^2), with the heat flux partitions calculated using the projected values of the bubble parameters, the slope of the total experimental heat flux is found to be about the same as that of the total calculated heat flux from the partition model, with the offset being about 7 to 12 W/cm^2. This is possibly an indication that the bubble site density is indeed constant, just as assumed in the model.

(a) 700 μm

(b) 360 μm

(c) 100 μm

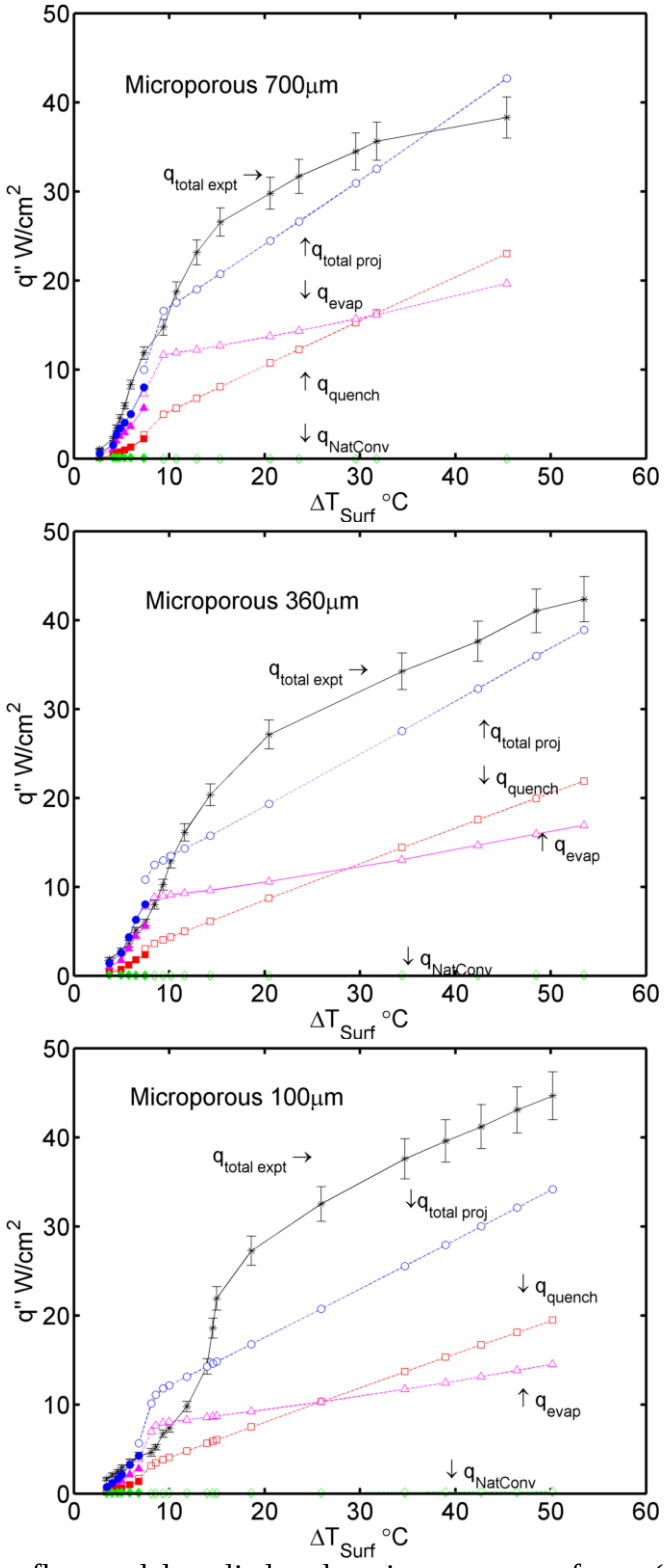

Figure II-19. The partition of heat flux model applied to the microporous surfaces: (a) 700 μm (b) 360 μm and (c) 100 μm. The solid line with * markers is the experimental data. The solid markers denote the data points of *N*, *D* and *f* from experiments, and the open symbols denote the data from extrapolated *N*, *D* and *f*.

In the microporous surface, the nucleation of bubbles takes place in cavities within the layer. The vapor bubble that is formed within the pores then moves through the pores before being released into the pool, detaching from the target surface. From the visualization method, we are able to observe the volume of bubble generated and therefore any heat transfer mode that results in the phase-change is indirectly accounted for. However, the bubble motion through the tunnels of the microporous layer will result in single-phase convective heat transfer to the liquid interface between the vapor and the solid. While the quenching component (q_{quench}) accounts for the single-phase convection during bubble growth outside the layer, the convective single-phase heat transfer within the microporous layer is not accounted for in the partition model. Taking this into consideration, it seems to suggest that a portion of the total heat flux to the pool from the heater with the microporous layer may actually be in the form of sensible heat transfer caused by the bubble motion through the pores, in addition to the enhancement due to the effects of bubble coalescence within and on the surface.

II.4 Summary

We experimentally studied the pool boiling heat transfer performance of copper surfaces coated with thermally conductive microporous copper layer, in comparison with plain surfaces of two different roughness levels. Better heat transfer performances were observed with the microporous surface. Under all conditions tested, the microporous surface showed lower boiling incipience temperature (3 – 11 °C) than the plain surface (17 – 38 °C) due to the presence of cavities in the size range 1 to 5 μm in large numbers on the microporous surface. The heat transfer coefficient increased by 50 – 270% on the microporous surface as a result of the much larger nucleate site density than plain surfaces. The CHF was enhanced by 33 to 60% for the microporous surface over the plain surface. High speed visualization was utilized to obtain

information on the bubble site density, departure diameter and frequency of departure on the different surfaces. On all the surfaces, the bubble site density and frequency of departure increases sharply with temperature, while the diameter at departure stays relatively insensitive to temperature. Correlations available in the literature were used as given, or modified to fit the experimental data for the site density and diameter at departure, and extend them to the full temperature range until CHF. Using the information on the bubble site density, departure diameter and frequency of departure, a simple heat flux partition model that neglects the effects of bubble coalescence, was applied to obtain the contribution of various modes of heat transfer to the fluid from the various target surfaces. On the plain surfaces, both evaporative and quenching components contributes nearly equally to the total heat flux. On the microporous surfaces, the evaporative component contributes about 70% to the total heat, thus confirming that the microporous coating enhances nucleate boiling heat transfer as a direct result of its significantly higher active nucleation site density.

Chapter III Spray Boiling on Microporous Surfaces[1]

III.1 Introduction

Spray cooling is a heat transfer process that occurs when liquid forced through a small orifice shatters into a dispersion of fine droplets which then impact a hot surface. Depending upon the flow rate and heat flux, the droplets spread on the surface and evaporate or form a thin liquid film, removing large amounts of energy at low temperatures due to the latent heat of evaporation in addition to substantial single-phase convection effects [88]. Heat transfer coefficients and CHF much higher than can be attained in pool boiling are possible with sprays since vapor can be removed from the heated surface more easily, allowing liquid to be supplied to the surface more easily. For example, while the CHF on plain surface with water is of the order of 110 W/cm^2 [5], CHF of about 1000 W/cm^2 have been reported using spray cooling [89] illustrating the potential of spray cooling. The liquid droplets are generated by atomizing the liquid through the nozzle by one of two methods: (1) using a high pressure drop across the nozzle that shatters the liquid into fine droplets, or (2) using a secondary high velocity air source. While past studies have shown that air-atomized spray can result in better heat transfer characteristics [90], pressure-atomized sprays are preferable considering that gas-atomized spray are difficult to incorporate in a closed loop electronic cooling system because of the complexity of separating air (or inert gas) from dielectric liquid coolants [91].

[1] A part of this chapter was published in [122]

Regardless of how the spray is produced, the spray cooling process can be categorized into two regimes based on the droplet density (i.e., the number of droplets per unit volume of the spray close to the heat transfer surface). The dilute spray regime involves very low droplet densities with the result that the droplets falling on the surface do not interfere with one another. Due to their momentum, the droplets form thin discs of liquid on impacting the surface; these discs then evaporate by absorbing heat from the surface. The other spray regime involves dense spray, that is, the number of droplets impinging on the heated surface is so large that there is extensive interaction between individual droplets upon reaching the surface. If the number of droplets is large, the droplets impinging close to each other will affect each other such that the liquid from these droplets will merge to form a thin film of liquid on the surface. If the rate of evaporation of this liquid film is lesser than the rate of incoming liquid, the subsequent droplets will impinge on a thin liquid film instead of the heat transfer surface. Thus, the impinging droplets will maintain a liquid film on the surface, the thickness of this film depending on the influx of liquid, the rate of evaporation, and the surface conditions. Figure III-1 illustrates the formation of a thin liquid film on the surface due to the spray impingement. The low liquid flow rates involved in the dilute regime limit its heat removal capacity and thereby its applications [92]. Hence, the current study concerns only the dense spray regime of pressure-atomized spray cooling system. Recent reviews of the spray cooling phenomenon are provided in references [93–95].

Spray heat transfer in the boiling regime on the plain surface has been studied for several years. Most of the early research on spray cooling was focused on the film boiling regime associated with the quenching of metals (see for example [96], and references therein). Due to the focus on the film boiling regime, the results from these studies are of limited value to design

of electronic cooling processes which are typically in the nucleate boiling regime. Comparison of spray cooling with other phase-change cooling techniques such as pool boiling and microchannel cooling and jet impingement shows that significantly higher quantities of heat can be removed with lower superheat by spray cooling [91,97]. Furthermore, spray cooling does not suffer from flow instability that is a major concern with microchannel cooling. A uniform dispersal of the liquid droplets impinging on the heater surface gives rise to a more uniform spatial surface temperature distribution over the entire spray impact area. Moreover, boiling incipient superheat, which may cause a severe thermal shock to electronic components and make the heat transfer performance highly unpredictable, is much less pronounced in spray cooling systems than in pool or flow boiling systems.

(a)

(b)

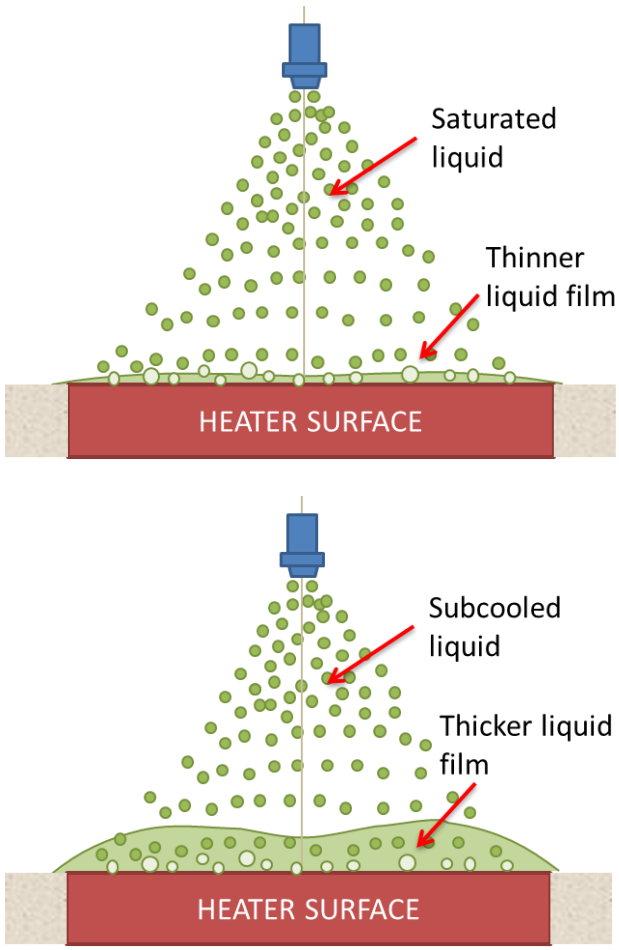

Figure III-1. Schematic showing the interaction of the spray droplets with (a) thin liquid-vapor film formed on the heater surface, (b) thick liquid film formed on the surface at high flow rates and/or high subcooling levels.

III.1.1 Spray Features

Atomization by the spray nozzle creates a distribution of droplet sizes, which can be measured with laser diffraction or phase Doppler anemometry (PDA). However, for practical purposes it is more convenient to use an average droplet size to characterize the spray. A general expression for mean diameter is given by:

$$d_{pq} = \left(\frac{\sum_{i=1}^{N} d_i^p}{\sum_{i=1}^{N} d_i^q} \right)^{1/(p-q)}, \quad \text{(III-1)}$$

where N is the total number of droplets generated by the spray nozzle and d_i is the diameter of the i^{th} droplet, and p and q are orders (e.g. 1, 2, or 3). The values of p and q would depends on the general physics of a given problem [98]. In spray cooling, the "Sauter mean diameter (SMD)" is commonly used because it captures both the volume and surface area characteristics of the spray. The SMD is defined as:

$$d_{32} = \frac{\sum_{i=1}^{N} d_i^3}{\sum_{i=1}^{N} d_i^2}. \quad \text{(III-2)}$$

Using experimental data of droplet size distribution in a full-cone spray obtained by phase Doppler particle analyzer (PDPA), Estes and Mudawar (1995) developed an SMD correlation for FC-72, FC-87, and water:

$$\frac{d_{32}}{d_0} = 3.67\left(We_{d0}^{1/2} Re_{d0}\right)^{-0.259}, \quad \text{(III-3)}$$

where the Weber and Reynolds numbers are defined as:

$$We_{d0} = \frac{\rho_v \left(\frac{2\Delta P}{\rho_l}\right) d_0}{\sigma_l}, \quad \text{(III-4)}$$

$$Re_{d0} = \frac{\rho_l \left(\frac{2\Delta P}{\rho_l}\right)^{1/2} d_0}{\mu_l}, \tag{III-5}$$

where d_0 is the nozzle orifice diameter, ρ_v is the vapor density, ρ_l is the liquid density, ΔP is the nozzle pressure drop, σ_l is the liquid surface tension, and μ_l is the liquid viscosity. The fluid properties are evaluated at the average of the inlet temperature and the saturation temperature.

Another key feature of droplets is velocity. Ghodbane and Holman [99] used a simple energy balance method to determine the break-up velocity:

$$U_{breakup} = \left(U_{pipe}^2 + \frac{2\Delta P}{\rho_l} - \frac{12\sigma_l}{\rho_l d_p}\right)^{1/2}, \tag{III-6}$$

where d_p is an average value for the diameter of the droplets as calculated using a correlation they developed. The third term within the parenthesis in the equation is found to be <2% in our experiments, and is therefore neglected.

III.1.2 Parameters Affecting Spray Cooling

As summarized by Coursey [100], there are many important parameters that control spray cooling heat transfer (Table III-1). One of the greatest challenges in the study of spray cooling is the inability to independently and precisely control these parameters. For example, mass flux can be increased by increasing the differential pressure in a pressure atomizing spray. However, this increase in pressure strongly affects droplet breakup; completely altering droplet size, number, and velocity. Of these parameters, spray properties have received the most attention. Chen et al. [89] studied the relative importance of mean droplet size, droplet flux, and droplet velocity on CHF. They used more than 20 full cone nozzles at a variety of nozzle pressures and standoff distances to systematically vary one of the above parameters while holding the other two

constant. Over 3000 combinations of the three spray parameters were generated, although only a small subset of these satisfied the criteria of two parameters being constant. They found that the mean droplet velocity had the greatest effect on CHF, followed by the droplet number flux. Both the CHF and heat transfer coefficient increased as these parameters were increased. The Sauter mean diameter was found to be of little importance.

Table III-1. Parameters affecting spray cooling.

Spray properties	Droplet size & distribution
	Droplet number flux
	Droplet velocity & distribution
	Mass flux & distribution
	Spray angle
Fluid properties	Density of the liquid
	Density of the vapor
	Thermal conductivity of liquid
	Surface tension of liquid
	Specific heat of liquid
	Latent heat of vaporization
Surface properties	Superheat
	Thermal conductivity of the heater substrate
	Surface structure
Environmental properties	Subcooling, Pressure
	Foreign nuclei, non-condensable gases
	Gravity and orientation

The effect of mass flow rate appears to be completely dependent on the total amount of liquid supplied. Thermodynamically, heat transfer is limited to:

$$q_{\max} = \dot{m}\left(C_{\mathrm{p}}\Delta T + h_{\mathrm{lv}}\right), \qquad \text{(III-7)}$$

where $\dot{m}$ is the mass flow rate, C_p is the liquid specific heat, h_{lv} is the latent heat of vaporization, and ΔT is the surface superheat temperature.

In a sufficiently dilute spray, most of the mass supplied can be heated and vaporized. In these cases, heat transfer increases as the mass flow rate increases. With a dense spray, much of the liquid flows off the surface and heat transfer may be insensitive to increases in the mass flow rate [90]. In experiments with air-atomized water sprays, Yang et al. [101] found that in the nucleate boiling regime the heat transfer increased with increasing flow rate until a limit of 3 L/hr, when the improvement ceased. Tilton et al. [102] found that heat transfer increased as the coolant flow rate was increased, provided the module was not flooded. Several other studies have found that heat transfer increased as mass flow increases [103–106]. Subcooling also has been found to increase CHF because more sensible heat is required to heat the liquid to the saturation temperature [105,107,108].

III.1.3 Models of Spray Cooling

Single-phase convection:

The simplest model of spray cooling is that of single-phase convection. Similar to pool boiling, spray cooling heat transfer is linear with respect to wall-to-spray temperature difference when the superheat is modest. This indicates little two-phase effects. Heat transfer is enhanced by maximizing the sensible heating of the spray and preventing vaporization, which leads to CHF [104]. The simplest two-phase model of spray cooling heat transfer is that the spray creates a thin-film on the surface of the heater. Heat is then conducted through the film and evaporation occurs at the free surface. The impinging droplets are thought to increase the conductance of this

layer through improved mixing [90]. To maximize heat transfer, the liquid film must be made as thin as possible. Pautsch and Shedd [109] used a four nozzle array and found that the regions with the poorest thermal performance had the thickest films.

Nucleate boiling spray:

The thicker films mentioned above leads to the second basic model, which is nucleation-dominated flow boiling. If the spray creates a thick enough liquid film, then the performance may be similar to that of typical boiling systems. In these systems, the heat transfer may be dominated by the nucleation site density on the solid surface. However, there is evidence to suggest that the impinging drops make the nucleation process very different. In the secondary nucleation model, the large nucleate and convective heat transfers observed are attributed to so called "secondary nuclei" [101,110]. When droplets enter the liquid film they are thought to entrain vapor, which serves as an additional nucleation site. Also, if a droplet breaks up a growing bubble, the nucleation site density is further increased. Rini et al. [110] found that the heat transfer increases as the droplet number flux increases, which they attribute to a corresponding increase in the number of secondary nuclei. Furthermore, the ratio of nucleate to convective heat transfer was unaffected by the droplet number flux, which suggests that secondary nuclei and turbulent mixing of the droplets enhances nucleate boiling and convection similarly.

Horacek et al. [108,111] proposed another mechanism for two-phase spray cooling heat transfer: contact line heat transfer. They used the total internal reflectance (TIR) technique to determine the wet and dry portions of the heated surface. They then calculated the wetted area fraction and the contact line length. The heat flux (once corrected for sensible heat) was found to be well correlated with the contact line length, which also increased to a local maximum like

CHF. Interestingly, wetted area fraction was found to decrease monotonically as superheat increased and could not be correlated with heat flux. This suggests that contact line heat transfer and not wetted area is responsible for two-phase portion of the heat transfer. Critical heat flux mechanisms in spray cooling may be slightly different than in typical boiling systems. It is generally agreed that CHF begins with dryout around the perimeter of the heater [90,112]. However, Pautsch and Shedd [109] noticed that CHF occurred first at the center of their heater due to it having the largest local film thickness. No validated model of CHF for spray cooling exists, but there are some possible mechanisms. With a sufficiently sparse spray, CHF will occur when the liquid supply is exhausted due to evaporation. Droplets hitting dry surface will quickly evaporate. Those droplets forming pools will boil like a typical pool. If liquid is in sufficient supply, then CHF may be caused by a "choking" of the liquid supply by bubbles generated in the liquid film. This could be due to escaping vapor preventing drops from hitting the surface or the ejection of liquid from the surface caused by the bursting of bubbles. With all of these models in mind it is important to note that the applicability of the model may vary significantly with mass flux. Dilute sprays may appropriately be considered mere extensions of discrete droplets. In these cases, evaporative effects may dominate. The opposite extreme, with large mass flow, may create such a thick liquid film that the process more closely resembles single-phase impinging jet flow.

III.1.4 Spray Cooling CHF Correlation

A CHF correlation was proposed by Mudawar and Estes [112], based on the one proposed earlier by Ghodbane and Holman [99]. They varied the nozzle-to-surface distance and found that CHF was maximized when the spray impact cone just inscribed the heater surface. With too short a nozzle spacing, droplet impingement was limited to a small portion of the heater

and CHF was lower. Conversely, when the spacing was too large, much of the liquid was wasted due to overspray. Based on these observations, they developed a correlation based on the average volumetric flux over the spray impact area:

$$\frac{q''_{CHF}}{\rho_v h_{lv} Q''} = 2.3\left(\frac{\rho_l}{\rho_v}\right)^{0.3}\left(\frac{\rho_l Q''^2 d_{32}}{\sigma}\right)^{-0.35}\left(1 + 0.0019\frac{\rho_l C_P \Delta T_{sub}}{\rho_v h_{lv}}\right), \qquad \text{(III-8)}$$

where d_{32} is the Sauter mean diameter evaluated as discussed previously , ρ_v is the vapor density, ρ_l is the liquid density, Q" is the flow rate per unit area of the heater surface ("volumetric flux"), σ is the liquid surface tension, and C_p is the liquid specific heat. The fluid properties are evaluated at the saturation temperature. This correlation has been reported to predict reasonably well the CHF observed under many conditions using dielectric fluids and water.

III.1.5 Effect of Surface Structure on the Heat Transfer and CHF

Surface structure is an important parameter affecting spray cooling and is the focus of the present work. Pais et al. [33] argued that increasing the surface roughness decreases the heat transfer by increasing the thickness of the liquid film on the surface. Heat transfer on microstructured surfaces was studied by Sodtke and Stephan [113] using water and a full-cone spray atomizer. Three pyramidal microstructures of various heights and widths, as shown in (a) were manufactured onto a 20 mm diameter copper cylinder such that the microstructured surface increased the wetted area by a factor of $\sqrt{2}$. Although little increase in heat transfer was observed for both microstructured surfaces at a standoff distance of 25 mm, very large increases were observed when the standoff distance was increased. Significantly larges enhancement in the heat transfer was observed, which was much larger than the surface area enhancement. This effect is hypothesized to be due to an increased length of the three phase contact line that forms on the structures which leads to a very efficient thin film evaporation.

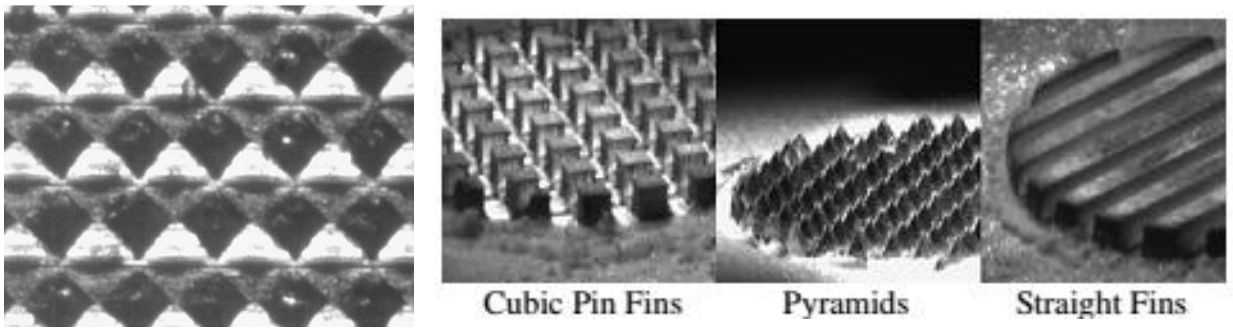

(a) (b)

Figure III-2. Photos of microstructured surfaces studied by (a) Sodtke and Stephan [113], and (b) Silk et al. [34].

Silk et al.[34] investigated the effects of enhanced surface structures beyond the surface roughness range on spray cooling heat transfer. The surface enhancements consisted of cubic pin fins, pyramids, and straight fins machined on the top surface of heated copper blocks with 2.0 cm^2 cross-sectional areas, as shown. Measurements were compared to a plain surface. PF-5060 under nominally degassed conditions was used as the working fluid. Spray volumetric flux (1.6 $cm^3/cm^2/s$) and nozzle to heater distance (17 mm) were held constant throughout each test. The study showed that the straight fins had the largest heat flux enhancement relative to the plain surface, followed by the cubic pin fins and the pyramid surface. Each surface had an increase in evaporation efficiency at CHF compared to the flat surface. The authors determined that the straight finned surface had the most efficient use of area added for additional heat transfer relative to the flat surface. They also determined that heat flux enhancement observed with the use of enhanced surfaces is a function of surface area added and liquid management on the heater surface.

Bostanci et al. [37] performed spray cooling experiments with ammonia on microstructured surfaces with indentations and protrusions at heat fluxes of up to 500 W/cm^2. They observed an enhancement of 49% -112% in the heat transfer coefficient with respect to that

on a smooth surface. The increase is believed to be due to the increased surface area, availability of a range of the cavity sizes, and increased contact line length density over the heater surface. Kim et al. [6] investigated evaporative spray cooling on microporous coated surface using water at very low flow rates up to 0.025 $cm^3/cm^2/s$. The low thermal conductivity porous layer was fabricated with thermally conductive microparticles using an organic binder, with a maximum thickness of 500 μm. They found that the critical heat flux (CHF) increased by 50% relative to that on the plain surface. Their mass fluxes, however, were very small, so the conduction resistance of the coating was probably not significant. The maximum heat flux achieved was 3.2 W/cm^2. Thiagarajan et al. [106] reported spray impingement boiling experiments on the copper surfaces coated with a thermally conductive copper microporous coating using HFE-7100 as the coolant. The microporous surface showed a 100-300% increase in the heat transfer coefficient over the plain surface, at all subcooling levels of 0°C to 30°C and flow rate levels 4.7 cm^3/s to 15.8 cm^3/s.

The effect of structured surfaces on pool boiling has received intensive attention. A summary of the different surface enhancements and their effect on the pool boiling performance is provided in reference [114] in which several forms of microstructure enhancement including laser drilled cavities, reentrant cavities, micro-fins, porous coatings and sputtered surfaces are reviewed. In particular, porous surfaces made with microparticle coatings have been studied in the past as a means of enhancing heat transfer in pool boiling [21,115,116]. Such porous surfaces lead to enhanced boiling heat transfer by a combination of the following factors: an increase in the effective surface area that leads to enhanced interaction of the liquid with the surface, an increase in the nucleation site density, that presence of capillaries that facilitate liquid return, and an increase in the three phase contact line length throughout the pores. By proper design of the

porous layer, the CHF could be enhanced by the capillary-assisted liquid flow towards the heater surface. This reduces liquid vapor counter flow resistance and impedes the development of localized dry-out conditions, which leads to a higher CHF [117].

The use of enhanced surfaces in conjunction with dense spray cooling (that is, when the flow rate is significantly higher than what evaporates from the surface) with dielectric liquids has received much less attention as compared to their application to pool boiling. 3M Novec HFE-7100 has been identified as a potential coolant for the cooling of power electronic modules in automobiles due to the desirable properties [2]. However, there exists no study in the literature on the performance of HFE-7100 coolant spray impingement, in conjunction with enhanced surfaces. The main objective of the present study is to investigate the performance enhancement that can be obtained by the conductive copper microporous coating, under spray impingement configurations with the HFE-7100 coolant. The effect of the spray flow rate using two different spray nozzles, and liquid subcooling on the heat transfer phenomena are also studied. In the following sections, the experimental setup and procedure, and the target surface enhancements are described, followed by a discussion of the results.

III.2 Experimental Apparatus and Procedure

III.2.1 Setup

The schematic diagram of the experimental test loop which is designed to deliver the test liquid at the desired pressure, temperature and flow rate to the spray nozzle located inside the test chamber is shown in Figure III-4 and Figure III-4. The bottom portion of the chamber serves as the liquid reservoir. The HFE-7100 liquid is circulated in a closed loop starting from the reservoir until it reaches the spray nozzle, using a magnetically-coupled precision pulseless flow gear pump made by Micropump (model number: C-73005-06). The pump is driven by a motor made by Leeson (model number: C-70073-00).

After the liquid leaves the spray nozzle, the coolant hits the heater surface and is partially evaporated upon impact. The scattered liquid accumulates in the bottom of the test vessel, while the vapor rises to the top region of the vessel by buoyancy. The liquid from the test vessel drains to the pump, and then passes through a valve and subsequently through a plate-type heat exchanger, where the liquid is subcooled to the required temperature. The subcooled liquid then passes through the flow meter, and then through a filter before again reaching the spray nozzle. The temperature of the incoming liquid is read by a type-K thermocouple approximately 2.5 cm upstream of the nozzle exit. The pressure measurements, prior to the nozzle entrance and inside the chamber, are made using pressure transducers. The pure liquid-vapor mixture in the chamber is maintained at 60.4°C which is the saturation temperature corresponding to the sea-level atmospheric pressure of HFE-7100.

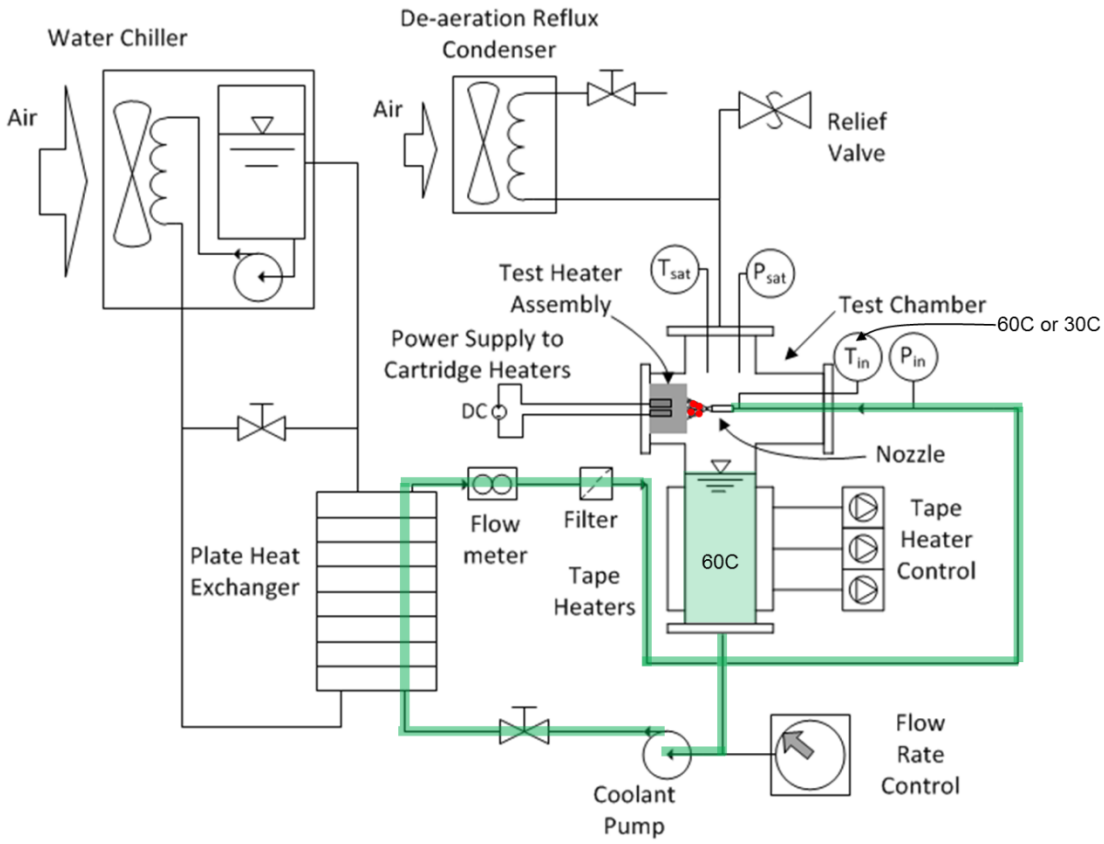

Figure III-3. Schematics of the spray cooling experimental test loop. The green lines indicate the coolant liquid flow path.

An air-cooled finned-tube heat exchanger is placed above the test vessel for the removal of non-condensable gases from the liquid. The temperature of the liquid in the test vessel temperature is maintained at a fixed point, within ±0.5°C, using band heaters that heat the liquid through the wall of the vessel. The input from the different sensors feed in to a data acquisition system and are read using LabVIEW. All the controls are manually operated.

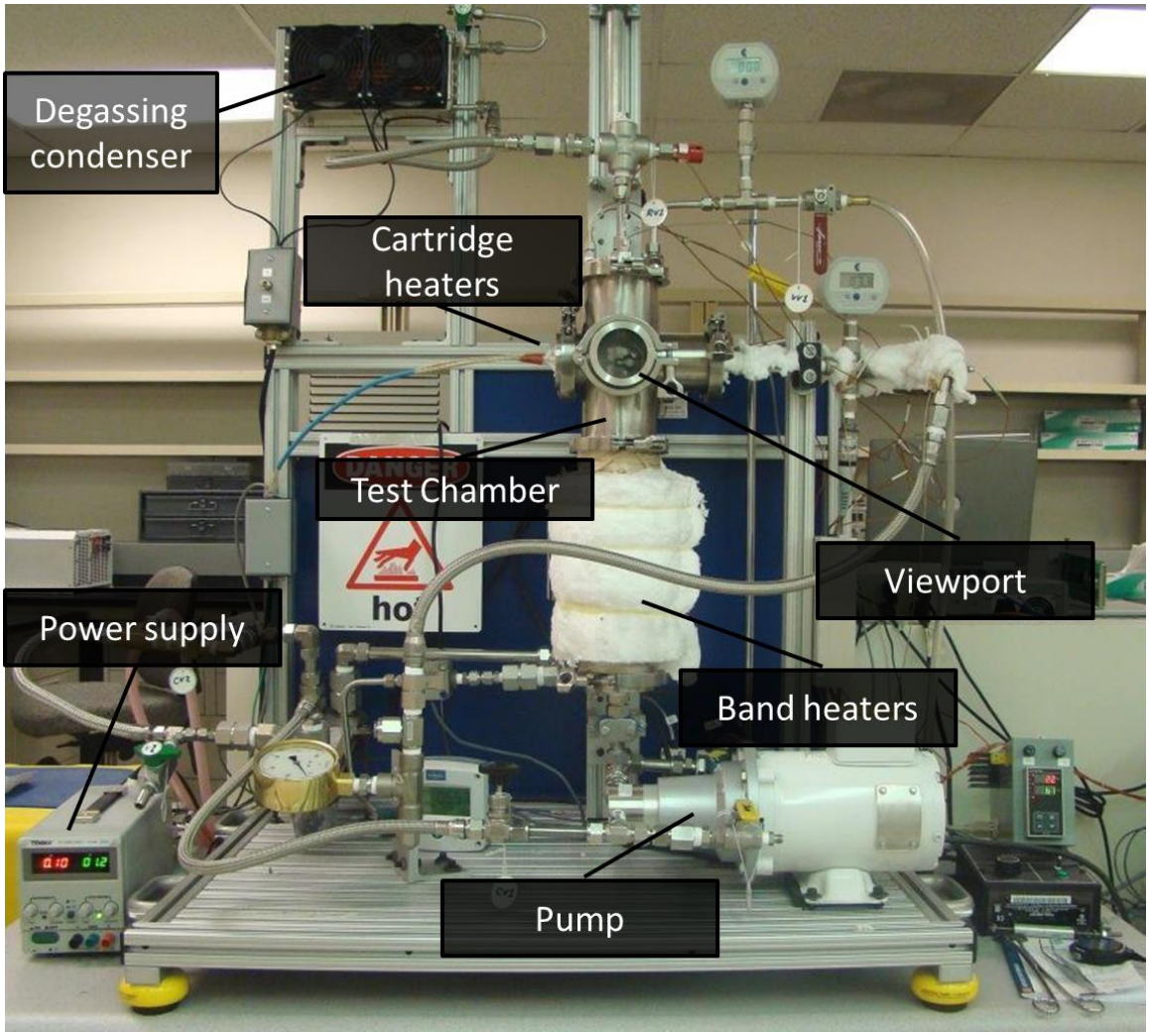

Figure III-4. Photograph of the spray cooling experimental test loop.

Figure III-5 shows the construction of the test heater. The test heater is a single cylindrical block of oxygen-free copper with a cubical projection whose top face has a surface area of 1 cm x 1 cm and is exposed to the coolant. The projected part of the cylindrical block is surrounded by an insulating fiberglass (G7) block which fits tightly along the sides of the cube. Three cartridge heaters, together capable of delivering over 250 W, are placed in cylindrical holes which are bored in the back of the copper block. The entire heater assembly is mounted on a stainless steel flange which is then clamped to the chamber.

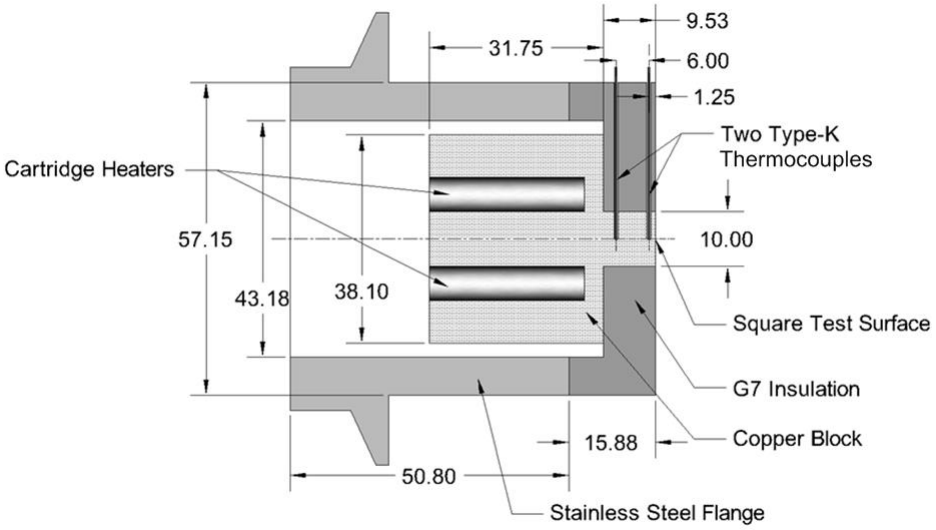

(a)

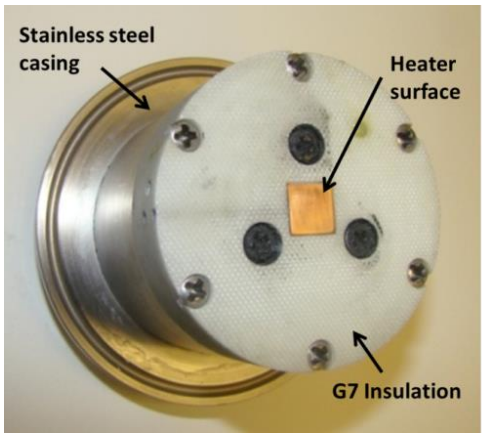

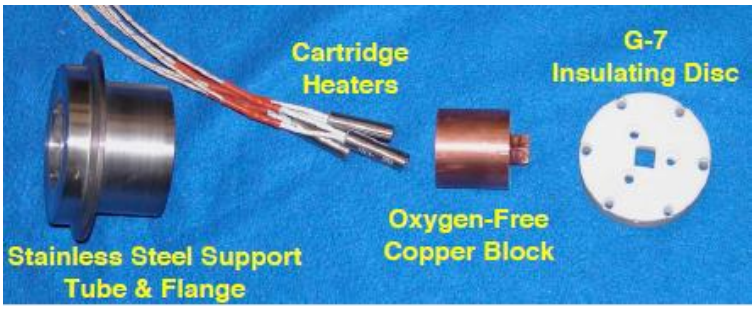

(b) (c)

Figure III-5. (a) Cross-section view of the test heater assembly (all dimensions in mm), showing the cartridge heaters that supply power to the copper block, the insulation around the block and the location of the thermocouples. (b) Photo of the assembly showing where the square target surface is exposed to the coolant. The surface is either plain, or coated with the microporous layer of conductive copper. (c) Individual parts of the heater assembly.

Two type-K thermocouples are inserted into the copper block, at a distance of 1.25 mm and 7.25 mm from the test surface. Dow Corning TC-5022 thermal grease is used to provide good thermal contact between the thermocouples/heaters and the copper block. The heat flux through the surface (=q'') is determined by the temperature gradient across these two

thermocouples. This information is also used to determine the surface temperature (assuming one dimensional heat flow), and hence the surface heat transfer coefficient.

Two pressure-swirl, full cone nozzles manufactured by Spray Systems, Inc. were used for this study: Unijet TG-0.7 (denoted as nozzle N1), and Unijet TG-3.5 (denoted as nozzle N2). Both of these nozzles are made of type # 303 stainless steel. The spray nozzles are situated so that the nozzle exit is at a distance of 9.4 mm (N1 nozzle) or 14.3 mm (N2 nozzle) from the target surface, as illustrated in Figure III-6. With this placement, the spray circle just inscribes the square edge of the heater to maximize the CHF [118]. The characteristics of the spray nozzles are summarized in Table III-2, and the thermophysical properties of HFE-7100 at various temperatures are shown in Table I-1.

Table III-2. Characteristics of the spray nozzles used in this study.

Nozzle	Orifice diameter d_0, mm	Distance from surface, mm	Spray cone angle θ	Volumetric flow rate Q, cm^3/s	Sauter mean diameter d_{32}, μm
N1 (TG 0.7)	0.762	9.4	56°	1.1 to 4.7	265 to 102
N2 (TG 3.5)	1.7	14.3	38.5°	4.7 to 15.8	460 to 191

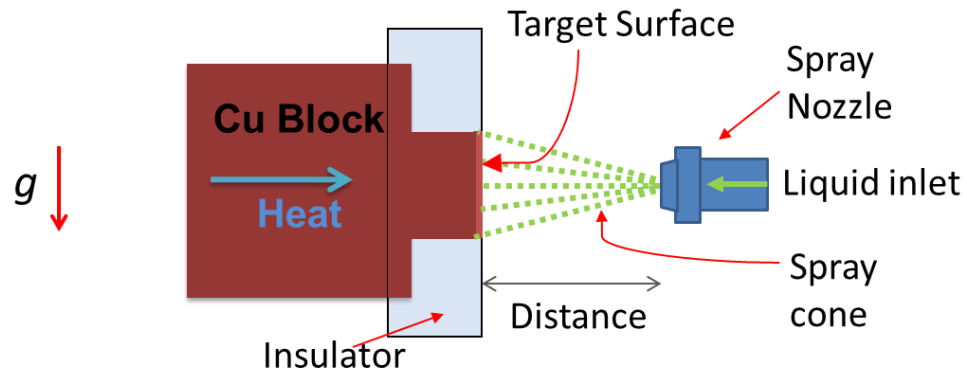

(a)

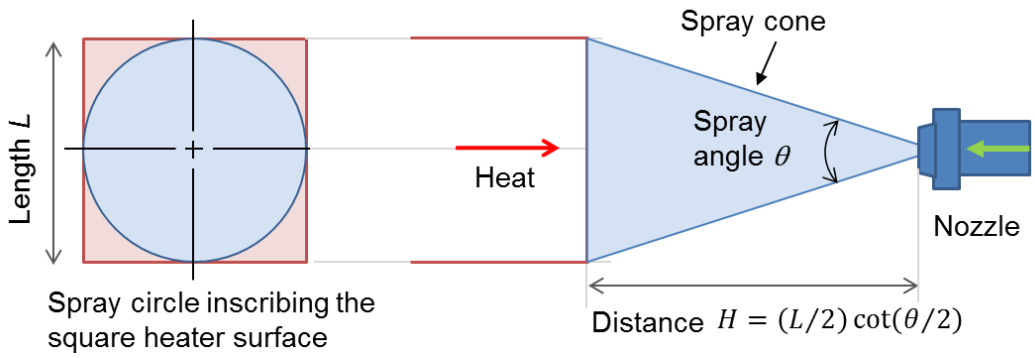

(b)

Figure III-6. Schematic diagrams showing the position of the spray nozzle relative to the heater assembly.

III.2.2 Experimental Procedure

Before each experiment, the fluid was deaerated for 20–45 minutes to expel any dissolved non-condensable gases using the deaeration condenser. This was accomplished by boiling the liquid in the reservoir using the band heaters around the chamber, and allowing the vapor mixed with the non-condensable gases to flow through a condenser located above the setup. The portion of the vapor that was condensed was allowed to drip back into the chamber, and the non-condensable gases were allowed to escape the chamber. The pump was switched on, and the liquid circulated through the loop during the degassing process to remove all the non-

condensable gases in the loop. After this procedure, the system was allowed to settle to a steady state, with no input power to the copper target surface. The partial pressure of non-condensable gas in the chamber $P_{gas} = P_{total} - P_{sat}(\text{at } T_{sat})$, was calculated to be 4,400 Pa. Using the constant of $C_H(T)$ = 3.2×10^7 Pa-mol/mol for HFE-7100 in Henry's law $P_{gas} = C_H(T)C_{gas}$, the dissolved gas concentration in the liquid was found to be about 140 ppm. This represents about 6% of the dissolution level in a non-degassed liquid.

For the spray experiments, two levels of liquid temperatures (measured upstream of the nozzle outlet) were considered: 30 °C (subcooling ΔT_{sub} = 30 °C, subsequently referred to as "subcooled"), and 60 °C (subcooling ΔT_{sub} = ~0 °C, subsequently referred to as "near-saturated"). For the spray tests with nozzle N1 at a flow rate of 1.1 cm^3/s, a subcooling level of only 26 °C could be attained because of cooling limitations. Boiling curves were generated by raising the voltage and thus the heat flux through the cartridge heaters in small increments. This allowed the temperatures to achieve steady state, which was determined by less than 0.1 °C change in 3–10 minutes (depending on the surface). The flux increment near the CHF was kept small (1 to 2 W) to achieve an accurate determination of the CHF (±2 W/cm^2). The highest heat flux with a stable target surface temperature was considered to be the CHF, beyond which a large surge in the temperature occurred with only a small increment in the heater power. Once the CHF was detected, the heater voltage was cut off and the target was allowed to cool down.

III.2.3 Experimental Uncertainties

The flow meter was calibrated by measuring the total liquid flowing through the loop in a given amount of time. The uncertainty in the flow rate is estimated to be ±0.17 cm^3/s for a flow rate range of 1 to 17 cm^3/s. The pressure transducers were calibrated to an accuracy of ±350 Pa

using a Fluke pressure calibrator. A NIST-traceable Resistance Temperature Detector (RTD) was used along with a Hart Scientific thermal bath to calibrate all the thermocouples in the temperature range from 20 °C to 105 °C. The uncertainty in the temperature measured is within ±0.03 °C. The uncertainties in voltage and current are negligible (<0.12% and <0.05%, respectively). The uncertainty in the heat flux measurement was estimated using the Kline and McClintock method [60]. Because of the uncertainty in the positions of the two target thermocouples (estimated to be ±0.125 mm from the centerline of the holes), the measured heat flux is estimated to have an uncertainty of ±6% (with 95% confidence intervals). The heat loss is in the range from 6% to 15% for a variety of heat transfer coefficients (h) and input power levels (q_{in}) in the nucleate boiling regime. The highest losses occur with the lowest h and the lowest q_{in}.

To ensure that the temperature readings by the thermocouples were accurate—so that the heat flux could be reliably measured by using the temperature gradient—a steady-state thermal analysis was performed with a 3D ANSYS Workbench model. . The analysis was performed at different surface heat fluxes, assuming a uniform heat transfer coefficient at the target surface and a set of heat transfer coefficients for the different modes of heat loss, including natural convection to the air surrounding the cylindrical copper block, and forced convection to the liquid/vapor from the G7 fiberglass surrounding the projected part of the copper block. The schematic of the model with the boundary conditions is shown in Figure III-7 (a) for a sample simulation corresponding to an experiment with an input heat of 99.75 W and a heat transfer coefficient of h = 2.06 W/cm^2/K on the target surface.

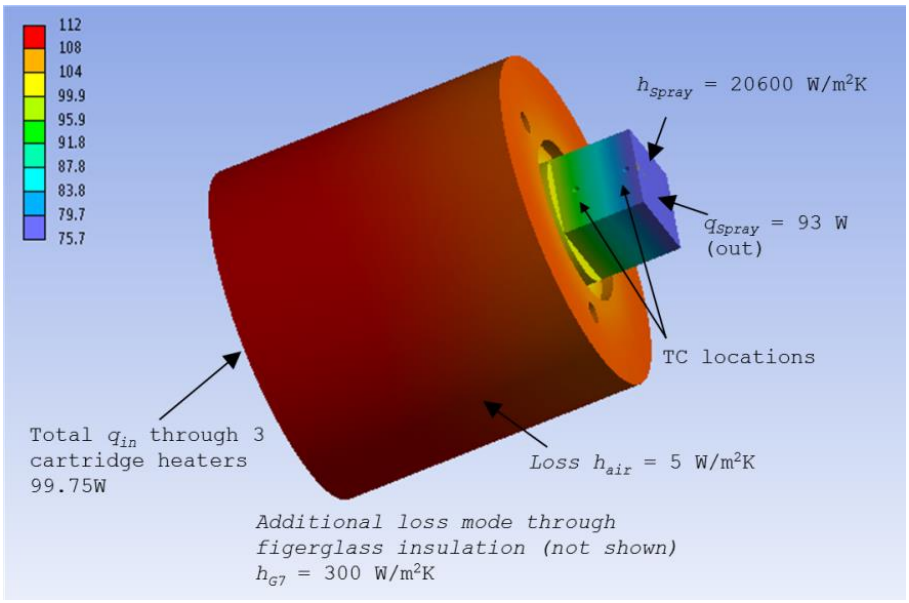

(a)

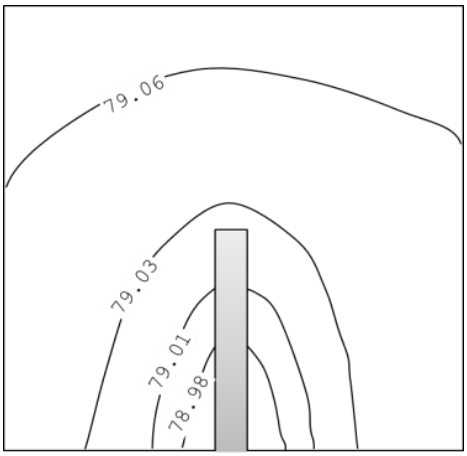

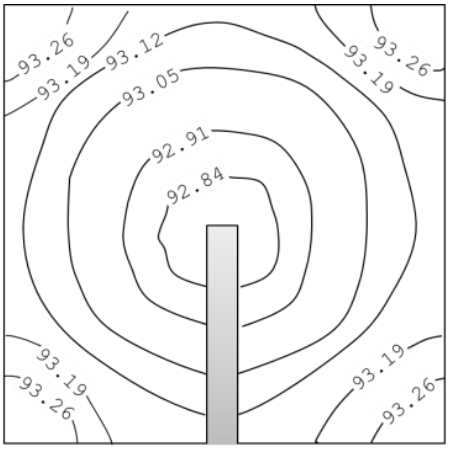

(b) (c)

Figure III-7. (a) Boundary conditions applied to the ANSYS model, and the resultant temperature (°C) distribution on the copper block and heat transfer to the spray. Temperature contour plots in the plane of each target thermocouple: (b) closer to the surface; (c) farther from the surface for a sample simulation corresponding to an experiment with heat input of 99.75 W and a heat transfer coefficient of 2.06 W/cm^2-K.

The set of coefficients for heat loss used in the analysis was obtained by iteratively trying different values until the temperatures obtained in the ANSYS model (and heat flux from the surface) matched the corresponding experimental values. In the model, the input values were the power input ($q_{in} = VI$, where V is the voltage and I is the current through the cartridge heaters)

and the loss heat transfer coefficients. The heat transfer through the different surfaces (including the target surface) and the temperature at different points within the copper block were the outputs. Figure III-7 (b) and (c) show the temperature contours in the planes where the thermocouples are placed in the copper block. . The temperature is uniform within 0.15 °C in the plane closer to the target surface, and within 0.5 °C in the plane farther from the surface. This confirms that the surface temperature in the experiments could be taken as the extrapolation of the two thermocouple temperature measurements.

III.2.4 Sample Surfaces

Two types of surfaces were studied: the baseline case of plain copper surface with no coating, and a microporous copper coating. The plain copper surface was polished to a surface roughness, R_a, of 0.33 μm (measured with a Fowler Pocket Surf roughness profilometer). The surface was deoxidized before a series of tests by wiping with cotton swabs dipped in hydrochloric acid and cleaning with isopropyl alcohol. The scanning electron microscope (SEM) image of the plain surface is shown in Figure III-8(a). The target with the microporous copper coating was obtained from 3M Corporation. The procedure for making the coating was explained in Chapter I. The resulting coating was about 100 μm thick with a porosity of about 57%. As shown in the SEM image of the microporous coating in Figure III-8(b), the microporous copper layer includes cavities of a variety of sizes, which result in a high nucleation site density. In addition, the layer includes a network of interconnected channels that facilitate liquid replenishment that could potentially delay dry-out on the surface to higher heat flux values as compared to the plain surface.

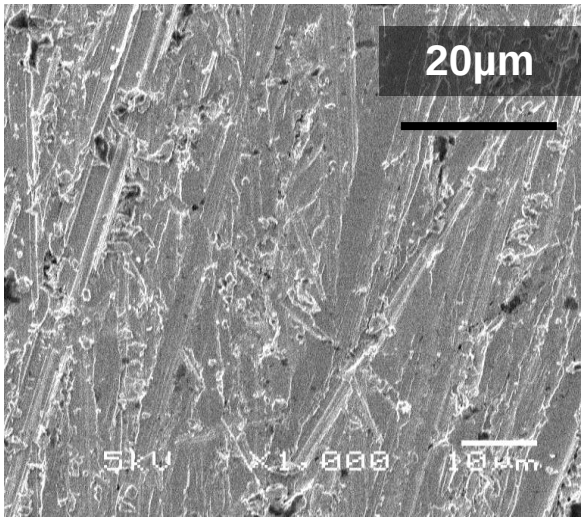

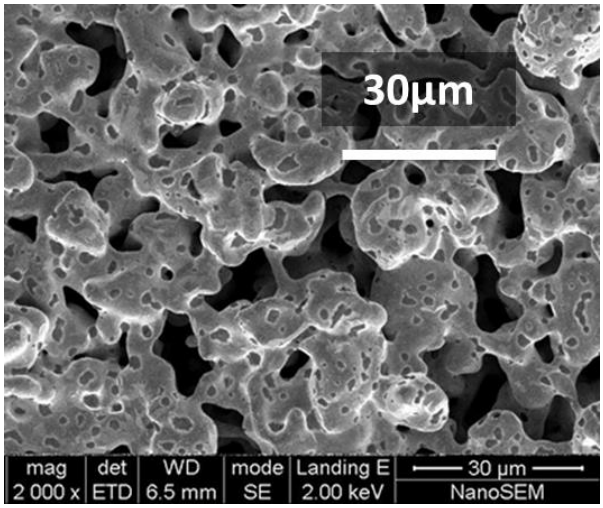

(a) (b)

Figure III-8. SEM micrograph of (a) the plain surface, and (b) the microporous coating.

III.3 Results and Discussions

III.3.1 Spray Characteristics

Experiments with spray impingement were performed, spanning the flow rates 1.1 cm^3/s to 4.7 cm^3/s with nozzle N1, and 4.7 cm^3/s to 15.8 cm^3/s with nozzle N2. The flow rate range was chosen considering the pumping pressure drop limitations. The Sauter mean diameter (SMD) is the diameter of a spherical drop that has the same volume to surface area ratio as the entire spray (see equation (III-2)). It is commonly used in spray cooling because it captures both the volume and surface area characteristics of the spray. For a fully-developed spray, the droplet Sauter mean diameter, d_{32}, is estimated using the correlation from [112], shown in equation (III-9)

$$\frac{d_{32}}{d_0} = 3.07\left(\frac{\sigma^{1/2}\mu_l}{\rho_v^{1/2}\Delta P d_0^{3/2}}\right)^{0.259}, \qquad \text{(III-9)}$$

where d_0 is the nozzle orifice diameter, ΔP is the pressure drop across the nozzle, σ is the surface tension and μ_l is the viscosity of the liquid, and ρ_v is the density of the vapor. This equation is a simplified form of equation (III-3). The properties of the liquid evaluated at the nozzle inlet temperature are used for the purpose of calculating the d_{32}. An estimated value of the number of droplets, N, that are generated per unit time (number density) is obtained using [89] the relation

$$Q \approx N\pi d_{32}^3/6, \tag{III-10}$$

where Q is the flow rate. The mean droplet velocity is estimated using equation

$$U \approx \left[U_{pipe}^2 + \frac{2\Delta P}{\rho_l}\right]^{1/2}, \tag{III-11}$$

where U_{pipe} is the liquid velocity in the pipe before entering the nozzle and ρ_l is the density of the liquid. The d_{32}, U and N of the droplets thus estimated, are shown in Figure III-9. For both the nozzles, at the same flow rate, the estimated value of the d_{32} for the case of the near-saturated spray is lower than that of the subcooled spray, which means that the near-saturated spray comprises larger number of smaller droplets than the subcooled spray. This is primarily due to the fact that the surface tension of the near-saturated liquid is lower than that of the subcooled liquid. The upper limit of the flow rate for the N1 nozzle is chosen to be the same as the lower limit for N2 nozzle so as to make a direct comparison between the heat transfer performances obtained at the same flow rate, flowing through the two different nozzles resulting in vastly different spray characteristics. The d_{32} of the spray from nozzle N2 at the flow rate of 4.7 cm^3/s is about 3.5 times larger than that of nozzle N1; therefore, the number density in N2 is 40-50 times smaller than that in N2.

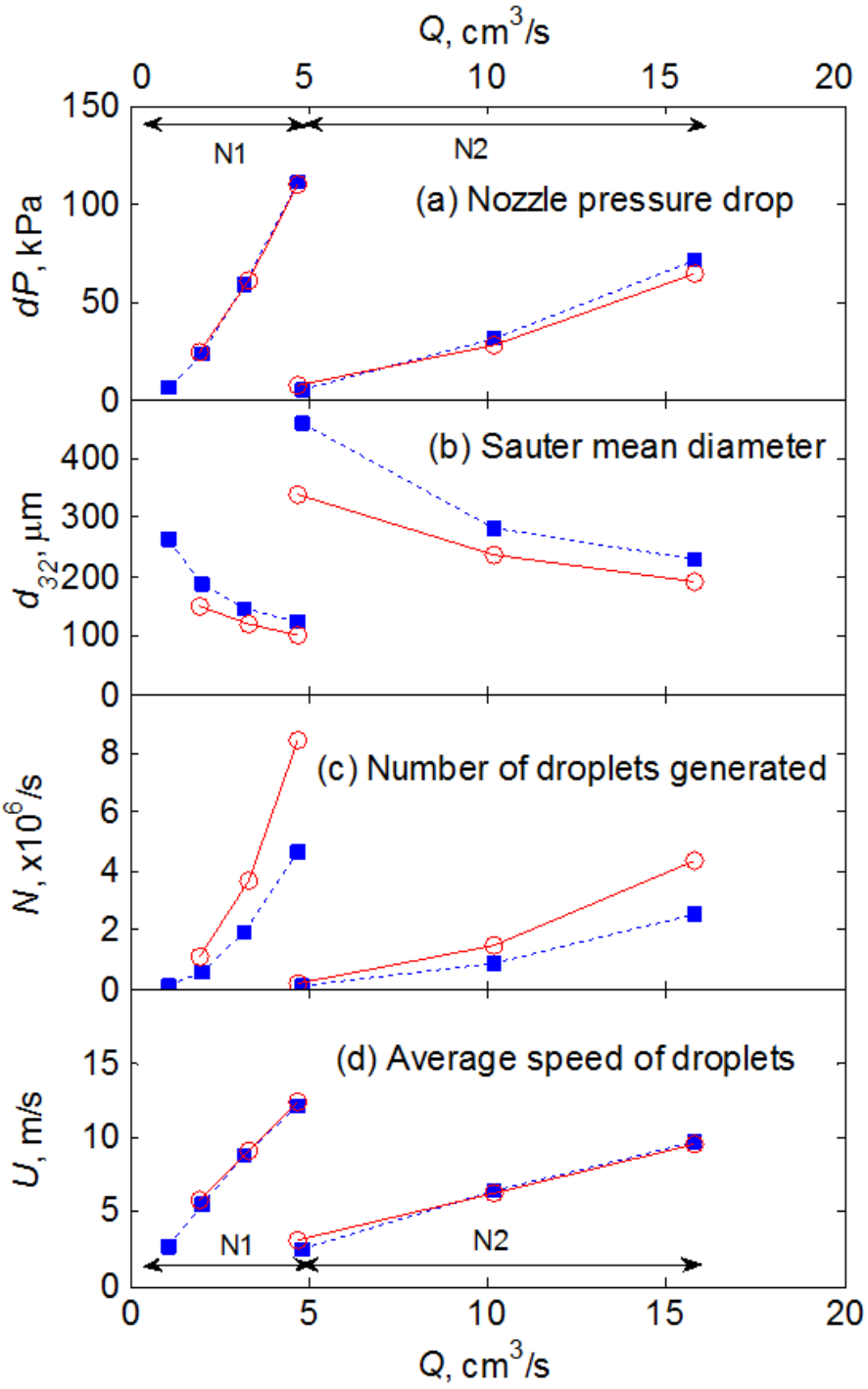

Figure III-9. Plots showing the (a) Pressure drop across the nozzle, (b) Sauter mean diameter of the droplets generated by the nozzle N1 and N2, (c) number of droplets generated per second, and (d) average speed of the droplets at various flow rates. The dotted lines correspond to data for the subcooled spray tests (ΔT_{sub}=30°C, except for the flow rate of 1.1 cm^3/s, where ΔT_{sub}=26°C), and the solid lines correspond to data for the near-saturated spray.

III.3.2 Enhancement due to Microporous Surface

Figure III-10 and Figure III-11, show the boiling curves corresponding to subcooled and near-saturated cases respectively, spray at various flow rates, on both the surfaces tested and for both spray nozzles. Consistently large performance enhancement, in terms of both the heat transfer coefficient and the CHF, are shown on the surface with the microporous coating as compared to the plain surface. In the subcooled spray tests (Figure III-10), the performance of the microporous surface is similar to that of the plain surface in the single-phase regime. Nucleate boiling on the plain surface begins at a superheat of $\gtrsim 20°C$, and the resulting increase in heat transfer, compared to the single-phase regime, is relatively modest. On the other hand, nucleate boiling on the microporous surface commences at around 3-4°C (much lower than that seen on the plain surface), due to the availability of a large range of cavities. After the onset of nucleate boiling, the slope of the boiling curve changes drastically indicating a much higher rate of heat transfer (and hence a low surface superheat temperature) on the microporous surface. This implies that the nucleate boiling contributes a much higher portion of the total heat transferred for the microporous surface than for the plain surface. These inferences are also applicable for the near-saturated case.

(a)

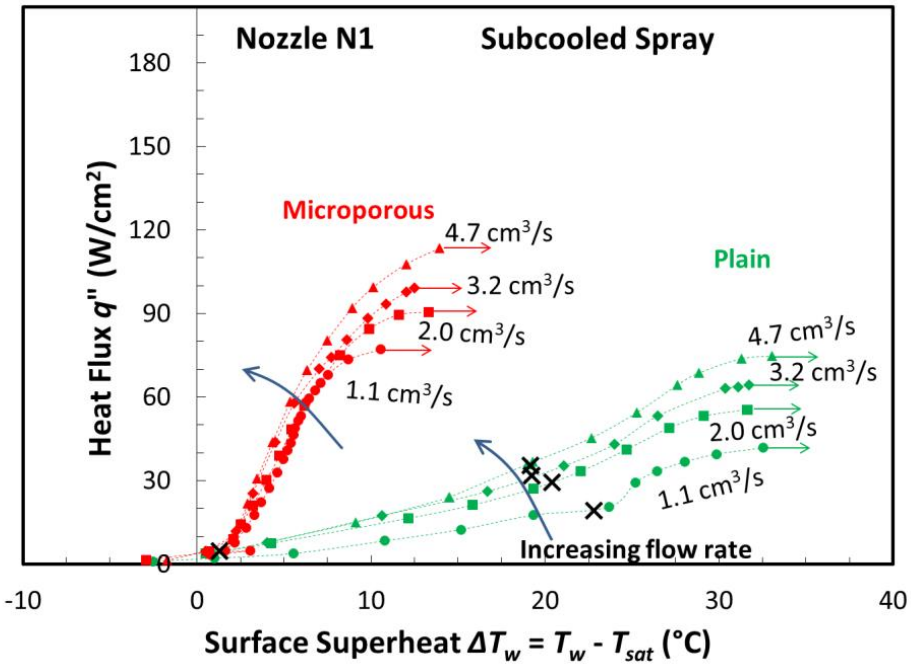

(b)

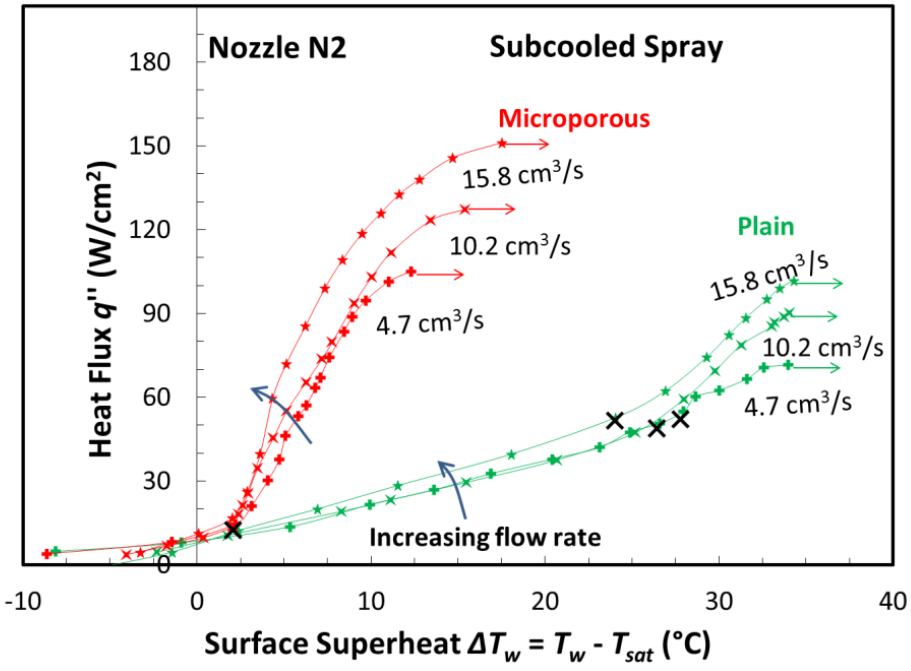

Figure III-10. Boiling curves showing the effect of the spray flow rate, with the subcooled spray with (a) nozzle N1 and (b) nozzle N2. Arrows denote CHF. The approximate point of start of nucleate boiling of marked with a "×".

(a)

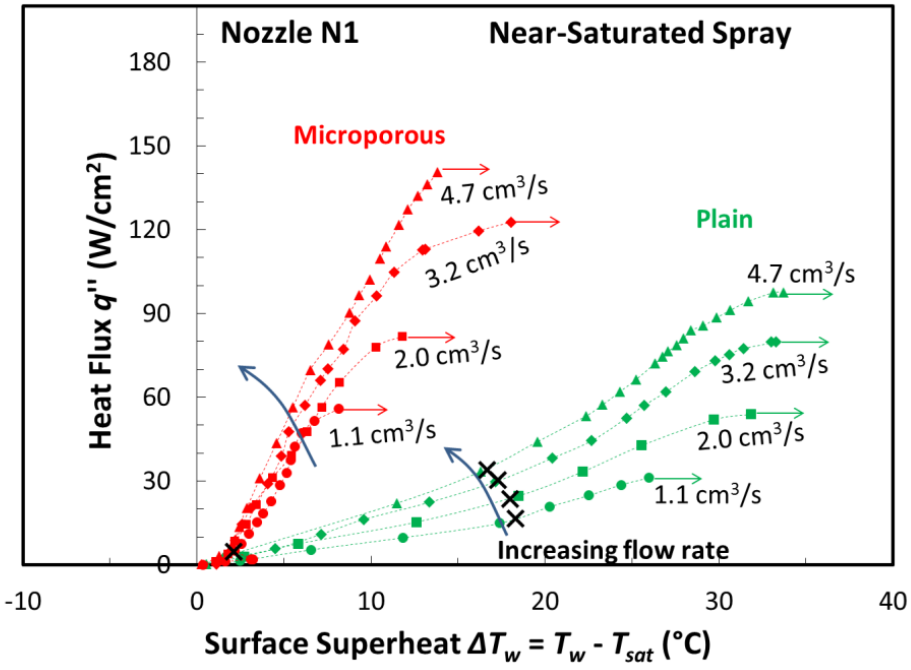

(b)

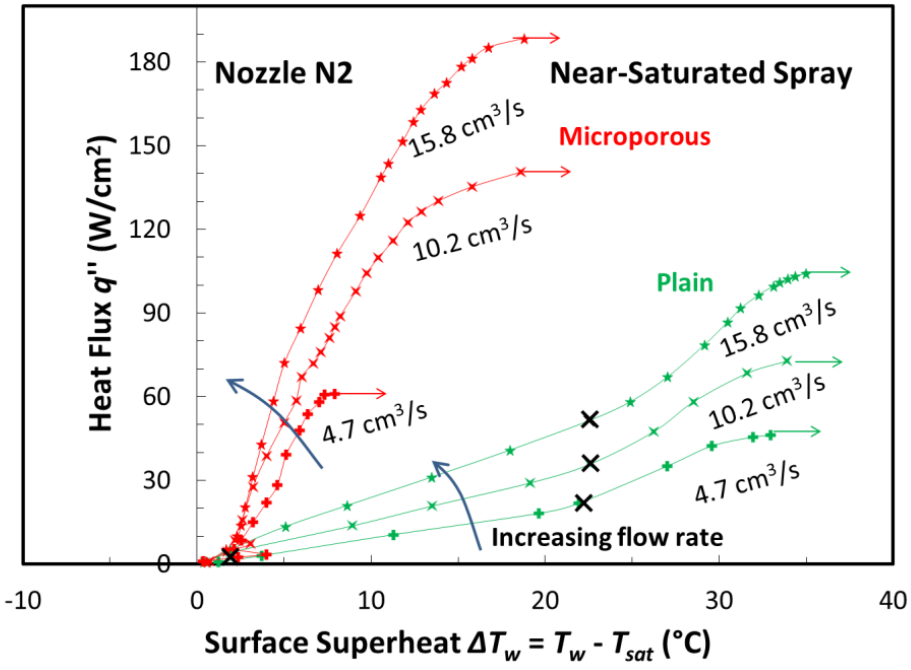

Figure III-11. Boiling curves showing the effect of flow rate, with the near-saturated spray with (a) nozzle N1 and (b) nozzle N2. Arrows denote CHF. The approximate point of start of nucleate boiling of marked with a "×".

Figure III-12 shows the heat transfer coefficient, *h*, versus the heat flux for different flow rate for the spray through nozzle N1. Figure III-13 shows the analogous data for spray through nozzle N2. The heat transfer coefficient, *h,* is calculated with the chamber (vapor) temperature (T_{sat}) as the reference using equation (III-12) for both the subcooled and near-saturated spray tests.

$$h = \frac{q''}{(T_w - T_{sat})} \tag{III-12}$$

In the subcooled spray, the *h* on the microporous surface for the flow rate of 4.7cm^3/s at the heat flux of ~70 W/cm^2 is 11.02 W/cm^2-K compared to the *h* on the plain surface of only 2.38 W/cm^2-K at the same heat flux, implying an enhancement of about 360% in the heat transfer coefficient due to the microporous coating. In addition to the higher nucleation site density, the boiling heat transfer enhancement on the microporous surface is believed to be also a result of an increase in three phase contact line length, within the numerous tunnels of the porous structure. This leads to an increased rate of thin film evaporation. This is similar to the mechanism proposed by Sodtke and Stephan [113] that spray cooling on a micro-structured surface significantly improved the cooling rates compared to plain surfaces at the same wall superheat. The microporous surface also results in a higher CHF than the plain surface for all conditions tested for otherwise identical conditions. For the subcooled spray at 4.7 cm^3/s, a CHF of 113.5 W/cm^2 is observed on the microporous surface compared to 74.7 W/cm^2 on the plain surface (52% enhancement). The enhancement of the CHF seen in the current experiments with the microporous surface could be explained by the fact that the microporous surface, by virtue of the numerous interconnected pores, results in a higher contact line length density consistent with the observation by Horacek et al. [108] who found that the heat flux dissipated from a spray cooled surface can be correlated to the three-phase contact line length density.

(a)

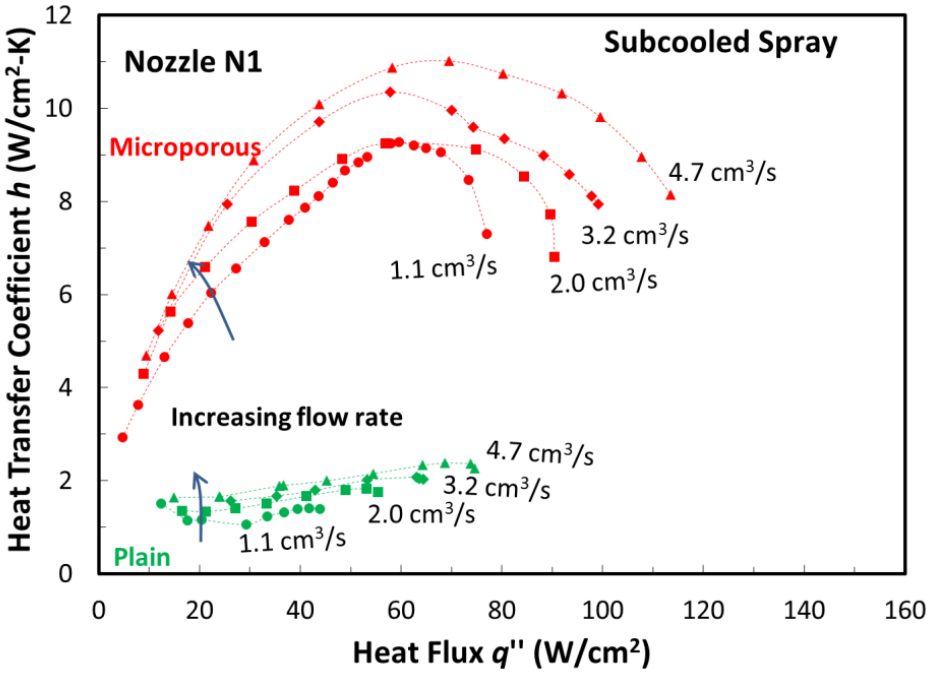

(b)

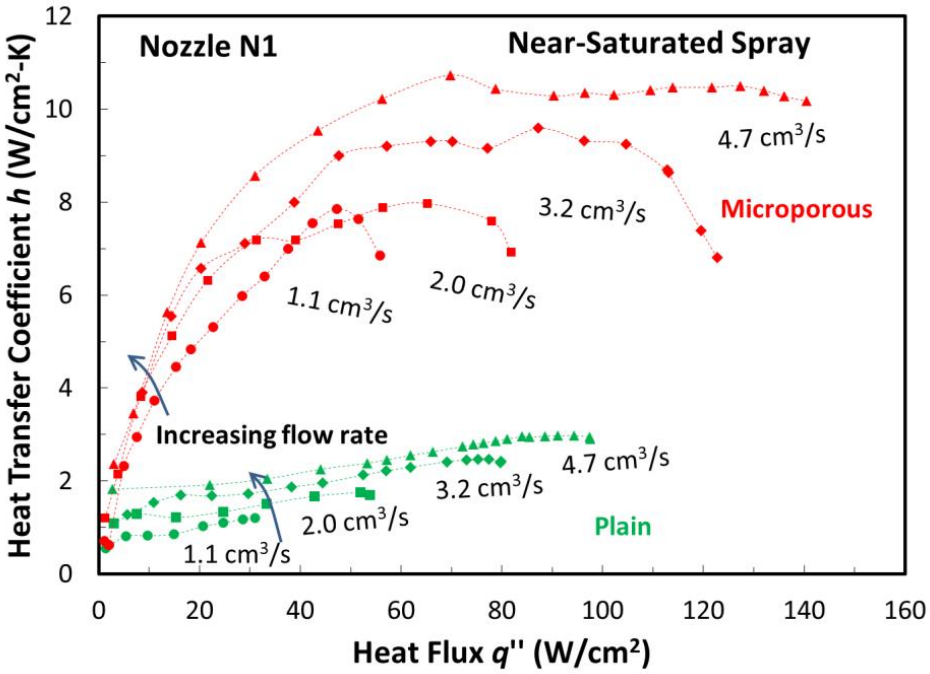

Figure III-12. Heat transfer coefficients obtained with nozzle N1 for the (a) subcooled spray and (b) near-saturated spray, at various flow rates, on the plain and microporous surface.

(a)

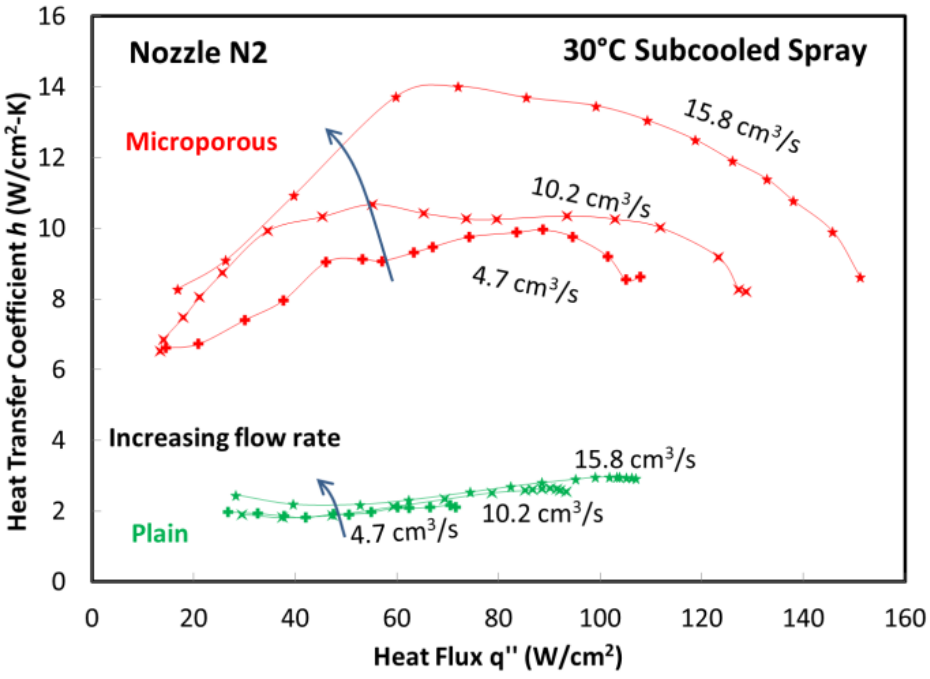

(b)

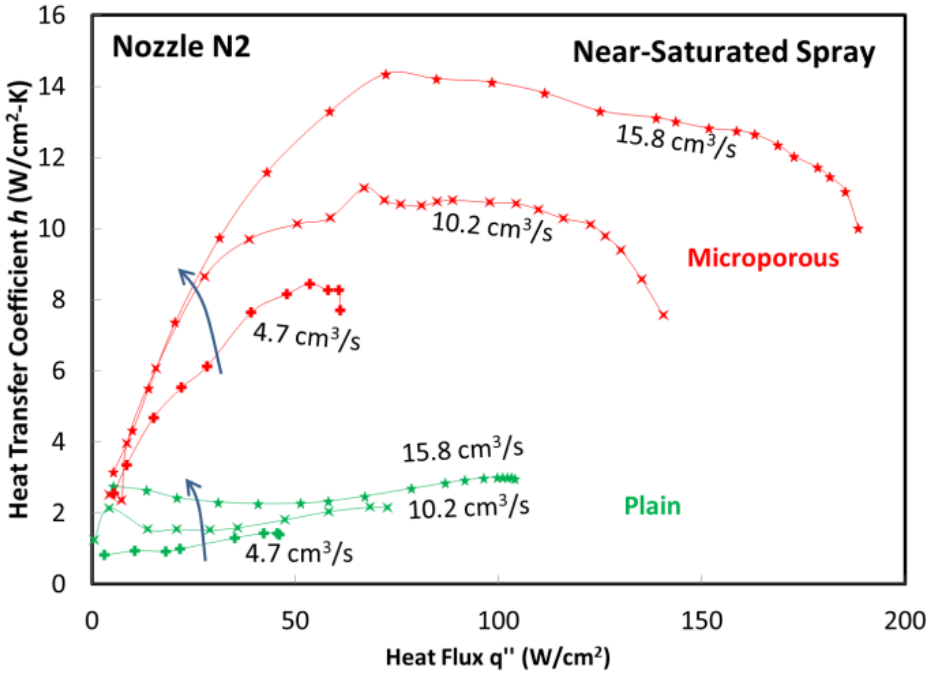

Figure III-13. Heat transfer coefficients obtained with nozzle N2 for the (a) subcooled spray and (b) near-saturated spray, at various flow rates, on the plain and microporous surface.

III.3.3 Effect of Spray Flow Rate

The heat transfer and the CHF monotonically increase with the spray flow rate for a given nozzle. In the case of a dense spray, it has previously been reported that the liquid flow rate has a relatively modest effect in the nucleate boiling regime [90,105]. The experimental data for the subcooled spray (Figure III-10 (a) and (b) corresponding to nozzle N1 and N2) shows that, on both the surfaces, the higher flow rate results in an increase in the heat flux at a given surface superheat but the effect is rather small. However, the boiling curves obtained for the near-saturated sprays (Figure III-11 (a) and (b)) show that the flow rate affects both the heat transfer and CHF very significantly. Increasing the liquid flow rate results in a concomitant increase in the number of droplets, which causes more frequent bubble puncturing on the surface and preventing the formation of dry-out spots, which results in enhanced CHF. Moreover, the vapor entrained in the droplets may act as nuclei for boiling (secondary nuclei) [110].

Figure III-14 shows CHF measured at various flow rates in the (a) subcooled and (b) near-saturated spray experiments. In each plot, the CHF are marked with open symbols on the plain surface (blue) and with solid symbols on the microporous (red). For a given nozzle, the CHF increases with increasing the flow rate, under subcooled and near-saturated conditions on both surfaces. The case of the boiling curves corresponding to the flow rate 4.7 cm^3/s using the two nozzles is particularly interesting. At the same flow rate (4.7 cm^3/s), the two nozzles produce vastly different spray characteristics (see Figure III-9). In the subcooled case, the estimated d_{32} of the droplets emerging from nozzle N1 is about 125 μm (U ~ 12.1m/s, N ~ $4.6x10^6/s$) and that of the droplets from nozzle N2 is 460 μm (U ~ 2.5m/s, N ~ $0.095x10^6/s$). Yet, when the liquid is subcooled by 30°C (Figure III-14(a)), the CHF is almost continuous between the two nozzles, for both the surfaces despite the differences between the spray characteristics, indicating that the

CHF is not influenced by the spray characteristics when the liquid is subcooled. the spray characteristics.

(a)

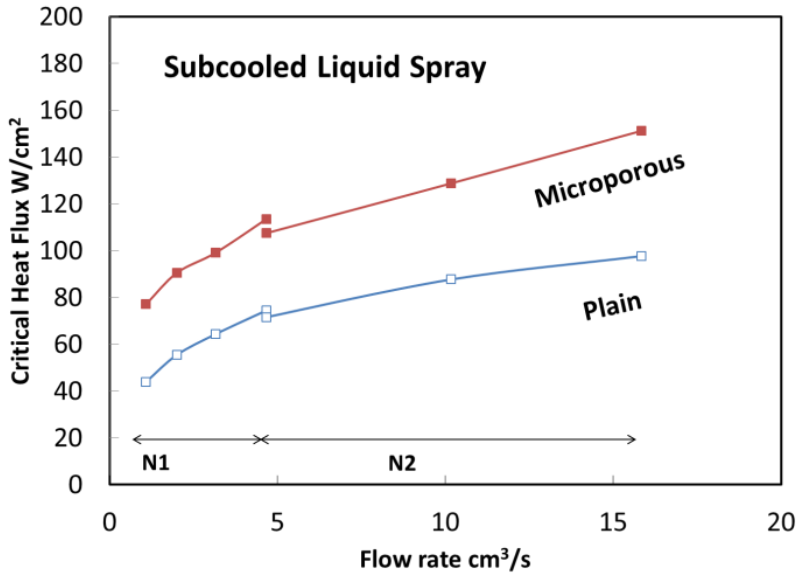

(b)

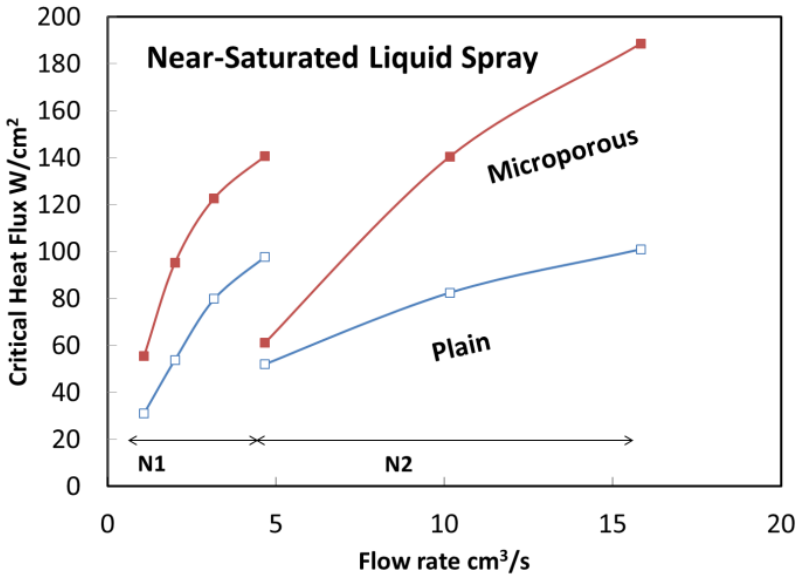

Figure III-14. Effect of flow rate on the CHF at (a) subcooled (b) near-saturated conditions. Also shown is the effect of the change of nozzle at the flow rate of 4.7 cm^3/s. Despite the large difference in the spray properties between the two nozzles, the CHF seems to depend only on the flow rate when the liquid is subcooled. However, when the liquid is near-saturated, the CHF depends on the spray characteristics in addition to the flow rate. This is true for both the plain and microporous surfaces.

On the contrary, when the liquid is near-saturated (Figure III-14(b)), the CHF decreased by 45% on the plain surface, and by 56% on the microporous surface going from nozzle N1 to N2 for the same flow rate. This shows that the CHF is strongly affected by the characteristics of the spray when the liquid is near-saturated. One possible reason is that the subcooled spray forms a thicker liquid film on the surface, thus reducing the influence of the spray parameters on the surface, while the near-saturated spray forms a thinner film and is therefore more influenced by

III.3.4 Effect of Liquid Subcooling

Figure III-15 shows the boiling curves for the subcooled and near-saturated conditions for the different surfaces for each of the flow rate tested with nozzle N1 (similar behavior is seen for the nozzle N2 but not shown here). In each plot, the solid symbols represent microporous surface and the open symbols represent the plain surface. An unusual pattern emerges from these plots: for both the surfaces, the subcooled spray performs better than the near-saturated spray at the lower flow rates, while at the higher flow rates, the near-saturated spray performs at least as well or even better than the subcooled spray. In the intermediate flow rate range, the effect of subcooling is insignificant. This is in contradiction to the expectation that heat transfer and CHF monotonically increase with subcooling [98]. To the best of our knowledge, such an effect has not been noted in the literature. Conventional understanding is that the lower temperature of the subcooled liquid enables sensible heat transfer in addition to boiling, thereby maximizing the total heat transferred. However our results show that subcooled liquid at sufficiently high flow rates can inhibit nucleation on the surface and thus result in less total heat transfer than if the liquid is near-saturated. In order to explain the counter-intuitive effect of the subcooling, we look into the efficiency of the spray cooling process under various conditions.

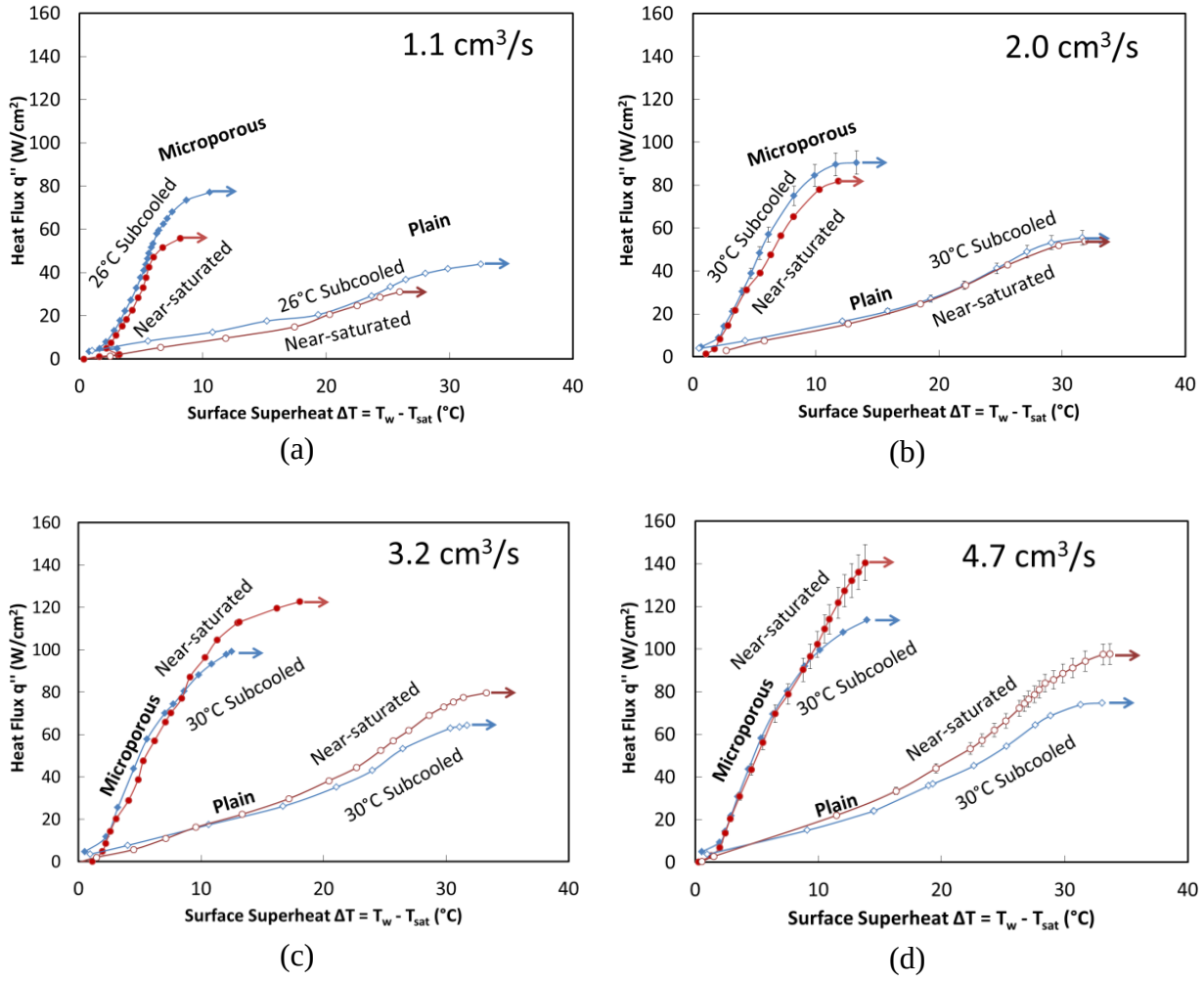

Figure III-15. Effect of subcooling at different spray flow rates on plain and microporous surfaces. Only boiling curves obtained for various spray flow rates through the nozzle N1 are shown here. When the flow rate is low, the heat transfer and CHF by the subcooled spray are better than by the saturated spray. As the flow rate increases, the additional heat transfer due to the subcooling of the spray first diminishes, and then reverses, resulting in higher heat transfer and CHF by the saturated spray than the subcooled spray.

The efficiency of the spray heat transfer is defined as the ratio of the heat transferred by the spray from the surface to the total heat that could be potentially carried by the liquid at the given flow rate and the subcooling level if it fully evaporates [104]. The experimental spray heat transfer efficiency is calculated using the following equation:

$$\eta = \frac{q"_{CHF} A}{Q \rho_l (C_P \Delta T_{sub} + h_{lv})}, \qquad \text{(III-13)}$$

where $q"_{CHF}$ denotes the critical heat flux, A is the heater surface area, Q is the flow rate, ρ_l is the density of the liquid, C_P is the specific heat of the liquid and ΔT_{sub} is the subcooling level, and h_{lv} is the latent heat of vaporization. Figure III-16 shows the overall efficiency of the heat transfer to the spray at CHF. Also shown on the Figure III-16 (a) is the maximum possible single-phase–only efficiency if the all of the heat transfer led to sensible heat and none to evaporation for the spray tests with subcooled liquid. The single-phase–only efficiency is calculated as follows

$$\eta_{1\phi} = \frac{C_P \Delta T_{sub}}{(C_P \Delta T_{sub} + h_{lv})}. \quad \text{(III-14)}$$

By definition, $\eta_{1\phi}$ is a function of only the liquid properties at a given subcooling level ($\eta_{1\phi} \approx 0$ for the near-saturated liquid). As expected [104], the efficiency decreases with increasing flow rate for both the subcooled and saturated cases. The efficiency on the microporous surface is in the range of 33% to 4.3% in the measured range of flow rates and subcooling levels, and on the plain surface 19.8% to 2.8%. The discontinuity between the nozzle N1 and N2 is a consequence of the CHF being discontinuous in the near-saturated case, as discussed previously.

(a)

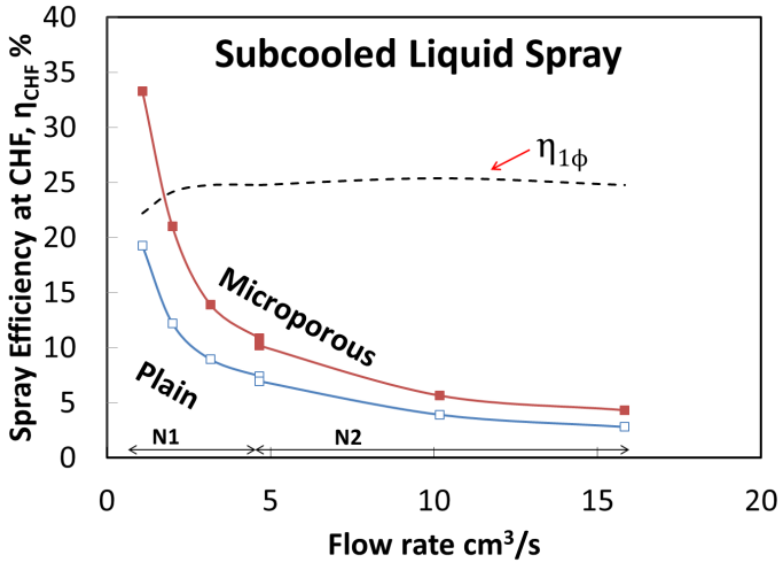

(b)

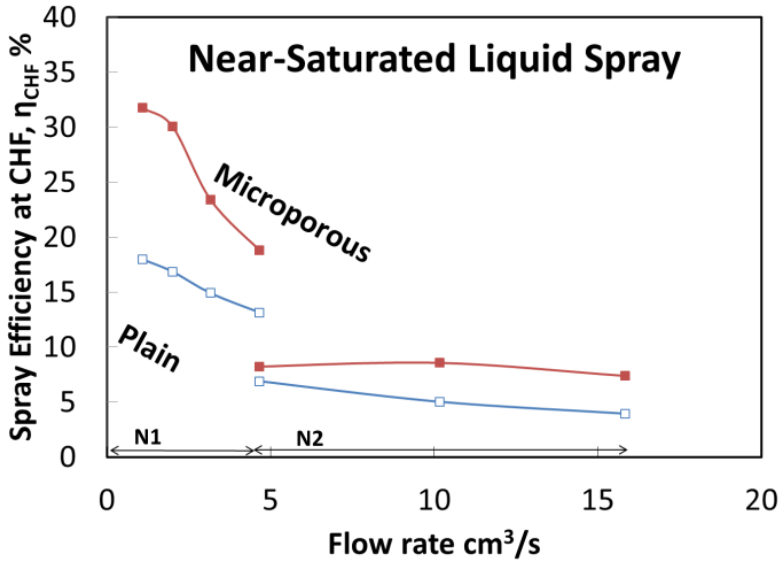

Figure III-16. Efficiency of spray heat transfer at CHF at (a) subcooled (b) near-saturated conditions.

From Figure III-16, it is seen in the subcooled spray tests, the total experimental efficiency is considerably smaller than the single-phase–only efficiency. This clearly indicates that not all the liquid is effective in removing heat. This, combined with the fact that boiling is clearly taking place in all the spray tests, shows that with increasing flow rate, only a small portion of the liquid becomes hot enough to boil, while most of the liquid droplets help in the

delay of the CHF by impingement and rupture of the vapor bubbles on the surface, without themselves directly participating in the heat transfer process. During the experiments, it is seen that a large fraction of the liquid spray hitting the heater surface scatters off the surface in the liquid state.

This observation of the liquid behavior also helps to explain the unexpected behavior seen in the effect of the flow rate between subcooled and near-saturated liquid spray—the observation that for the higher flow rates for a given nozzle, on both surfaces, the nucleate boiling heat transfer, and CHF, are higher for the near-saturated liquid than the subcooled liquid. In a dense spray cooling configuration, a thin film of the liquid forms on the surface within which the nucleation and bubble growth take place. The duration of interaction of the liquid droplets with the target surface, τ, essentially decreases with increasing flow rate ($\tau \sim 1/Q$). Given that only a small portion of the liquid evaporates, the duration of the interaction is approximately the same, regardless of whether the liquid is saturated or subcooled. The liquid droplets that reach the surface at the saturation temperature (as in the near-saturated spray tests) will immediately superheat on hitting the surface and boil. The liquid droplets that are subcooled, though, will first have to heat sensibly until they reach the saturation temperature before they can boil. Because of the limited time spent by the liquid on the heater surface and the much higher rate of phase change heat transfer compared to sensible heat transfer, it is conceivable that the saturated liquid droplets will undergo phase change faster, removing more heat than the liquid droplets that strike the surface at subcooled conditions.

III.3.5 CHF Correlation

III.3.5.1 Plain surface

Using dimensional analysis, Monde and Katto [119] showed that the CHF data for a jet impingement boiling system can be correlated according to a single dimensionless equation in terms of density ratio, Weber number, and Jakob number, using empirical coefficients and exponents. Mudawar and Valentine [98] modified the Monde-Katto correlation by replacing the characteristic velocity and length in the equation by the volumetric flux and Sauter mean diameter, respectively, for spray cooling CHF. They correlated CHF for a small circular heater situated in a large impact area according to the equation

$$\frac{q"}{\rho_v h_{lv} Q"} = f\left[\frac{\rho_l}{\rho_v}, \frac{\rho_l C_P \Delta T_{sub}}{\rho_v h_{lv}}, \frac{\rho_l Q"^2 d_{32}}{\sigma}\right], \qquad \text{(III-15)}$$

where $Q"$ is the volumetric flux, and $q"$ is the heat flux based on the total area of the surface, ρ_v is the density of the vapor, ρ_l is the density, σ is the surface tension, C_P is the specific heat of the liquid, ΔT_{sub} is the subcooling level, and h_{lv} is the latent heat of vaporization. Based on the work of Mudawar and Valentine, Mudawar and Estes [118] developed a correlation for the CHF, as discussed in section (III.3.5):

$$\frac{q"}{\rho_v h_{lv} Q"} = 2.3\left(\frac{\rho_l}{\rho_v}\right)^{0.3}\left(\frac{\rho_l Q"^2 d_{32}}{\sigma}\right)^{-0.35}\left(1 + 0.0019\frac{\rho_l C_P \Delta T_{sub}}{\rho_v h_{lv}}\right). \qquad \text{(III-16)}$$

They postulated that for a configuration where the spray impact circle just inscribes the square heater, CHF would commence at the outer edge of the spray impact area, where volumetric flux is a minimum, and propagate inward in an unstable manner. When applied to the data from our experiments, this correlation was found to over-predict the experimentally observed CHF for all cases (with the plain surface) despite adhering to the conditions prescribed

for the usage of this correlation. A modified correlation was derived based on our data, using the same dimensionless groups:

$$\frac{q"}{\rho_v h_{lv} Q"} = 1.449 \left(\frac{\rho_l}{\rho_v}\right)^{0.3} \left(\frac{\rho_l Q"^2 d_{32}}{\sigma}\right)^{-0.3371} \left(1 + 0.0058 \frac{\rho_l C_P \Delta T_{sub}}{\rho_v h_{lv}}\right). \qquad \text{(III-17)}$$

Here, the liquid and vapor properties are evaluated at the average temperature between the T_{in} and T_{sat}. This correlation was applied to spray cooling data from the following sources, in addition to data from this study:

1. Lin and Ponnappan [103]: Dielectric coolants FC-87, FC-72, and methanol.
2. Rini et al. [110] : FC-72
3. Silk [120]: PF-5060
4. Coursey et al. [36]: PF-5060
5. Chen et al. [89]: Water
6. Puterbaugh et al. [121]: FC-72 (with presence of 1–20 v/v% of non-condensable gas).

The experimental data is compared against the prediction from the correlation in equation (III-17) in Figure III-17. The correlation works well for the dielectric coolants, with a mean absolute error of 16%; however, it over-predicted the CHF for water, and under-predicted the CHF for methanol as shown in Figure III-18 (a). The original Estes-Mudawar correlation seems to predict better when considering both methanol and water experimental data, as shown in Figure III-18 (b).

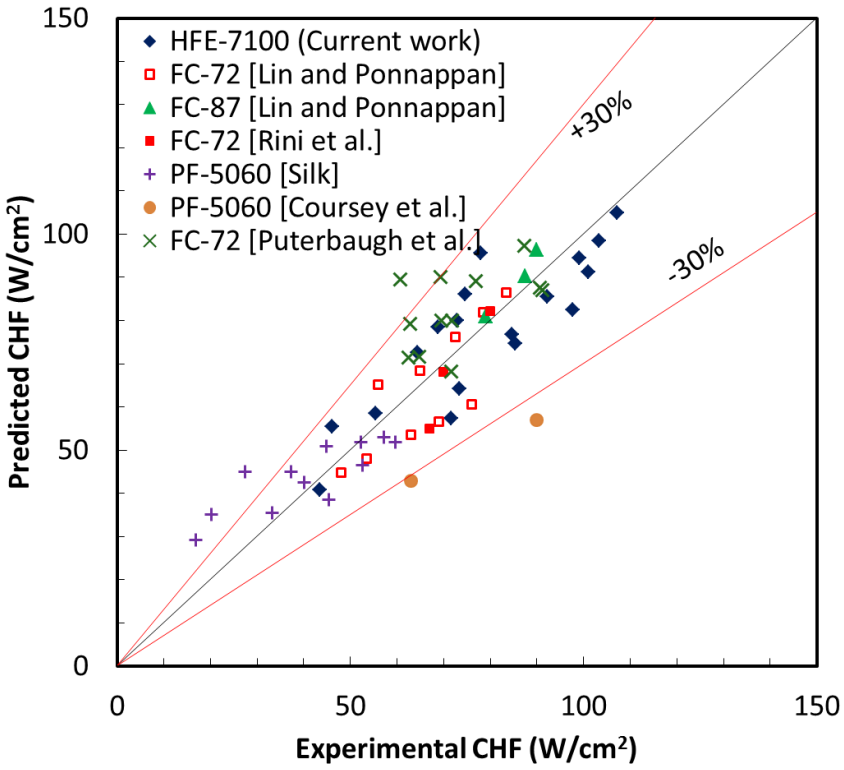

Figure III-17. Measured versus Predicted CHF for dielectric liquids using the modified correlation provided in equation (III-17) for the plain surface. The correlation predicts the experimental CHF with a mean absolute error of 16% for the dielectric liquids. The outliers in the dielectric liquids are those measured using gassy liquids.

(a)

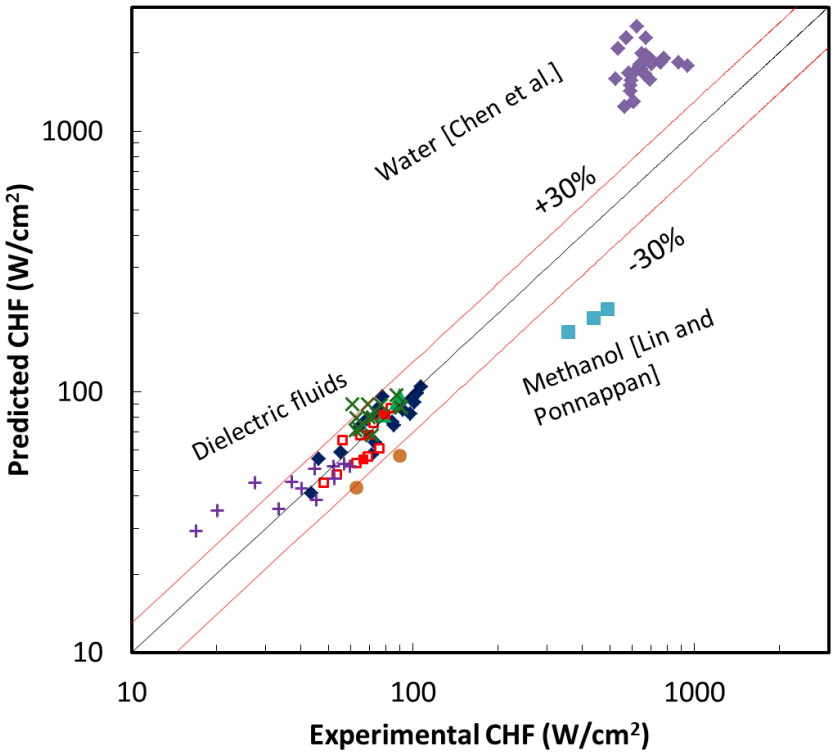

(b)

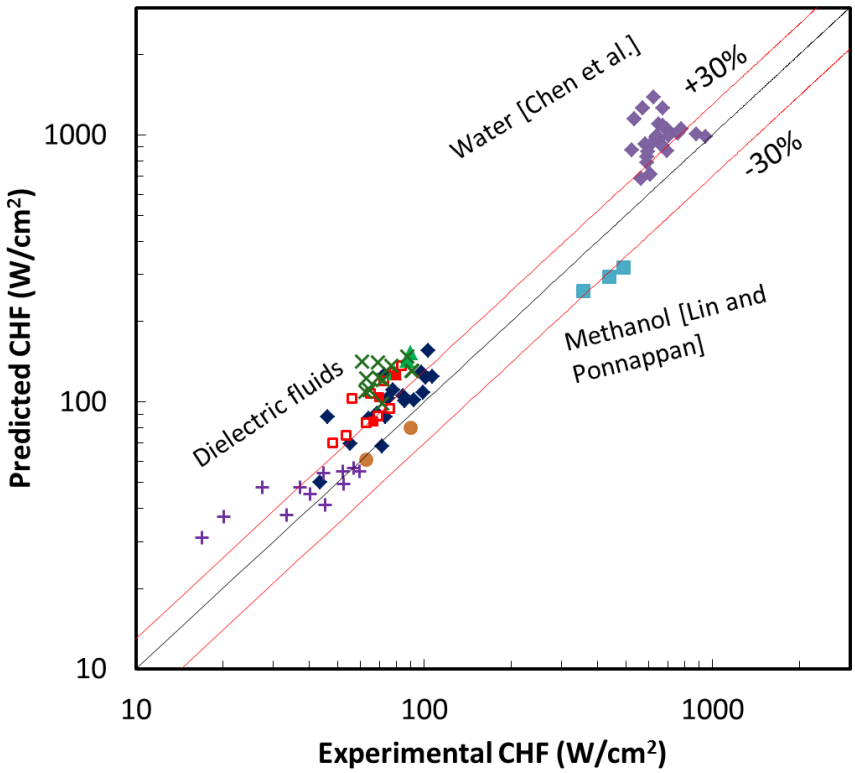

Figure III-18. Measured versus predicted CHF on plain surfaces for dielectric liquids, water, and methanol using (a) the modified correlation, equation (III-17), and (b) the Estes-Mudawar correlation, equation (III-16).

III.3.5.2 Microporous surface

To fit the experimental data generated for the microporous surface, the correlation was modified in equation (III-18) as follows:

$$\frac{q"}{\rho_v h_{lv} Q"} = 2.139\left(\frac{\rho_l}{\rho_v}\right)^{0.3}\left(\frac{\rho_l Q"^2 d_{32}}{\sigma}\right)^{-0.363}\left(1 + 0.0058\frac{\rho_l C_P \Delta T_{sub}}{\rho_v h_{lv}}\right). \qquad \text{(III-18)}$$

The mean absolute error for this fit is 9.8% with respect to the experimental data from this study for both the subcooled and near-saturated spray conditions as shown in Figure III-19. This correlation was applied to spray cooling data on enhanced surfaces from the following sources, in addition to the experimental data from this study:

1. Coursey et al. [36]: PF-5060 on open, copper microchannel surface
2. Silk et al. [34]: PF-5060 on enhanced surfaces with cubic pin fins, pyramids and straight fins.

This is a semi-empirical correlation that could be used as a predictive tool to estimate the CHF that could be obtained under various conditions for a spray on an enhanced surface.

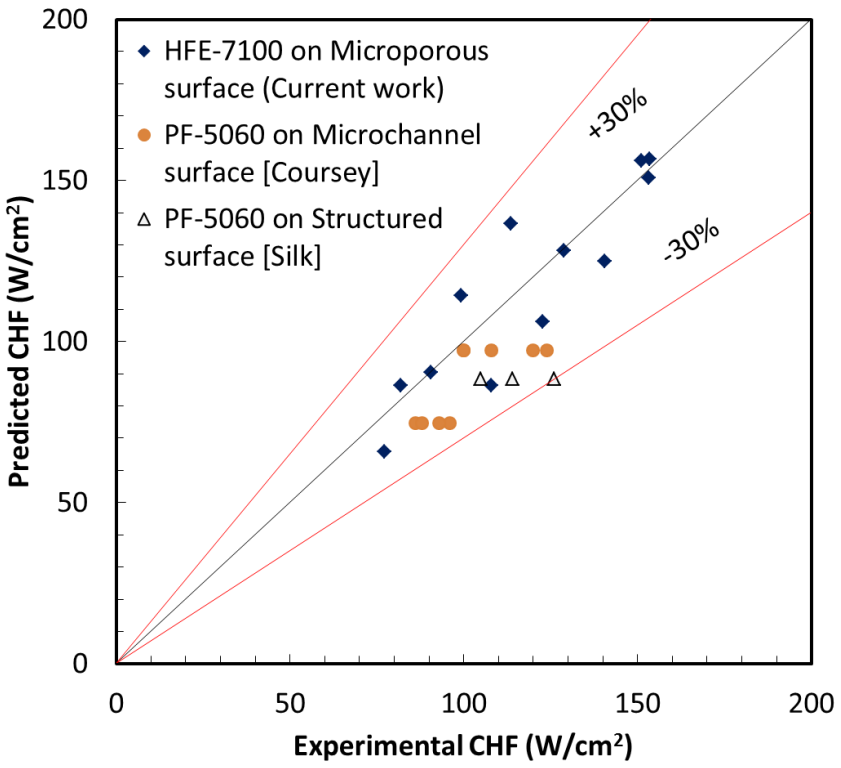

Figure III-19. Measured versus Predicted CHF for HFE-7100 spray on the microporous surface in the current study, and PF-5060 on structured and microchannel surfaces. The correlation is from equation (III-18). The mean absolute error is 9.8%.

III.4 Summary

Spray impingement boiling experiments were performed on the copper surface coated with a thermally conductive copper microporous coating, in comparison with a plain copper surface. Spray experiments were performed at flow rates ranging from 1.1 cm^3/s to 15.8 cm^3/s using two different spray nozzles with liquid subcooling of 30°C and ~0°C. Very high heat transfer performances were obtained with the microporous surfaces, in comparison with the plain surface. Under all conditions tested, the microporous surface showed lower boiling incipience temperature (3-4°C) than the plain surface ($\gtrsim$ 20°C). The CHF increased by more than 50%-

80% for the microporous surface over the plain surface for identical conditions, depending on the flow rate.

The spray parameters had little influence on the CHF when the spray was subcooled. When the spray was near-saturated, however, the spray parameters had a strong influence on the CHF. It was observed that at low flow rates for either nozzle, the subcooling of the liquid resulted in a higher heat flux throughout the nucleate boiling regime, including CHF. With high flow rate sprays, though, the subcooling had a detrimental effect on the heat transfer coefficient at the high heat fluxes. Moreover, the CHF also decreased with the subcooling at higher flow rates for both surfaces. This counter-intuitive effect of the subcooling likely results from the limited residence time of the liquid droplets in contact with the heater surface and the much higher efficiency of phase-change heat transfer. The near-saturated spray undergoes phase change much faster than the subcooled liquid, removing heat more efficiently than the subcooled liquid. Modified correlations based on the Estes-Mudawar [112] correlation were developed to predict the experimentally observed CHF data for both plain and microporous surfaces.

Chapter IV Conclusions and Future Work

In this work, we explored the enhancement of the liquid-vapor phase-change heat transfer that is obtained using a thermally conductive copper microporous surface in pool boiling and spray impingement boiling configurations. The conclusions from the work on pool boiling and spray impingement boiling are as follows.

IV.1 Enhancement of Pool Boiling

We experimentally studied the pool boiling heat transfer performance of copper surfaces coated with thermally conductive microporous copper layer, in comparison with plain surfaces of two different roughness levels. The target surfaces were 10 mm long and 2 mm wide. This narrow dimension was chosen so that bubble activity over the whole surface could be seen in the high-speed visualization.

- Better heat transfer performances were observed with the microporous surface. Under all conditions tested, the microporous surface showed lower boiling incipience temperature (3 – 11 °C) than the plain surface (17 – 38 °C) due to the presence of cavities in the size range 1 to 5 μm in large numbers on the microporous surface. Based on the Hsu's criterion for active nucleating cavity sizes, it was determined that the relevant contact angle of the liquid-vapor interface is the dynamic contact angle (>15°), much larger than the static contact angle (~1°).

- The heat transfer coefficient increased by 50 – 270% on the microporous surface as a result of the much larger nucleate site density than plain surfaces. The CHF was enhanced by 33 to 60% for the microporous surface over the plain surface.
- A comparison with the literature on pool boiling with HFE-7100 on various structured surfaces shows the enhancement provided by the microporous surface is among the highest.
- High speed visualization was utilized to obtain information on the bubble site density, departure diameter and frequency of departure on the different surfaces. On all the surfaces, the bubble site density and frequency of departure increases sharply with temperature, while the diameter at departure stays relatively insensitive to temperature.
- The Hibiki-Ishii correlation [74] was found to work very well for the nucleation site density on the plain surfaces if the contact angle is assumed to be in the range 41° to 48°. The same correlation was modified to predict the nucleation site density on the microporous surfaces also.
- The experimental data for the average bubble diameter at departure was found to be predicted well by the correlation by Phan et al. [81], when used with the same contact angle used in the nucleation site density correlation.
- No correlation in the literature was found to predict the magnitude and steeply increasing trend in the frequency of departure of the bubbles.
- The experimental bubble dynamics data collected in the isolated bubbles regime (with heat flux < 10 W/cm^2) was extended using the correlations to the full temperature range until CHF. Using the information on the bubble site density, departure diameter and frequency of departure, a simple heat flux partition model that neglects the effects of bubble

coalescence, was applied to obtain the contribution of various modes of heat transfer to the fluid from the various target surfaces.

- On the plain surfaces, both evaporative and quenching components contributes nearly equally to the total heat flux. On the microporous surfaces, the evaporative component contributes about 70% to the total heat, thus confirming that the microporous coating enhances nucleate boiling heat transfer as a direct result of its significantly higher active nucleation site density.

IV.2 Enhancement of Spray Boiling

We performed spray impingement boiling experiments on vertically oriented 10 mm x 10 mm copper surface coated with a thermally conductive copper microporous coating, in comparison with a plain copper surface, and studied the heat transfer performance. The flow rates ranging from 1.1 cm^3/s to 15.8 cm^3/s using two different spray nozzles with liquid subcooling of 30 °C and ~0 °C was studied.

- Very high heat transfer performances were obtained with the microporous surfaces, in comparison with the plain surface. Under all conditions tested, the microporous surface showed lower boiling incipience temperature (3-4 °C) than the plain surface ($\gtrsim$ 20 °C). The CHF increased by more than 50%-80% for the microporous surface over the plain surface for identical conditions, depending on the flow rate.
- The maximum CHF of 187 W/cm^2 was attained with the microporous surface, and the near-saturated liquid spray (subcooling ~ 0 °C) at flow rate of 15.8 cm^3/s. This is compared to the largest CHF of 104 W/cm^2 attained on the plain surface, under the same conditions.

- The spray parameters had little influence on the CHF when the spray was subcooled. When the spray was near-saturated, however, the spray parameters had a strong influence on the CHF.
- It was observed that at low flow rates for either nozzle, the subcooling of the liquid resulted in a higher heat flux throughout the nucleate boiling regime, including CHF.
- With high flow rate sprays, though, the subcooling had a detrimental effect on the heat transfer coefficient at the high heat fluxes. Moreover, the CHF also decreased with the subcooling at higher flow rates for both surfaces. This counter-intuitive effect of the subcooling likely results from the limited residence time of the liquid droplets in contact with the heater surface and the much higher efficiency of phase-change heat transfer. The near-saturated spray undergoes phase change much faster than the subcooled liquid, removing heat more efficiently than the subcooled liquid.
- Modified correlations based on the Estes-Mudawar [112] correlation were developed to predict the experimentally observed CHF data for both plain and microporous surfaces.

IV.3 Recommendation for Future Work

- Since water is the most commonly used coolant, pool boiling and spray cooling experiments should be conducted using water on the microporous coated surfaces. The enhancement of heat transfer or the lack thereof would provide information on the effect of the size scale of the pores in the microporous surface on the site density and consequently, the heat transfer performance.

- In order to elucidate the reason for the enhanced contribution of phase-change heat versus quenching/single-phase on the microporous surface, very high-speed and high-magnification visualization experiments could be designed to study the liquid-vapor and temperatures distribution within a vertical slice of the microporous layer.
- An interesting aspect of spray impingement boiling discovered in this work was the effect of subcooling on the heat transfer coefficient and CHF. That the liquid subcooling (at high liquid flow rates for a given nozzle) can actually result in reduced heat transfer and CHF (compared to saturated liquid spray) suggests that by appropriate design, the subcooling requirement in a practical application of spray cooling may be eliminated/reduced. Further understanding of this phenomenon could be obtained by performing a matrix of experiments spanning a wide range of flow rate and subcooling levels. As this phenomenon is also observed on the plain surface, a visualization study using a transparent ITO (Indium tin oxide) thin film heater combined with a measurement of the thickness of the liquid thin film on the heated surface would provide valuable information needed to construct a theoretical and quantitative model for the heat transfer.
- Dense spray heat transfer on the microporous surfaces was studied in this work. The performance of the microporous surface under a low flow rate evaporative spray was not investigated. Further experimental work could focus on low flow rate/low pressure drop systems with spray efficiency approaching 100%. That would reveal the heat transfer enhancement due to the increased surface area of the coated surface and liquid spreading afforded by the microporous layer, rather than the effect of the increase in nucleation site density.

References

[1] I. Mudawar, Assessment of high-heat-flux thermal management schemes, IEEE Trans. Components Packag. Technol. 24 (2) (2001) 122–141.

[2] I. Mudawar, D. Bharathan, K. Kelly, S. Narumanchi, Two-phase spray cooling of hybrid vehicle electronics, IEEE Trans. Components Packag. Technol. 32 (2009) 501–512.

[3] 3M product brochure, 3M microporous metallic boiling enhancement coating (BEC) L-20227, (2008).

[4] P.E. Tuma, Evaporator/boiler design for thermosyphons utilizing segregated hydrofluoroether working fluids, in: 22nd Annu. IEEE Semicond. Therm. Meas. Manag. Symp., 2006: pp. 69–77.

[5] V.P. Carey, Liquid-vapor phase-change phenomena: an introduction to the thermophysics of vaporization and condensation processes in heat transfer equipment, 2nd ed., Taylor and Francis, New York, 2007.

[6] J.H. Kim, S.M. You, S.U.S. Choi, Evaporative spray cooling of plain and microporous coated surfaces, Int. J. Heat Mass Transf. 47 (14-16) (2004) 3307–3315.

[7] C. Hsieh, S. Yao, Evaporative heat transfer characteristics of a water spray on micro-structured silicon surfaces, Int. J. Heat Mass Transf. 49 (2006) 962–974.

[8] P.J. Berenson, Experiments on pool-boiling heat transfer, Int. J. Heat Mass Transf. 5 (10) (1962) 985–999.

[9] C.P. Costello, W.J. Frea, The roles of capillary wicking and surface deposits in the attainment of high pool boiling burnout heat fluxes, AIChE J. 10 (3) (1964) 393–398.

[10] P.J. Marto, L.V.J. Lepere, Pool boiling heat transfer from enhanced surfaces to dielectric fluids, J. Heat Transfer 104 (2) (1982) 292–299.

[11] S. Oktay, A.F. Schmeckenbecher, Preparation and Performance of Dendritic Heat Sinks, J. Electrochem. Soc. 121 (7) (1974) 912.

[12] M.E. Poniewski, J.R. Thome, Nucleate boiling on micro-structured surfaces, Heat Transfer Research, Inc. (HTRI), 2008.

[13] I. Mudawar, T.M. Anderson, Parametric Investigation Into the Effects of Pressure, Subcooling, Surface Augmentation and Choice of Coolant on Pool Boiling in the Design of Cooling Systems for High-Power-Density Electronic Chips, J. Electron. Packag. 112 (4) (1990) 375–382.

[14] I. Mudawar, Direct-immersion cooling for high power electronic chips, in: [1992 Proceedings] Intersoc. Conf. Therm. Phenom. Electron. Syst., IEEE, 1992: pp. 74–84.

[15] R.L. Webb, N.-H. Kim, Principles of enhanced heat transfer, Taylor & Francis Group, 2005.

[16] R.L. Webb, The evolution of enhanced surface geometries for nucleate boiling, Heat Transf. Eng. 2 (3-4) (1981) 46–69.

[17] R.L. Webb, Nucleate boiling on porous coated surfaces, Heat Transf. Eng. 4 (3-4) (1983) 71–82.

[18] A.E. Bergles, M.C. Chyu, Characteristics of nucleate pool boiling from porous metallic coatings, J. Heat Transfer 104 (2) (1982) 279–285.

[19] N.H. Afgan, L.A. Jovic, S.A. Kovalev, V.A. Lenykov, Boiling heat transfer from surfaces with porous layers, Int. J. Heat Mass Transf. 28 (2) (1985) 415–422.

[20] J.R. Thome, Enhanced boiling heat transfer, Hemisphere Publishing Corporation, New York, 1990.

[21] J.Y. Chang, S.M. You, Boiling heat transfer phenomena from microporous and porous surfaces in saturated FC-72, Int. J. Heat Mass Transf. 40 (18) (1997) 4427–4447.

[22] J.H. Kim, K.N. Rainey, S.M. You, J.Y. Pak, Mechanism of nucleate boiling heat transfer enhancement from microporous surfaces in saturated FC-72, J. Heat Transfer 124 (3) (2002) 500–506.

[23] K.N. Rainey, S.M. You, S. Lee, Effect of pressure, subcooling, and dissolved gas on pool boiling heat transfer from microporous, square pin-finned surfaces in FC-72, J. Heat Transfer 125 (2003) 75–83.

[24] S.M. You, T.W. Simon, A. Bar-Cohen, A technique for enhancing boiling heat transfer with application to cooling of electronic equipment, in: [1992 Proceedings] Intersoc. Conf. Therm. Phenom. Electron. Syst., IEEE, 1992: pp. 66–73.

[25] J.P. O'Connor, S.M. You, A painting technique to enhance pool boiling heat transfer in saturated FC-72, J. Heat Transfer 117 (2) (1995) 387.

[26] K.N. Rainey, S.M. You, Pool boiling heat transfer from plain and microporous, square pin-finned surfaces in saturated FC-72, J. Heat Transfer 122 (3) (2000) 509–516.

[27] K.N. Rainey, G. Li, S.M. You, Flow boiling heat transfer from plain and microporous coated surfaces in subcooled FC-72, J. Heat Transfer 123 (5) (2001) 918.

[28] S.M. You, K.N. Rainey, C.N. Ammerman, A new microporous surface coating for enhancement of pool and flow boiling heat transfer, in: Adv. Heat Transf., 2004: pp. 73–142.

[29] M.S. El-Genk, J.L. Parker, Enhanced boiling of HFE-7100 dielectric liquid on porous graphite, 46 (2005) 2455–2481.

[30] G.S. Hwang, M. Kaviany, Critical heat flux in thin, uniform particle coatings, Int. J. Heat Mass Transf. 49 (5-6) (2006) 844–849.

[31] C. Li, G.P. Peterson, Parametric Study of Pool Boiling on Horizontal Highly Conductive Microporous Coated Surfaces, J. Heat Transfer 129 (11) (2007) 1465.

[32] C. Li, G.P. Peterson, Experimental Studies on CHF of Pool Boiling on Horizontal Conductive Micro Porous Coated Surfaces, AIP Conf. Proc. 969 (1) (2008) 12–20.

[33] M.R. Pais, L.C. Chow, E.T. Mahefkey, Surface roughness and its effects on the heat transfer mechanism in spray cooling, J. Heat Transfer 114 (1) (n.d.) 211–219.

[34] E.A. Silk, J. Kim, K. Kiger, Spray cooling of enhanced surfaces: Impact of structured surface geometry and spray axis inclination, Int. J. Heat Mass Transf. 49 (25-26) (2006) 4910–4920.

[35] E.A. Silk, Investigation of Pore Size Effect On Spray Cooling Heat Transfer With Porous Tunnels, in: AIP Conf. Proc., AIP, 2008: pp. 112–122.

[36] J.S. Coursey, J. Kim, K.T. Kiger, Spray cooling of high aspect ratio open microchannels, J. Heat Transfer 129 (8) (2007) 1052–1059.

[37] H. Bostanci, D.P. Rini, J.P. Kizito, L.C. Chow, Spray cooling with ammonia on microstructured surfaces: performance enhancement and hysteresis effect, J. Heat Transfer 131 (7) (2009) 071401:1–9.

[38] H. Bostanci, D.P. Rini, J.P. Kizito, V. Singh, S. Seal, L.C. Chow, High heat flux spray cooling with ammonia: Investigation of enhanced surfaces for CHF, Int. J. Heat Mass Transf. 55 (13-14) (2012) 3849–3856.

[39] 3M product brochure, 3M Novec™ engineered fluid HFE-7100 for heat transfer, (2002).

[40] S. Moghaddam, K. Kiger, Physical mechanisms of heat transfer during single bubble nucleate boiling of FC-72 under saturation conditions-II: Theoretical analysis, Int. J. Heat Mass Transf. 52 (5-6) (2009) 1295–1303.

[41] M. Jakob, W. Linke, Boiling heat transfer, Phys. Z. 636 (1935) 267–273.

[42] W.M. Rohsenow, A method of correlating heat transfer data for surface boiling of liquids, J. Heat Transfer 74 (1952) 969–976.

[43] C.L. Tien, A hydrodynamic model for nucleate pool boiling, Int. J. Heat Mass Transf. 5 (6) (1962) 533–540.

[44] N. Zuber, Nucleate boiling. The region of isolated bubbles and the similarity with natural convection, Int. J. Heat Mass Transf. 6 (1) (1963) 53–78.

[45] K.E. Forster, R. Greif, Heat transfer to a boiling liquid, J. Heat Transfer 81 (1959) 43–53.

[46] B.B. Mikic, W.M. Rohsenow, A new correlation of pool-boiling data including the effect of heating surface characteristics, J. Heat Transfer 91 (2) (1969) 245–250.

[47] S. Haider, R. Webb, A transient micro-convection model of nucleate pool boiling, Int. J. Heat Mass Transf. 40 (15) (1997) 3675–3688.

[48] R.L. Judd, K.S. Hwang, A Comprehensive Model for Nucleate Pool Boiling Heat Transfer Including Microlayer Evaporation, J. Heat Transfer 98 (4) (1976) 623.

[49] V.K. Dhir, Boiling Heat Transfer, Annu. Rev. Fluid Mech. 30 (1) (1998) 365–401.

[50] R.J. Benjamin, A.R. Balakrishnan, Nucleate pool boiling heat transfer of pure liquids at low to moderate heat fluxes, Int. J. Heat Mass Transf. 39 (12) (1996) 2495–2504.

[51] S. Moghaddam, K. Kiger, Physical mechanisms of heat transfer during single bubble nucleate boiling of FC-72 under saturation conditions-I. Experimental investigation, Int. J. Heat Mass Transf. 52 (5-6) (2009) 1284–1294.

[52] S.J.D. van Stralen, The mechanism of nucleate boiling in pure liquids and in binary mixtures—part I, Int. J. Heat Mass Transf. 9 (10) (1966) 995–1006.

[53] B.B. Mikic, W.M. Rohsenow, P. Griffith, On bubble growth rates, Int. J. Heat Mass Transf. 13 (4) (1970) 657–666.

[54] H.K. Forster, N. Zuber, Dynamics of vapor bubbles and boiling heat transfer, AIChE J. 1 (4) (1955) 531–535.

[55] A. Luke, D.-C. Cheng, High speed video recording of bubble formation with pool boiling, Int. J. Therm. Sci. 45 (2006) 310–320.

[56] C. Gerardi, J. Buongiorno, L. Hu, T. McKrell, Study of bubble growth in water pool boiling through synchronized, infrared thermometry and high-speed video, Int. J. Heat Mass Transf. 53 (19-20) (2010) 4185–4192.

[57] J. McHale, S. Garimella, Nucleate boiling from smooth and rough surfaces–Part 2: analysis of surface roughness effects on nucleate boiling, Exp. Therm. Fluid Sci. 44 (2013) 439–455.

[58] C.Y. Ho, R.W. Powell, P.E. Liley, Thermal Conductivity of the Elements, J. Phys. Chem. Ref. Data 1 (2) (1972) 279.

[59] M.S. El-Genk, H. Bostanci, Saturation boiling of HFE-7100 from a copper surface, simulating a microelectronic chip, Int. J. Heat Mass Transf. 46 (2003) 1841–1854.

[60] S.J. Kline, F.A. McClintock, Describing uncertainties in single-sample experiments, Mech. Eng. 75 (1) (1953) 3–8.

[61] G. Moreno, S. Narumanchi, C. King, Pool boiling heat transfer characteristics of HFO-1234yf on plain and microporous-enhanced surfaces, J. Heat Transfer 135 (11) (2013) 111014.

[62] T.M. Anderson, I. Mudawar, Microelectronic cooling by enhanced pool boiling of a dielectric fluorocarbon liquid, J. Heat Transfer 111 (3) (1989) 752.

[63] J.H. Lienhard, V.K. Dhir, D.M. Riherd, Peak pool boiling heat-flux measurements on finite horizontal flat plates, J. Heat Transfer 95 (4) (1973) 477.

[64] J.H. Lienhard, V.K. Dhir, Hydrodynamic prediction of peak pool-boiling heat fluxes from finite bodies, J. Heat Transfer 95 (2) (1973) 152.

[65] R. Raj, J. Kim, Heater size and gravity based pool boiling regime map: transition criteria between buoyancy and surface tension dominated boiling, J. Heat Transfer 132 (9) (2010) 091503.

[66] C.H. Wang, V.K. Dhir, Effect of surface wettability on active nucleation site density during pool boiling of water on a vertical surface, J. Heat Transfer 115 (3) (1993) 659.

[67] S.M. You, T.W. Simon, A. Bar-Cohen, W. Tong, Experimental investigation of nucleate boiling incipience with a highly-wetting dielectric fluid (R-113), Int. J. Heat Mass Transf. 33 (1990) 105–117.

[68] Y.Y. Hsu, On the size range of active nucleation cavities on a heating surface, J. Heat Transfer 84 (3) (1962) 207–213.

[69] A. Bar-Cohen, M. Arik, M. Ohadi, Direct liquid cooling of high flux micro and nano electronic components, Proc. IEEE 94 (8) (2006) 1549–1570.

[70] S.M. Kwark, M. Amaya, R. Kumar, G. Moreno, S.M. You, Effects of pressure, orientation, and heater size on pool boiling of water with nanocoated heaters, Int. J. Heat Mass Transf. 53 (23-24) (2010) 5199–5208.

[71] M. Elgenk, J. Parker, Enhanced boiling of HFE-7100 dielectric liquid on porous graphite, Energy Convers. Manag. 46 (15-16) (2005) 2455–2481.

[72] J.W. Liu, D.J. Lee, A. Su, Boiling of methanol and HFE-7100 on heated surface covered with a layer of mesh, 2001.

[73] D. Gorenflo, E. Danger, A. Luke, S. Kotthoff, U. Chandra, C. Ranganayakulu, Bubble formation with pool boiling on tubes with or without basic surface modifications for enhancement, Int. J. Heat Fluid Flow 25 (2) (2004) 288–297.

[74] T. Hibiki, M. Ishii, Active nucleation site density in boiling systems, Int. J. Heat Mass Transf. 46 (14) (2003) 2587–2601.

[75] G. Kocamustafaogullari, M. Ishii, Interfacial area and nucleation site density in boiling systems, Int. J. Heat Mass Transf. 26 (9) (1983) 1377–1387.

[76] R.J. Benjamin, A.R. Balakrishnan, Nucleation site density in pool boiling of saturated pure liquids: Effect of surface microroughness and surface and liquid physical properties, Exp. Therm. Fluid Sci. 15 (1) (1997) 32–42.

[77] W. Tong, A. Bar-Cohen, T.W. Simon, S.M. You, Contact angle effects on boiling incipience of highly-wetting liquids, Int. J. Heat Mass Transf. 33 (1) (1990) 91–103.

[78] R. Cole, Bubble frequencies and departure volumes at subatmospheric pressures, AIChE J. 13 (4) (1967) 779–783.

[79] S.S. Kutateladze, I.I. Gogonin, Growth rate and detachment diameter of a vapor bubble in free convection boiling of a saturated liquid, High Temp. 17 (1980) 667–671.

[80] M.K. Jensen, G.J. Memmel, Evaluation of bubble departure diameter correlations, in: Proc. 8th Int. Heat Transf. Conf., Begell House Inc., 1986: pp. 1907–1912.

[81] H.T. Phan, N. Caney, P. Marty, S. Colasson, J. Gavillet, How does surface wettability influence nucleate boiling?, Comptes Rendus Mécanique 337 (5) (2009) 251–259.

[82] F.N. Peebles, H.J. Garber, Studies on the motion of gas bubbles in liquids, Chem. Eng. Prog. 49 (1953) 88–97.

[83] J.P. McHale, S. V. Garimella, Bubble nucleation characteristics in pool boiling of a wetting liquid on smooth and rough surfaces, Int. J. Multiph. Flow 36 (4) (2010) 249–260.

[84] R.W. Bowring, Physical model, based on bubble detachment, and calculation of steam voidage in the subcooled region of a heated channel, in: HPR-10, Inst. Atomenergi, Halden, Norw., 1962.

[85] W.H. McAdams, Heat transmission, 3rd ed., McGraw-Hill, New York, 1954.

[86] C.-Y. Han, P. Griffith, The mechanism of heat transfer in nucleate pool boiling—Part I, Int. J. Heat Mass Transf. 8 (6) (1965) 887–904.

[87] F. Demiray, J. Kim, Microscale heat transfer measurements during pool boiling of FC-72: effect of subcooling, Int. J. Heat Mass Transf. 47 (14-16) (2004) 3257–3268.

[88] B. Abbasi, J. Kim, A. Marshall, Dynamic pressure based prediction of spray cooling heat transfer coefficients, Int. J. Multiph. Flow 36 (6) (2010) 491–502.

[89] R.-H. Chen, L.C. Chow, J.E. Navedo, Effects of spray characteristics on critical heat flux in subcooled water spray cooling, Int. J. Heat Mass Transf. 45 (2002) 4033–4043.

[90] M.S. Sehmbey, L.C. Chow, M.R. Pais, T. Mahefkey, High heat flux spray cooling: a review, in: Heat Transf. High Heat Flux Syst. HTD-Vol. 301, ASME, Chicago, 1994: pp. 39–46.

[91] I. Mudawar, Assessment of high-heat-flux thermal management schemes, IEEE Trans. Components Packag. Technol. 24 (2) (2001) 122–141.

[92] C. Bonacina, S. Del Giudice, G. Comini, Dropwise Evaporation, J. Heat Transfer 101 (3) (1979) 441.

[93] J. Kim, Spray cooling heat transfer: The state of the art, Int. J. Heat Fluid Flow 28 (4) (2007) 753–767.

[94] T.A. Shedd, Next generation spray cooling: High heat flux management in compact spaces, Heat Transf. Eng. 28 (2) (2007) 87–92.

[95] E.A. Silk, E.L. Golliher, R.P. Selvam, Spray cooling heat transfer: Technology overview and assessment of future challenges for micro-gravity application, Energy Convers. Manag. 49 (2008) 453–468.

[96] J.D. Bernardin, I. Mudawar, Film boiling heat transfer of droplet streams and sprays, Int. J. Heat Mass Transf. 40 (1997) 2579–2593.

[97] K.A. Estes, I. Mudawar, Comparison of two-phase electronic cooling using free jets and sprays, J. Electron. Packag. 117 (4) (1995) 323–332.

[98] I. Mudawar, W. Valentine, Determination of the local quench curve for spray-cooled metallic surfaces, J. Heat Treat. 7 (2) (1989) 107–121.

[99] M. Ghodbane, J. Holman, Experimental study of spray cooling with Freon-113, Int. J. Heat Mass Transf. 34 (4) (1991) 1163–1174.

[100] J.S. Coursey, Enhancement of spray cooling heat transfer using extended surfaces and nanofluids, PhD dissertation, University of Maryland, College Park, 2007.

[101] J. Yang, L.C. Chow, M.R. Pais, Nucleate boiling heat transfer in spray cooling, J. Heat Transfer 118 (1996) 668–671.

[102] D.E. Tilton, C.L. Tilton, M.R. Pais, M.J. Morgan, High-flux spray cooling in a simulated multichip module, ASME Heat Transf. Div Publ. 206 (1992) 73–79.

[103] L. Lin, R. Ponnappan, Heat transfer characteristics of spray cooling in a closed loop, Int. J. Heat Mass Transf. 46 (2003) 3737–3746.

[104] A.G. Pautsch, T.A. Shedd, Spray impingement cooling with single- and multiple-nozzle arrays. Part I: Heat transfer data using FC-72, Int. J. Heat Mass Transf. 48 (15) (2005) 3167–3175.

[105] J.R. Rybicki, I. Mudawar, Single-phase and two-phase cooling characteristics of upward-facing and downward-facing sprays, Int. J. Heat Mass Transf. 49 (1-2) (2006) 5–16.

[106] S.J. Thiagarajan, S. Narumanchi, C. King, W. Wang, R. Yang, Enhancement of heat transfer with pool and spray impingement boiling on microporous and nanowire surface coatings, in: Proc. 14th Int. Heat Transf. Conf., Washington, D.C., 2010: pp. 1–10.

[107] M. Visaria, I. Mudawar, Effects of high subcooling on two-phase spray cooling and critical heat flux, Int. J. Heat Mass Transf. 51 (21-22) (2008) 5269–5278.

[108] B. Horacek, K. Kiger, J. Kim, Single nozzle spray cooling heat transfer mechanisms, Int. J. Heat Mass Transf. 48 (2005) 1425–1438.

[109] A. Pautsch, T. Shedd, Adiabatic and diabatic measurements of the liquid film thickness during spray cooling with FC-72, Int. J. Heat Mass Transf. 49 (2006) 2610–2618.

[110] D.P. Rini, R.-H. Chen, L.C. Chow, Bubble behavior and nucleate boiling heat transfer in saturated FC-72 spray cooling, J. Heat Transfer 124 (1) (2002) 63.

[111] B. Horacek, J. Kim, K.T. Kiger, Spray Cooling Using Multiple Nozzles: Visualization and Wall Heat Transfer Measurements, IEEE Trans. Device Mater. Reliab. 4 (4) (2004) 614–625.

[112] K.A. Estes, I. Mudawar, Correlation of Sauter mean diameter and critical heat flux for spray cooling of small surfaces, Int. J. Heat Mass Transf. 38 (16) (1995) 2985–2996.

[113] C. Sodtke, P. Stephan, Spray cooling on micro structured surfaces, Int. J. Heat Mass Transf. 50 (19-20) (2007) 4089–4097.

[114] H. Honda, J. Wei, Enhanced boiling heat transfer from electronic components by use of surface microstructures, Exp. Therm. Fluid Sci. 28 (2004) 159–169.

[115] J. Tehver, H. Sui, V. Temkina, Heat transfer and hysteresis phenomena in boiling on porous plasma-sprayed surface, Exp. Therm. Fluid Sci. 5 (6) (1992) 714–727.

[116] M.S. El-Genk, Nucleate boiling enhancements on porous graphite and microporous and macro-finned copper surfaces, Heat Transf. Eng. 33 (3) (2012) 175–204.

[117] S.G. Liter, M. Kaviany, Pool boiling CHF enhancement by modulated porous-layer coating: theory and experiment, Int. J. Heat Mass Transf. 44 (22) (2001) 4287–4311.

[118] I. Mudawar, K.A. Estes, Optimizing and predicting CHF in spray cooling of a square surface, J. Heat Transfer 118 (1996) 672–679.

[119] M. Monde, Y. Katto, Burnout in a high heat-flux boiling system with an impinging jet, Int. J. Heat Mass Transf. 21 (1978) 295–305.

[120] E.A. Silk, Investigation into enhanced surface spray cooling, PhD Dissertation, University of Maryland, College Park, MD, 2006.

[121] R.L. Puterbaugh, K.L. Yerkes, T.E. Michalak, S.K. Thomas, Cooling performance of a partially-confined FC-72 spray: the effect of dissolved air, in: 45th Annu. AIAA Aerosp. Sci. Meet. Exhib., Reno, NV, 2007: pp. 1–12.

[122] S.J. Thiagarajan, S. Narumanchi, R. Yang, Effect of flow rate and subcooling on spray heat transfer on microporous copper surfaces, Int. J. Heat Mass Transf. 69 (2014) 493–505.